

國立臺灣大學電機資訊學院電子工程學研究所

碩士論文

Graduate Institute of Electronics Engineering

College of Electrical Engineering & Computer Science

National Taiwan University

Master Thesis

矩形黑磷薄膜電晶體其光電特性的各向異性

The anisotropy of optoelectrical properties of
Rectangular Black Phosphorus Thin Film Transistor

王奇樺

Chi-Hua Wang

指導教授：李嗣涔 博士

Advisor : Si-Chen Lee, Ph.D.

中華民國 108 年 7 月

July, 2019

中文口試委員審定書



國立臺灣大學碩士學位論文 口試委員會審定書

矩形黑磷薄膜電晶體其光電特性各向異性

The anisotropy of optoelectrical properties of Rectangular
Black Phosphorus Thin Film Transistor

本論文係王奇樺君 (R06943112) 在國立臺灣大學電子工程學研究所完成之碩士學位論文，於民國 108 年 07 月 05 日承下列考試委員審查通過及口試及格，特此證明

口試委員：

木嗣澐
林浩鈺 (指導教授)
吳肇欣

系主任、所長

吳子宇

誌謝



這兩年的碩士時光在台大真的是學到了不少東西，無論是專業知識還是一些做人處事的道理。對於能夠完成這篇論文並順利畢業，首先我要感謝我的指導教授 李嗣涇博士，謝謝教授對於我在專業知識上的傳授以及教導我做研究的方法，使得我可以通過口試並完成論文。再來我要感謝馬姊協助我們處理一些機台維修或者是耗材購買的事務，使得我可以專心在研究上。謝謝張博彥、洪彬超以及蕭堯學長帶我認識二維材料，並教導我實驗以及操作機台的方法。謝謝余凱文以及彭天欣常常和我討論實驗，我們都是做二維材料的，在研究上常常有許多可以互相借鏡的地方，兩年下來承蒙你們照顧了。謝謝湯董、洪教授、曾奕融以及郭哲邵常常陪我聊天吃飯，讓我在實驗室的時光總是充滿了歡笑。希望 Lee group 的大家畢業之後可以工作順利，鵬程萬里。

再來我要感謝王俊雄、蔣耘洁以及李家碩學長幫我進行量測，使得我可以順利完成碩論三四章 AFM 以及照光量測的部分。謝謝陳昂寬、王子珩以及林庭萱常常幫我約真空量測。謝謝四宮輝夜以及中野四葉這兩位可愛的女孩，妳們兩位絕對是我在碩二下可以順利完成論文的精神支柱。輝夜，恭喜妳最近和會長的關係有了重大突破，除了預祝你們未來感情順利以外，再來我和會長都要去美國了，答應我，一起來美國吧！四葉，我就知道妳是風太郎命中註定之人，我相信最後成為新娘的絕對是妳，如果妳最後沒有跟風太

郎回家也沒關係，我帶妳回家。謝謝狗哲、溫大、子睿還有昱翔周末常常陪
我玩，去美國以後我一定會想念和你們一起混的時光。最後的最後，我要謝
謝我的父母家人，沒有你們的支持與陪伴，我是無法順利完成這篇論文。最
後預祝大家平安、快樂、發大財，謝謝大家。



摘要

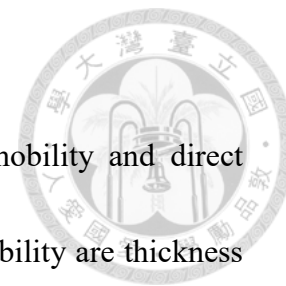


黑磷為一種具有高電洞遷移率以及直接能隙(= 0.33eV) 的二維材料。影響其載子遷移率的因素包括了黑磷薄膜的厚度、contact 金屬的選擇以及載子移動的方向。因此必須同時考慮這三個因素，才有辦法達到黑磷薄膜電晶體的高電洞遷移率。

本論文首先對黑磷的基本性質做了材料分析。透過光學顯微鏡以及原子力顯微鏡的搭配可以粗略的判斷黑磷薄片的厚度，拉曼光譜儀則能夠用來辨認黑磷薄片的晶體方向。X 射線與極紫外線光電子能譜儀則可用來確認黑磷與金鍍合金元素組成、能隙與功函數。透過挑選適當的厚度、使用金鍍合金來達成歐姆接觸、以及製作長方形黑磷來迅速判斷黑磷晶格方向，成功製造出擁有良好元件特性的背電極黑磷薄膜電晶體，其元件表現出接近 $300\text{cm}^2/\text{V}\cdot\text{s}$ 的場效電洞遷移率和高達 3 個數量級的電流開關比。同時也製作了黑磷-二硫化鎢的異質界面整流二極體與透過厚度控制達成的黑磷同質界面整流二極體，兩者接近 2 的理想因子顯示其電流主要為復合電流主控。兩者良好的光響應則展現了具有直接能隙的黑磷在光電應用上的潛力。

關鍵字: 黑磷、薄膜電晶體、厚度、金鍍合金、長方形、黑磷-二硫化鎢異質界面

ABSTRACT



Black Phosphorus (BP) is a 2D material with high hole mobility and direct bandgap ($= 0.33\text{eV}$). The factors that will influence its carrier mobility are thickness of the BP thin film, choice of the contact metal and the transport direction of the carriers. Therefore, these three factors must be considered simultaneously to obtain the high hole mobility of BP thin film transistors.

In this thesis, material analysis is first conducted to study the fundamental properties of the exfoliated BP. The thickness of BP flakes can be roughly determined by optical microscopy and atomic force microscopy (AFM). The lattice orientation of BP flakes can be recognized by Raman spectroscopy. X-ray and Ultraviolet photoelectron spectroscopy are used to measure the elemental composition, bandgap and work function of BP and AuGe alloy. Through picking the appropriate thickness of the BP thin film, using AuGe alloy to obtain ohmic contact, and fabricating rectangular BP thin film to determine the lattice orientation of BP flakes, the back-gated BP thin film transistors (TFTs) are successfully fabricated and show excellent device performance. The high hole mobility near $300\text{cm}^2/\text{V}\cdot\text{s}$ and the on/off ratio up to 3 order of magnitude can be achieved. The P-N BP/ WS_2 heterostructure and BP homostructure through thickness engineering are also fabricated. Both of their ideality factors are near 2, indicating that the forward current is dominated by

recombination current. Their good optical responsivities also show BP's potential in the application of optoelectronics due to its direct bandgap.



Key words: black phosphorus (BP), thin film transistor (TFT), thickness, AuGe alloy, rectangular, BP/WS₂ heterostructure

CONTENTS

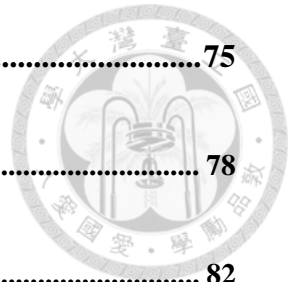


摘要.....	i
ABSTRACT	v
CONTENTS.....	vii
LIST OF FIGURES.....	x
LIST OF TABLES.....	xviii
Chapter 1 Introduction	1
1.1 Overview of black phosphorus	1
1.2 Advantages of BP FETs	9
1.3 Motivation	14
Chapter 2 Experiments	17
2.1 Fabrication Systems	17
2.1.1 Mechanical Exfoliation.....	17
2.1.2 Photolithography.....	22
2.1.3 E-beam lithography	24
2.1.4 Evaporation System.....	28
2.1.5 Rapid Thermal Annealing (RTA)	28
2.1.6 Heterostructure Fabrication System.....	29
2.2 Measurement Techniques	31
2.2.1 Optical Microscopy (OM)	31

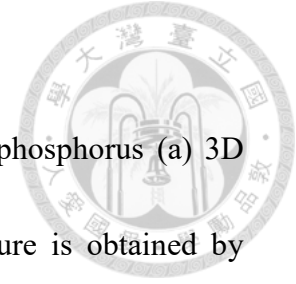
2.2.2 Atomic Force Microscopy (AFM).....	32
2.2.3 Raman Spectroscopy	33
2.2.4 X-ray Diffraction (XRD)	34
2.2.5 X-ray Photoelectron Spectroscopy (XPS).....	35
2.2.6 Ultraviolet Photoemission Spectroscopy (UPS).....	36
2.2.7 Current – Voltage Characteristics	39
Chapter 3 Material Analysis for Black Phosphorus.....	40
3.1 Crystal Structure of Black Phosphorus.....	40
3.2 Characterization of Black Phosphorus Film Thickness.....	43
3.2.1 Optical Microscopy (OM)	43
3.2.2 Atomic Force Microscope (AFM).....	44
3.3 Raman Spectroscopy	50
3.4 XPS and UPS Analysis of Black Phosphorus and Gold-Germanium alloy.....	57
3.4.1 X-ray Photoelectron Spectroscopy (XPS).....	57
3.4.2 Ultraviolet Photoelectron Spectroscopy (UPS)	64
Chapter 4 BP Thin Film Transistors.....	70
4.1 Back-gated Black Phosphorus TFTs	71
4.1.1 Device Process Flow	71



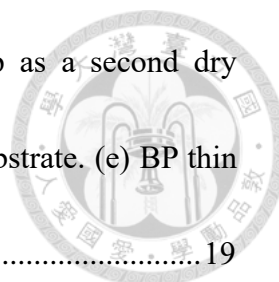
4.1.2 Device Performance	75
4.2 Thickness Dependence of Electronic Properties.....	78
4.3 Contact Metal Comparison of BP TFTs.....	82
4.4 Anisotropic Properties of Black Phosphorus	91
4.5 Characteristics of P-N BP/WS ₂ Heterostructure.....	100
4.5.1 Device Process Flow for BP-WS ₂ Heterostructure.....	100
4.5.2 Device Performance	102
4.5.3 BP Homostructure P-N-Like Diode through Thickness Control	109
Chapter 5 Conclusion.....	112
References	115



LIST OF FIGURES



- Fig. 1.1 Schematic diagram of the crystalline structure of black phosphorus (a) 3D representation, (b) lateral view, (c) top view. Crystal structure is obtained by density functional theory(DFT).4
- Fig. 1.2 (a) Crystal structure of bulk BP marked with coordinate axes(x,y,z) and lattice vectors(a,b,c) (b) The first Brillouin zone and some high symmetric points of bulk black phosphorus.5
- Fig. 1.3 (a) Calculated band structures for monolayer, bilayer, trilayer and bulk black phosphorus sheets at all high-symmetry points in the Brillouin zone. The energy is scaled with respect to the Fermi energy E_F . (b) Thickness dependence of the black phosphorus band gap, calculated with different approaches.....7
- Fig. 1.4 Moore’s Law: Gordon Moore, the co-founder of Intel, predicted that transistor density and thus chip performance would double every 18 months. ... 10
- Fig. 1.5 (a) Cross-section of an n-channel Si MOSFET, (b)The potential $\psi(x)$ distribution from the source to drain. (c) The potential energy distribution $U(x)$ for electrons from the source to drain. 12
- Fig. 1.6 Trends of “More Moore” and “More than Moore” reported by 2013 ITRS... 13
- Fig. 2.1 Illustration of mechanical exfoliation process: (a) Bulk BP is adhered to the Blue Nitto tape, leave some BP flakes on the tape. (b) Fold the tape numerous



times to make the BP flakes thinner. (c) Use PDMS stamp as a second dry transfer. (d) Press down the PDMS stamp onto the Si/SiO₂ substrate. (e) BP thin films were successfully exfoliated onto the substrate..... 19

Fig. 2.2 Needle-shaped BP flakes on blue Nitto tape under (a) naked eye and (b) optical microscopy observation, respectively.21

Fig. 2.3 The PDMS stamp used in this research.21

Fig. 2.4 Exfoliated rectangular BP on 300nm SiO₂/Si substrate under optical microscopy. Scale bar is 20um.....22

Fig. 2.5 (a) The spin-coater and hot plate used in this research (b) The exposure system used in this research.....23

Fig. 2.6 Illustration of undercut PMMA formation: (a) After spin-coated bi-layer PMMA and soft bake, the photoresist is dosed by electron beam. (b) The darker colors represent the molecular chain scissored by electron beam. (c) The undercut structure is formed after development.26

Fig. 2.7 The equipment of EBL process, JEOL JSM7001F.....27

Fig. 2.8 The equipment of RTA system, MILA-300028

Fig. 2.9 Three axis micrometer stage.....30

Fig. 2.10 Heterosutstructure fabrication system.....30

Fig. 2.11 The optical microscopy used in this research.31

Fig. 2.12 (a) and (b) indicates that the thickness of this BP nanosheet is roughly 15nm.

..... 33

Fig. 2.13 The equipment of Raman measurement used in this research..... 34

Fig. 2.14 Energy level diagram of the emitted photoelectron..... 36

Fig. 2.15 (a) and (b) Schematic diagram showing how photoelectrons are generated. 38

Fig. 3.1 (a) The X-ray diffraction pattern of bulk BP crystal. Schematic of the unit cell
of BP. (b) Top View. (c) Lateral view..... 42

Fig. 3.2 (a) The OM image of an exfoliated BP nanosheet with green color. (b) The
AFM image of this BP nanosheet. The white line marks the position of the line
profiles shown in (c). (c) AFM line profile for the thickness of BP. The thickness
of this BP nanosheet is about 14 nm. 46

Fig. 3.3 (a) The OM image of an exfoliated BP nanosheet with yellow color. (b) The
AFM image of this BP nanosheet. The white line marks the position of the line
profiles shown in (c). (c) AFM line profile for the thickness of BP. The thickness
of this BP nanosheet is about 43 nm. 47

Fig. 3.4 (a) The OM image of an exfoliated BP nanosheet with both green and yellow
color. (b) and (d) The AFM image of this BP nanosheet. The white line, which is
at the green and yellow part of this BP nanosheet, respectively, marks the
position of the line profiles shown in (c) and (e), respectively. (c) and (e) AFM

line profile for the thickness of BP. The thickness of the green and yellow part of this BP nanosheet is about 12.4 nm and 29 nm, respectively.49

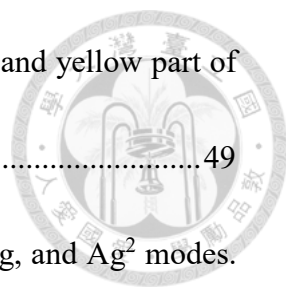


Fig. 3.5 Schematic plot showing the vibration directions of Ag^1 , B^2g , and Ag^2 modes.

The atoms oscillate along the z (out-of-plane), x (zigzag) and y (armchair) directions, respectively.....51

Fig. 3.6 (a) Optical image of a BP flake. θ is the angle between the zigzag

crystallographic direction and polarization direction of incident laser. The scale bar is $10 \mu m$. (b) Polarization dependence of Ag^1 , B^2g , and Ag^2 modes. The solid

curves are the theoretical value and the dots are the experimental results. (c)

Angle dependent Raman spectra for BP. The three characteristic Raman modes, Ag^1 ($362 cm^{-1}$), B^2g ($439 cm^{-1}$) and Ag^2 ($467 cm^{-1}$), can be observed.54

Fig. 3.7 The polar plots of Raman intensity for each Raman vibration mode with 532

nm excitation.....55

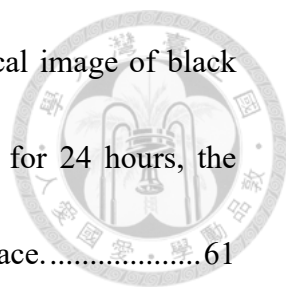
Fig. 3.8 The Raman intensity ratios of Ag^2 to Ag^1 vibration modes for 20 rectangular

BP samples (labeled as A~T). The polarizations of the 532 nm laser excitation are along AC and ZZ directions. The average intensity ratios of the AC and ZZ

directions are 2.40 and 1.08, respectively.56

Fig. 3.9 Energy level diagram of the emitted photoelectron.....58

Fig. 3.10 (a) X-ray photoelectron spectrum for BP P2p core level. (b) O 1s core level



spectrum. (c) Schematic diagram of P_2O_5 molecule. (d) Optical image of black phosphorus nanosheet after exposing to ambient atmosphere for 24 hours, the “bubbles” implied the water absorption on the hydrophilic surface..... 61

Fig. 3.11 (a) X-ray photoelectron spectrum for Ge3d core level. (b) Au4f core level spectrum..... 62

Fig. 3.12 XPS results of BP with 1.5 nm Ge on top of it before and after RTA. After RTA, the peak of P-Ge bond shows up. 63

Fig. 3.13 Band diagram of an unknown material..... 65

Fig. 3.14 (a), (b) and (c) UPS spectra of bulk BP. (d) Band diagram of bulk black phosphorus. 68

Fig. 3.15 (a) and (b) UPS spectra of AuGe alloy. 70

Fig. 4.1 Top view of BP TFT (a) before and (b) after device fabrication under optical microscope. The width and length of the device is 1.8um/2.9um, respectively. (c) Cross-sectional view of back-gated BP TFT structure. 73

Fig. 4.2 The flow chart of back-gated BP TFT fabrication processes. 74

Fig. 4.3 Output characteristics of Cr contact BP TFT (a) before and (b) after thermal annealing. 76

Fig. 4.4 Transfer characteristics of Cr contact BP TFT (a) before and (b) after thermal annealing. 77

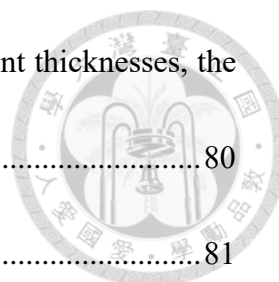


Fig. 4.5 Transfer characteristics of BP TFT in log scale with different thicknesses, the green arrow indicates the sweep direction of the gate bias..... 80

Fig. 4.6 The model of back-gated BP TFT 81

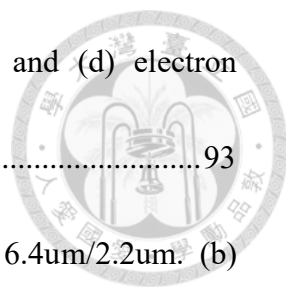
Fig. 4.7 (a) Optical image of the Cr contact TLM sample (b) Transfer characteristics of the Cr contact device, $L = 1.8 \text{ um}$. (c) Output characteristics of the Cr contact device for hole current transport and (d) electron current transport. (e) Result of TLM extraction method. 86

Fig. 4.8 (a) Optical image of the Ni contact TLM sample (b) Transfer characteristics of the Ni contact device, $L = 1 \text{ um}$. (c) Output characteristics of the Ni contact device for hole current transport and (d) electron current transport. (e) Result of TLM extraction method. 87

Fig. 4.9 (a) Optical image of the AuGe alloy contact TLM sample (b) Transfer characteristics of the AuGe alloy contact device, $L = 3.5 \text{ um}$. (c) Output characteristics of the AuGe alloy contact device for hole current transport and (d) electron current transport. (e) Result of TLM extraction method..... 88

Fig. 4.10 Three different metal's contact resistance versus back gate bias. Note that the dependency of the contact resistance versus back gate bias for AuGe alloy contact is quite different than the other two metals. 89

Fig. 4.11 (a) AFM image of the ZZ direction sample, $W/L = 2.55\text{um}/2.8\text{um}$. (b)



Thickness = 11.5 nm. Output characteristics for (c) hole and (d) electron transport. (e) Transfer characteristics..... 93

Fig. 4.12 (a) AFM image of the AC direction sample, W/L = 6.4um/2.2um. (b) Thickness = 20 nm. Output characteristics for (c) hole and (d) electron transport (e) Transfer characteristics..... 94

Fig. 4.13 (a) AFM image of the BP TFT sample, W/L = 4.35um/3.5um for ZZ, and 1um/1.7um for AC, respectively. (b) Thickness = 35 nm. Transfer characteristics for (c) ZZ direction and (d) AC direction. 96

Fig. 4.14 Illustration of the current spreading effect in BP TFT. 97

Fig. 4.15 The mobilities along AC (black line) and ZZ (blue line) directions and the μ_{AC}/μ_{ZZ} ratio versus back gate bias (red line), the ZZ and AC samples are mentioned in Fig 4.11 and Fig. 4.12, respectively. 98

Fig. 4.16 The mobilities along AC (black line) and ZZ (blue line) directions and the μ_{AC}/μ_{ZZ} ratio versus back gate bias (red line), the AC and ZZ samples are mentioned in Fig. 4.13. 99

Fig. 4.17 The flow chart for BP-WS₂ heterostructure fabrication process 101

Fig. 4.18 (a) BP flakes on 300nm SiO₂ substrate (b) Dry transfer WS₂ onto BP (c) Completed device under optical microscope (d) Schematic diagram of the completed device. 102

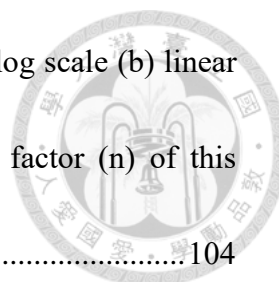


Fig. 4.19 I_d versus V_d of BP-WS₂ heterostructure P-N diode in (a) log scale (b) linear scale. Note that the red dashed line can extract the ideality factor (n) of this device.104

Fig. 4.20 The ideality factor and on/off ratio of BP-WS₂ heterostructure P-N diode under different back gate bias. 104

Fig. 4.21 The emission spectra of Xe lamp. 105

Fig. 4.22 (a) I_d versus V_d characteristics of BP-WS₂ heterostructure under various incident light intensity (b) Enlarged graph of (a) at $V_d < 0$ 106

Fig. 4.23 Responsivity of BP-WS₂ Heterostructure versus incident light intensity... 107

Fig. 4.24 Ideal Band diagram of BP-WS₂ Heterostructure before contact. 108

Fig. 4.25 BP homostructure P-N-like diode under (a) Optical microscope (b) 3D AFM image (c) 2D AFM image, the white line indicates the position of the line profiles shown in (d). (d) The result of the AFM measurement. 111

Fig. 4.26 I_d - V_d plot of the homojunction P-N-like diode in (a) log scale (b) linear scale. Notice that at $V_d = 0V$, the diode also didn't show any photoresponse, indicating that the homojunction P-N-like diode is not a photodiode but a photoconductor..... 112

LIST OF TABLES

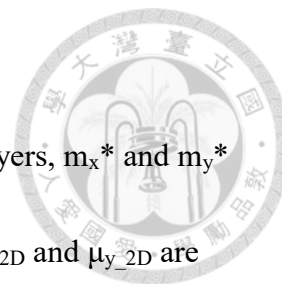


Table 1.1 Predicted carrier mobility. N_L represents the number of layers, m_x^* and m_y^* are carrier effective masses along AC and ZZ, respectively. μ_{x_2D} and μ_{y_2D} are mobilities along AC and ZZ, respectively.....	8
Table 2.1 photolithography conditions	23
Table 2.2 E-beam lithography conditions	27
Table 3.1 Thickness dependence of color for BP film on 300 nm SiO_2/Si substrate under optical microscopy.	44
Table 4.1 Electronic properties of BP TFTs before and after thermal annealing.....	77
Table 4.2 Electronic properties of BP TFTs for different thicknesses.	80
Table 4.3 Electronic properties of BP TFTs with different metal contacts.	89
Table 4.4 Three different metal's contact resistance versus back gate bias.....	90
Table 4.5 Electrical properties of BP TFTs along two transport directions.	95
Table 4.6 Electrical properties of BP TFTs along two transport directions on the same flake.....	96
Table 4.7 Device performance of the homojunction P-N-like diode	112

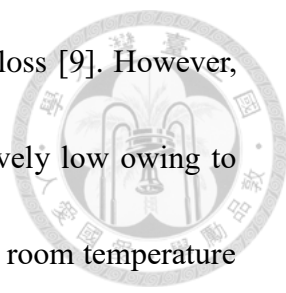
Chapter 1 Introduction

1.1 Overview of black phosphorus



The band theory of graphite was first analyzed by Wallace in 1947 as a beginning for understanding the electronic properties of 3D graphite [1], but the feasible method of fabricating two-dimensional graphene remained unknown. In 2004, Novoselov et al. discovered a convenient way to fabricate 2D graphene with the thickness is decreased down to only single layer or few layers by using scotch tape to mechanically peel graphene thin flakes from bulk graphite crystal [2]. This exfoliation method has aroused tremendous interests in the study of graphene and other two dimensional materials such as hexagonal-boron nitride (h-BN), transition metal dichalcogenides (TMDCs) and black phosphorus (BP) [3, 4].

Although graphene has extremely high mobility due to its massless Dirac feature fermions, which made graphene a possible candidate for field effect transistor(FET) applications [5, 6], the fact that pristine graphene's lack of energy bandgap makes graphene-based FET too hard to be turned off [7], which implies that graphene is not suitable for FET applications. Therefore, many researchers have turned to other 2D materials such as molybdenum disulfide (MoS_2), which is one kind of transition metal dichalcogenides (TMDCs) and has a large bandgap of 1.8eV [8]. In 2011, Radisavljevic et al. fabricated the first single layered molybdenum disulfide (MoS_2)



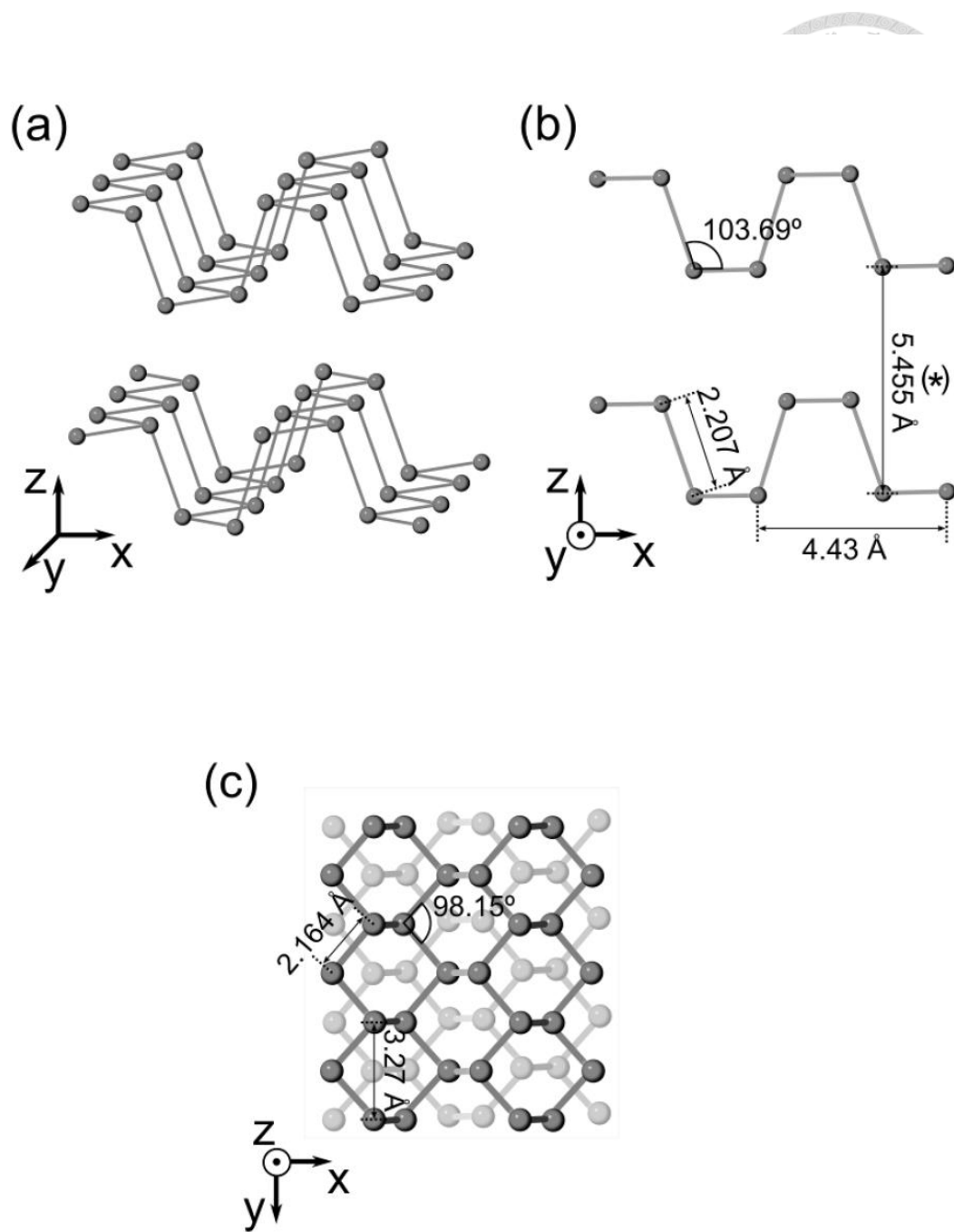
FET with a high drain current on/off ratio and low standby power loss [9]. However, the mobility of MoS₂ or other TMDCs-based transistors are relatively low owing to the heavy effective mass of carriers and severe phonon scattering at room temperature [10, 11]. Besides, it also faces a problem of not compatible to modern CMOS processes [12]. Recently, black phosphorus (BP), one of the 2D materials, has brought about much interests due to its better electrical properties such as proper bandgap and high mobility [13, 14].

Black phosphorus is the most thermodynamically stable allotrope of phosphorus at room temperature and pressure [15]. Bulk BP can be synthesized by heating white phosphorus or red phosphorus under high pressures (12,000 atmospheres) [16, 17]. The electronic properties and crystal structure of BP are very much like those of graphite with both being black and flaky, a conductor of electricity [18-20], and having puckered sheets of linked atoms. While black phosphorus is the most steady form among all allotropes of phosphorus, environmental vulnerability is still a crucial issue [21, 22].

Black phosphorus is a layered material in which individual atomic layers are stacked together by van der Waals force [23]. BP has an orthorhombic structure and is the least reactive allotrope of phosphorus, a result of its lattice of interlinked six-membered rings where each phosphorus atom is covalently bonded to three

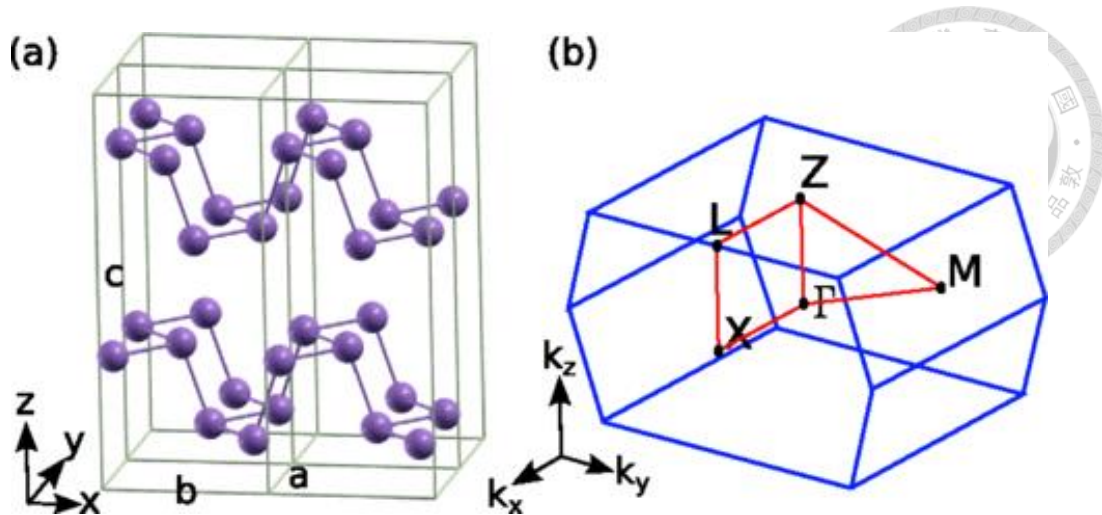
adjacent phosphorus atoms to form a puckered honeycomb structure [19, 24, 25], as shown in Fig 1.1. In this figure, the x and y directions in BP structure correspond to the armchair(AC) and zigzag(ZZ) direction, respectively. It should also be noted that phonons, photons, and electrons in layered black phosphorus structure display rather anisotropic features within the plane of layers [26-28].

Fig. 1.2 (a) shows the primitive cell of black phosphorus in its honeycomb lattice. Its primitive unit vector in reciprocal lattice can be obtained by using Fourier transform, as well as its Brillouin zone and high symmetry points, as shown in Fig. 1.2 (b).



2D Materials, 2014, 1(2) 025001

Fig. 1.1 Schematic diagram of the crystalline structure of black phosphorus (a) 3D representation, (b) lateral view, (c) top view. Crystal structure is obtained by density functional theory(DFT).



P.-L. Gong et al., arXiv:1507.03213.

Fig. 1.2 (a) Crystal structure of bulk BP marked with coordinate axes(x,y,z) and lattice vectors(a,b,c) (b) The first Brillouin zone and some high symmetric points of bulk black phosphorus.

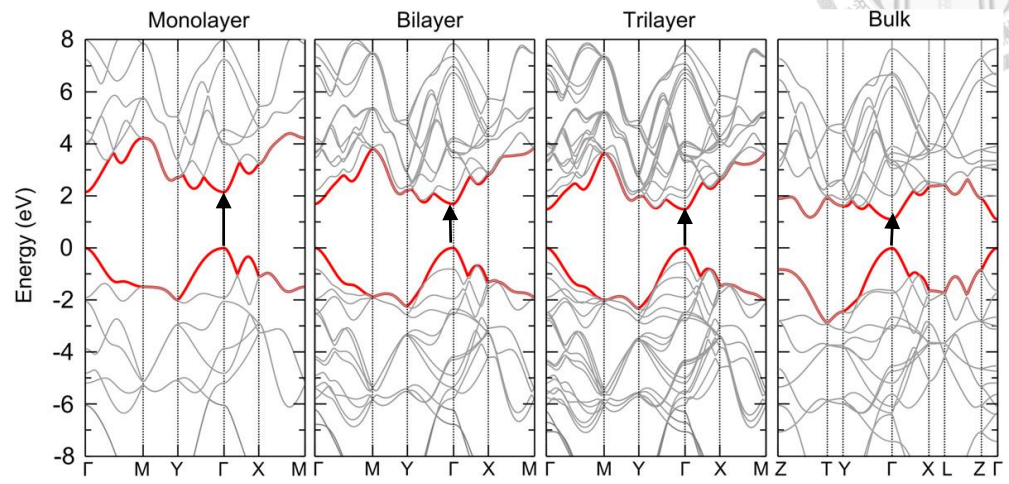
The band structure of black phosphorus is thickness dependent, which can be attributed to interlayer interactions. Fig. 1.3 (a) shows the calculated band structure of black phosphorus for monolayer, bilayer, trilayer and bulk by density functional theory(DFT) [24]. The bandgap of monolayer black phosphorus(phosphorene) is predicted to be about 2.0eV at the Γ point of the first Brillouin zone [14]. It should be noticed that as the layer number increases, the bandgap of BP remains direct at the Γ point of the first Brillouin zone for all thicknesses. Fig. 1.3 (b) shows the relationship between thickness and bandgap calculated with different ab initio methods [24, 29, 30]. Even though the magnitude of bandgap counts on which approximation method is used, all of the cases show that the bandgap greatly decreases as the layer number

increases [14]. This thickness dependent bandgap, which is due to the quantum confinement of the charge carriers in the out-of-plane direction [31], is stronger than that observed in those of the other 2D semiconductor materials. The band structure approximation of BP shows that BP has the needed bandgap for the field-effect transistor applications.

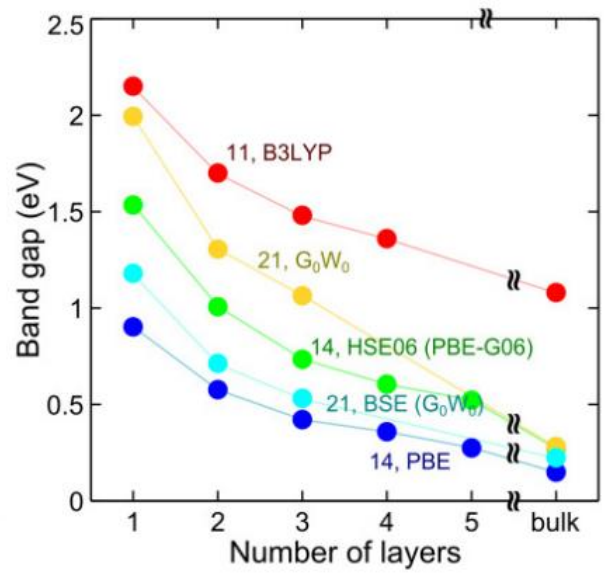
Moreover, although black phosphorus exhibits an intrinsic ambipolar behavior, the conduction type in few layered BP is hole-dominant for the following two reasons. First, the activation energy for p-type BP is lower than that of n-type BP [14]. Second one is the higher degree of anisotropy of the hole effective mass [32].



(a)



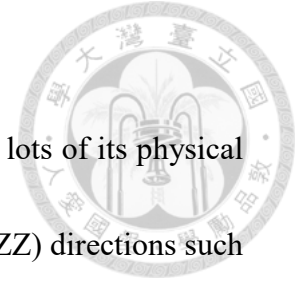
(b)



2D Materials, 2014, 1(2): p. 025001.

Fig. 1.3 (a) Calculated band structures for monolayer, bilayer, trilayer and bulk black phosphorus sheets at all high-symmetry points in the Brillouin zone. The energy is scaled with respect to the Fermi energy E_F . (b) Thickness dependence of the black phosphorus band gap,

calculated with different approaches.



According to the in-plane anisotropic geometry of BP crystal, lots of its physical characteristics are also quite different in armchair(AC) and zigzag(ZZ) directions such as electronic, thermal, optical and mechanical properties [33, 34]. Some physical properties along AC and ZZ directions for few-layered BP are theoretically predicted, listed in Table. 1.1. Except for mono layer, the ratio of mobility along AC and ZZ directions are predicted to be about 2 for holes and 4 for electrons at room temperature [30]. The experimental ratio of hole mobility, the dominant transport carriers of BP, is about 1.5~1.8 [28, 35]. Thus, in order to achieve better performance for BP devices, the AC direction should be used as the current channel because of the higher mobility on this direction.

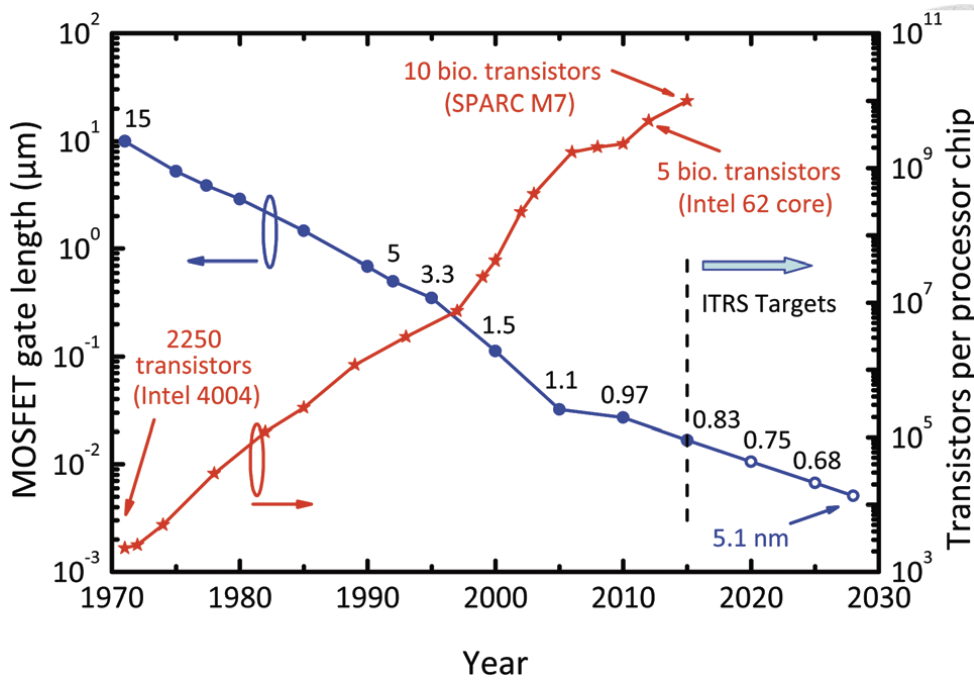
Table 1.1 Predicted carrier mobility. N_L represents the number of layers, m_x^* and m_y^* are carrier effective masses along AC and ZZ, respectively. μ_{x_2D} and μ_{y_2D} are mobilities along AC and ZZ, respectively.

Carrier type	N_L	m_x^*/m_0 $\Gamma-X$	m_y^*/m_0 $\Gamma-Y$	$\mu_{x, 2D}$ ($10^3 \text{ cm}^2 \text{ V}^{-1} \text{ s}^{-1}$)	$\mu_{y, 2D}$ ($10^3 \text{ cm}^2 \text{ V}^{-1} \text{ s}^{-1}$)
electron	1	0.17	1.12	1.10-1.14	~ 0.08
	2	0.18	1.13	~ 0.60	0.14-0.16
	3	0.16	1.15	0.76-0.80	0.20-0.22
	4	0.16	1.16	0.96-1.08	0.26-0.30
	5	0.15	1.18	1.36-1.58	0.36-0.40
hole	1	0.15	6.35	0.64-0.70	10-26
	2	0.15	1.81	2.6-2.8	1.3-2.2
	3	0.15	1.12	4.4-5.2	2.2-3.2
	4	0.14	0.97	4.4-5.2	2.6-3.2
	5	0.14	0.89	4.8-6.4	3.0-4.6

arXiv:1401.5045 (2014).

1.2 Advantages of BP FETs

The development trend of semiconductor devices have followed an empirical regularity called “Moore’s Law”, and the transistors have kept scaling down in the last fifty years as shown in Fig 1.4 [36]. However, with the channel length scaling, transistors will inevitably suffer several problems such as leakage current and short channel effect [37, 38]. Scaling theory has predicted that a field effect transistor (FET) with a thinner dielectric and a thinner gate-controlled region will alleviate the short channel effect down to very short gate length [39]. The reason for this phenomenon can be illustrated by using the concept of characteristic length as shown below [37].



Nanoscale, 2015, 7, 8261-8283

Fig. 1.4 Moore's Law: Gordon Moore, the co-founder of Intel, predicted that transistor density and thus chip performance would double every 18 months.

Structure of typical planar silicon-based metal-oxide-semiconductor field effect transistor (MOSFET) is demonstrated in Fig 1.5 (a). The potential $\phi(x)$ and potential energy $U(x)$ distribution along the channel are demonstrated in Fig 1.5 (b) and (c), respectively. The characteristic length λ is defined in Eq. (1.1) and the lowest potential along the channel ϕ_{\min} is defined in Eq. (1.2)

$$\lambda = \sqrt{\frac{\epsilon_s}{\epsilon_{ox}} t_s t_{ox}} \quad (1.1)$$

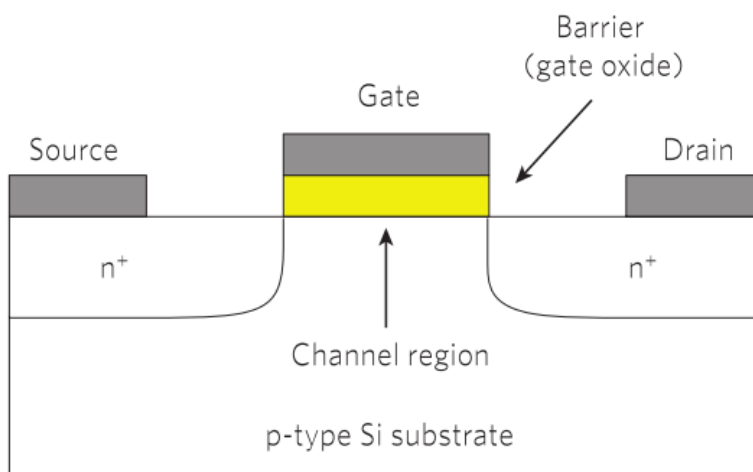
$$\phi_{\min} \approx 2\sqrt{\phi_s \phi_d} e^{-L_{\text{eff}}/2\lambda} \quad (1.2)$$

where λ : characteristic length, ϵ_s : the permittivity of semiconductor, ϵ_{ox} : the permittivity of gate oxide, t_s : thickness of semiconductor channel, t_{ox} : thickness of

gate oxide, ϕ_{\min} : the lowest potential along the channel, ϕ_s : the potential at the source, ϕ_d : the potential at the drain, L_{eff} : the effective channel length.

It is obvious that the higher ratio between L_{eff} and λ results in a larger potential barrier between the source and drain, thereby leading to a better gate control. Therefore, in order to lessen the short channel effect while the channel length keeps scaling down, the characteristic length λ should be reduced so that a large ratio between L_{eff} and λ can be maintained. According to Eq. (1.1), in order to have a smaller λ , a thinner dielectric and a thinner channel is required.

(a)



(b)

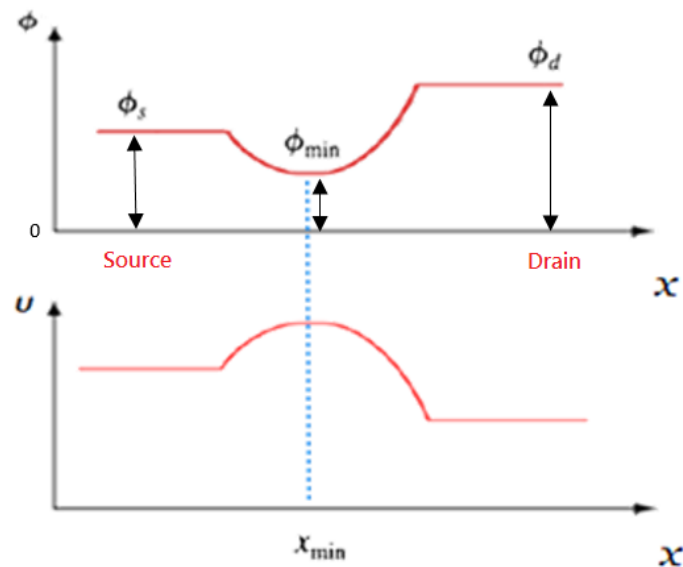


Fig. 1.5 (a) Cross-section of an n-channel Si MOSFET, (b) The potential $\psi(x)$ distribution from the source to drain. (c) The potential energy distribution $U(x)$ for electrons from the source to drain.

Therefore, 2D materials such as graphene or black phosphorus are promising materials to solve the short channel problem with its nano-scaled layer thickness [7, 9, 40]. Compared to 3D materials, even if the thickness of 3D materials' channel is scaling down, the surface roughness of 3D material will significantly degrade the carrier mobility. Even worse, the channel will show a serious thickness fluctuation that leads to undesirably huge threshold-voltage variations. These problems occur even at thickness many times greater than the thickness of 2D materials. What's more, because there are no out-of-plane broken bonds, 2D materials have no dangling bonds on the surface, producing a clean semiconductor-metal interface. In Fig. 1.6, 2D

materials are reported by the International Technology Roadmap for Semiconductors to be one of the key solutions to overcome the challenges faced in maintaining Moore's Law.



Fig. 1.6 Trends of “More Moore” and “More than Moore” reported by 2013 ITRS.

Li et al. fabricated the first BP FETs in 2014 [13]. Since then, lots of high performance BP FETs have been fabricated [27, 28, 41, 42]. Furthermore, tunable direct bandgap of BP ranging from 0.3eV in the bulk material to 1.5~2.0 eV in the monolayer, which covers large portions of the visible and near infrared electromagnetic spectrum, makes BP a promising candidate for future nano-scaled electronic and optoelectronic applications [42-45]. Differ from MoS₂ with only n-type characteristics, BP exhibits an ambipolar behavior [46], which is suitable for modern CMOS applications. Moreover, the unique in-plane anisotropy of BP [32] makes it

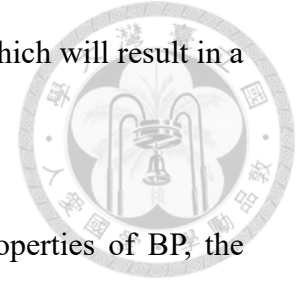
possible to be used in thermoelectric [47, 48], photonic and optoelectronic devices [49-51]. Hence, BP have the prospect to replace silicon and give a better performance for electronic devices.



1.3 Motivation

As mentioned before, the excellent electronic properties of black phosphorus make it appealing for applications in transistor, logic and optoelectronic devices. However, there are two important issues that will restrain the BP device performance. The first one is BP's unique anisotropic properties. Since BP is the first widely studied two-dimensional material to undergo degradation upon exposure to ambient atmosphere [22, 52], and there are concerns that BP might severely degrade during the process of determining the direction of BP, most of the previous researches about BP

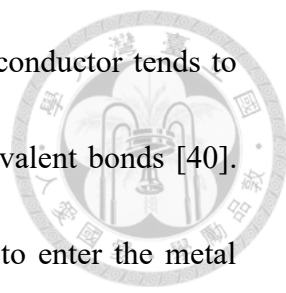
FETs did not take BP's anisotropic properties into consideration, which will result in a non-optimized performance of the BP FETs.



Although there are some efforts to study the anisotropic properties of BP, the mechanical exfoliation method will generate a bunch of irregular-shaped BP thin film and thus limit the accuracy of electrical measurement. On the other hand, the CVD technology of BP has not been mature enough to attain high performance BP FETs [53]. Consequently, it is quite challenging to accurately measure the electrical anisotropic properties of BP.

However, the good news is that based on the orthorhombic primitive cell of BP crystal, BP thin film with a unique rectangular shape has been successfully fabricated after improving the traditional exfoliation method [54]. The rectangular BP has two mutually perpendicular sides with the longer and shorter sides being ZZ and AC directions, respectively. There are two advantages of the rectangular-shaped BP thin film. First, the in-plane lattice orientation can be quickly determined through a simple optical microscopy observation alone, which is crucial during the fabrication process of BP FETs. Second, the rectangular shape of BP thin film will lead to a more precise measurement of the anisotropic properties of BP FETs.

The second factor that will limit the performance of the BP FETs is the large contact resistance at the interface of the source/drain metal and BP channel.



Compared to 3D(bulk) material, the pristine surface of a 2D semiconductor tends to form a van der Waals (vdW) gap with metal contact instead of covalent bonds [40]. This vdW gap acts as an additional tunneling barrier for carriers to enter the metal contact, thereby resulting in a higher contact resistance. In some cases, this vdW gap can be eliminated by forming a “metallic” contact between the interface of metal and 2D material, which was reported in graphene and MoS₂ [55, 56].

So far, the most common strategy for lowering the contact resistance of BP devices is choosing high work function metals. For example, using palladium (work function=5.12eV) as metal contact can allow more holes to inject into the contact, hence reducing the contact resistance for p-type BP FETs significantly [35, 57-59]. On the contrary, a relatively low work function metal like aluminum(Al) can enhance the electron injection and lead to n-type behavior for BP FETs [58, 60, 61]. However, this technique cannot solve the interfacial vdW gap problem.

Another way to reduce the contact resistance is using the method of surface charge transfer doping to the BP channel [62, 63]. Despite the fact that surface charge transfer doping can contribute to a pretty low R_C [62], the drain current modulation of the device is sacrificed in most cases. In addition, some of the doping effects even exhibit poor long-term reliability against ambient atmosphere [64]. Thus, a new technique must be invented to decrease the contact resistance of BP FETs.

Finally, since black phosphorus' type control is found to be thickness dependent [58] , a gate modulated p-n-like homojunction in BP is fabricated through a simple thickness engineering, which is compared to BP/WS₂ heterostructure P-N diode and reveals BP's potential in optoelectronics and photonics applications.

In this thesis, the introduction of black phosphorus and its development are presented in Chapter 1. The fabrication systems and measurement systems are introduced in Chapter 2. The material analysis of BP is presented in Chapter 3. Chapter 4 presents the fabrication process of the performance-optimized BP TFTs with orientation and contact engineering. The electrical properties will also be discussed in this chapter. Finally, the conclusion is given in chapter 5

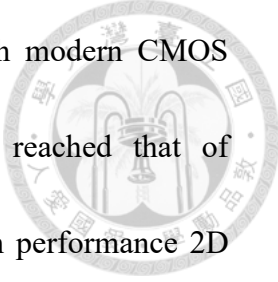
Chapter 2 Experiments

In this chapter, the fabrication systems will be first introduced. Then the measurement techniques for material analysis and device properties will be presented.

2.1 Fabrication Systems

2.1.1 Mechanical Exfoliation

To prepare 2D materials, different approaches have been used, such as mechanical exfoliation [9], chemical vapor deposition(CVD) [53, 65], and liquid-phase exfoliation [66]. Although the CVD method can produce large-scale and



homogeneous atomic layers of 2D materials, and is suitable with modern CMOS fabrication process, the quality of 2D thin film has not yet reached that of mechanically exfoliated 2D thin film [67]. Accordingly, most high performance 2D thin film transistors are made by mechanical exfoliation so far. Since black phosphorus flakes are found to chemically degrade upon exposure to ambient conditions, the transfer procedure was implemented in a glove box which is a sealed container and is used to remove solvents, water and oxygen inside the glove box. The details of mechanical exfoliation to fabricate rectangular BP are as follows. First, the blue Nitto tape was used to tear the bulk black phosphorus apart, as shown in Fig. 2.1 (a). Then, the blue Nitto tape with the black phosphorus crystallites on it was folded for several times in order to make the BP flakes thinner, as shown in Fig. 2.1 (b). It should be noted that there are some needle-shaped BP flakes on the Nitto tape which can be observed with naked eye and optical microscopy, as shown in Fig. 2.2 (a) and (b). By Raman measurement and TEM measurement in Chapter 3, the long sides of these needle-shaped BP flakes were confirmed to be the zigzag direction of the BP crystal. Next, the PDMS stamp was pressed onto the Nitto tape and then peeled off slowly, as shown in Fig. 2.1 (c). The PDMS stamp is a thin layer of commercially available viscoelastic material which is adhered to a glass side to facilitate handling, as shown in Fig. 2.3. In order to obtain rectangular-shaped BP thin film, the PDMS

stamp must aim at these needle-shaped BP flakes so that these flakes can be transferred onto the PDMS stamp. Finally, these thin flakes on the PDMS stamp can be transferred onto the SiO₂/Si substrate by simply putting the PDMS stamp on the SiO₂/Si substrate and then peeling it off slowly, as shown in Fig. 2.1 (d) and (e). After the substrate was taken out from the glove box, the substrate was immediately immersed in acetone for 1 hour in order to remove the adhesive residue. Then the sample was quickly passivated with PMMA to keep BP flakes from degrading in the ambient atmosphere [68]. Finally, BP thin films were checked carefully under the optical microscope to find out the BP nanosheets with rectangular shape and proper thickness, as shown in Fig. 2.4.

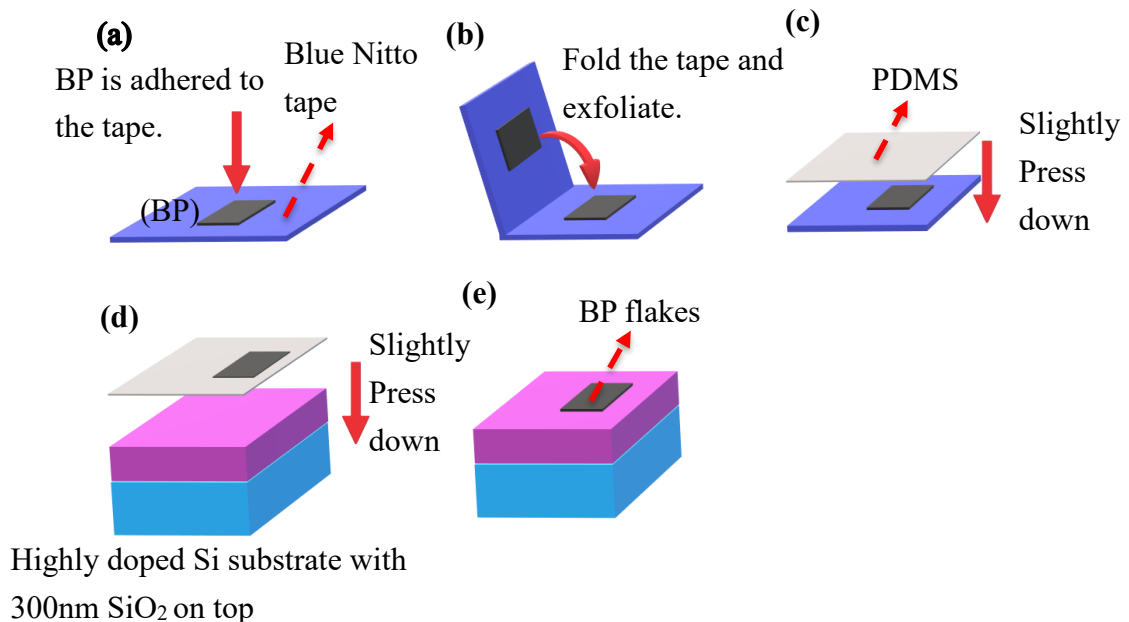
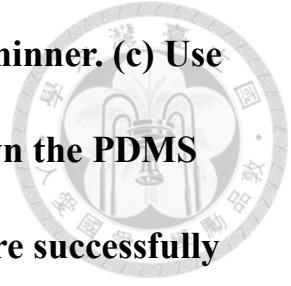


Fig. 2.1 Illustration of mechanical exfoliation process: (a) Bulk BP is adhered to the Blue Nitto tape, leave some BP flakes on the tape. (b)

Fold the tape numerous times to make the BP flakes thinner. (c) Use PDMS stamp as a second dry transfer. (d) Press down the PDMS stamp onto the Si/SiO₂ substrate. (e) BP thin films were successfully exfoliated onto the substrate.



(a)



(b)

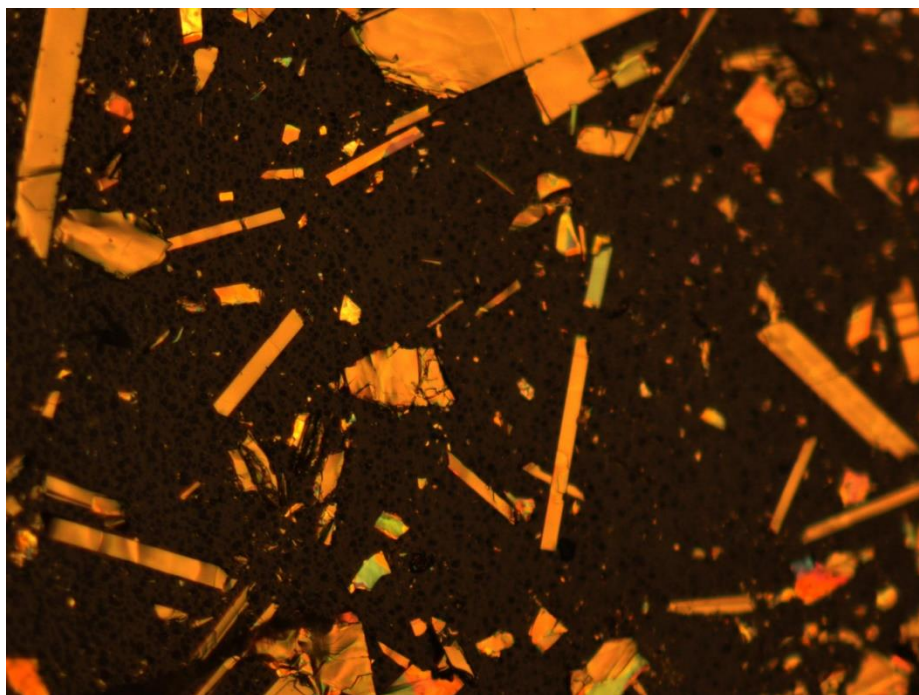


Fig. 2.2 Needle-shaped BP flakes on blue Nitto tape under (a) naked eye and (b) optical microscopy observation, respectively.



Fig. 2.3 The PDMS stamp used in this research.



Fig. 2.4 Exfoliated rectangular BP on 300nm SiO₂/Si substrate under optical microscopy. Scale bar is 20um.

2.1.2 Photolithography

Photolithography, also termed optical lithography or UV lithography, is a process used in microfabrication to pattern the thin film or the bulk of a substrate. It uses light to transfer a geometric pattern from a photomask to a light-sensitive chemical "photoresist", or simply "resist," on the substrate. A series of chemical treatments then either engraves the exposure pattern into, or enables deposition of a new material in the desired pattern upon the material underneath the photoresist.

In this research, NR9-1000PY negative photoresist (PR) was spun and coated on the silicon wafer as shown in Fig. 2.5(a), then the PR was soft baked for 1 minute to

evaporate solvent contained in the photoresist. The exposure system is the Karl Suss MJB4 Mask Aligner with 365 nm UV light, as shown in Fig. 2.5 (b). After 8 seconds exposure, the PR was hard baked for 150 seconds, then the RD-6 development solution was used to remove the unexposed portion of negative photoresist. 錯誤! 找不到參照來源。 lists the photolithography conditions.

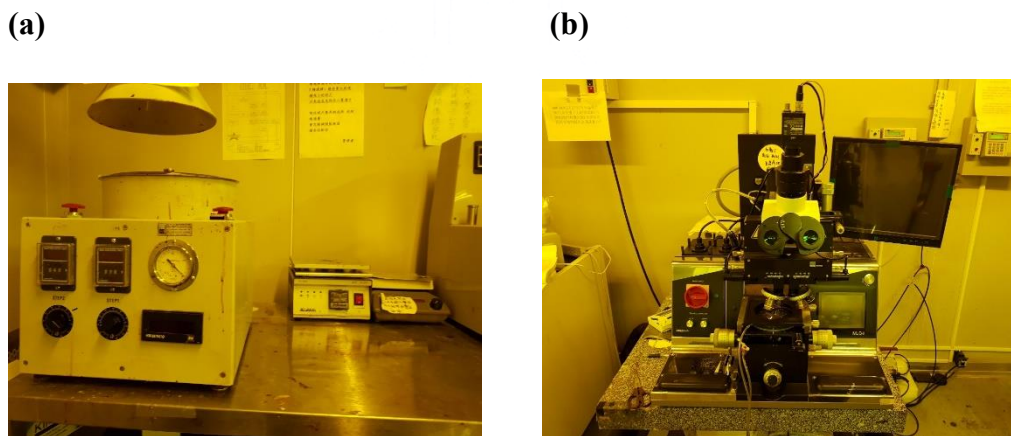
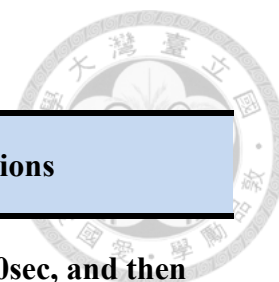


Fig. 2.5 (a) The spin-coater and hot plate used in this research (b) The exposure system used in this research

Table 2.1 photolithography conditions



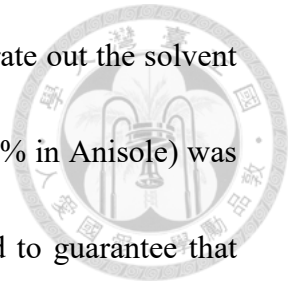
Pattern Formation	Conditions
Spinning and Coating(NR9-1000PY)	First 1000rpm 10sec, and then 4000 rpm 40 sec
Soft Bake	130°C 1min
Exposure	8 sec
Hard Bake	113°C 150sec
Development	6 sec

2.1.3 E-beam lithography

E-beam lithography is using the accelerated electron beam as the source to draw the required patterns on a surface covered by an electron-sensitive film called the resist. The electron beam changes the solubility of the resist, enabling selective removal of either the exposed or non-exposed regions of the resist by immersing it in a solvent for developing. The purpose, the same as the photolithography, is to create very small structures in the resist that can subsequently be transferred to the substrate material, often by etching.

In this research, 495PMMA A4 Resists (Solids: 4% in Anisole) was spun and

coated on the silicon wafer. The 5 minutes baking is used to evaporate out the solvent contained in the photoresist. Then 950PMMA A2 Resists (Solids: 2% in Anisole) was coated as a second layer to obtain the "undercut" which is applied to guarantee that the subsequent lift-off process goes smoothly, as shown in Fig. 2.6. Then the wafer coated with double layer was loaded into the chamber. The e-beam system is JSM7001F and the dosage of electron is $200\mu\text{C}/\text{cm}^2$. The e-beam process is operated under a vacuum of 9.6×10^{-5} Torr. After the dose of electron, the developer with a composition of 1 MIBK to 3 IPA is used to develop the resist. The process conditions of e-beam lithography are listed in **錯誤! 找不到參照來源。**



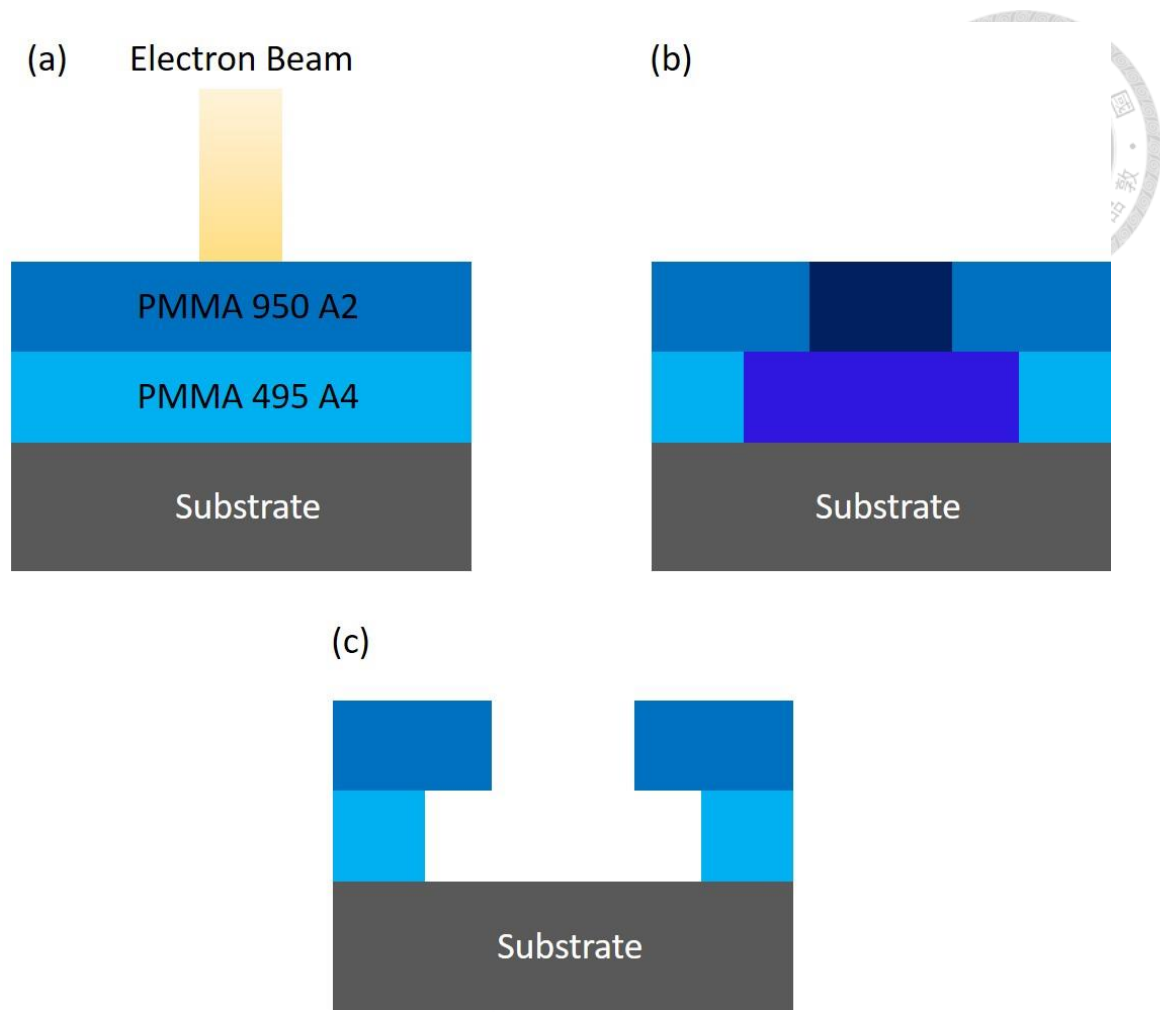


Fig. 2.6 Illustration of undercut PMMA formation: (a) After spin-coated bi-layer PMMA and soft bake, the photoresist is dosed by electron beam. (b) The darker colors represent the molecular chain scissored by electron beam. (c) The undercut structure is formed after development.



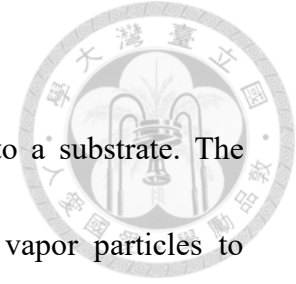
Fig. 2.7 The equipment of EBL process, JEOL JSM7001F.

Table 2.2 E-beam lithography conditions

Pattern Formation	Conditions
Spinning and Coating(495PMMA)	3000 rpm 30 sec
Bake	180°C 5min
Spinning and Coating(950PMMA)	3000 rpm 30 sec
Bake	180°C 5min
dosage of electron	200μC/cm²
Development(1:3 MIBK to IPA)	1min
Rinse(IPA)	30sec

2.1.4 Evaporation System

Evaporation is a common method to deposit a thin film onto a substrate. The source material is evaporated in a vacuum. The vacuum allows vapor particles to travel directly to the substrate, where they condense back to a solid state. In this research, metal is deposited by thermal evaporation or e-gun evaporation process under a vacuum of 4×10^{-6} Torr.



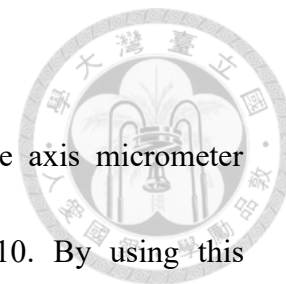
2.1.5 Rapid Thermal Annealing (RTA)

Rapid thermal anneal (RTA) is a subset of Rapid Thermal Processing. It is a process used in semiconductor device fabrication which consists of heating a single wafer for a period of time in order to affect its electrical properties. In this research, the RTA system is MILA-3000.



Fig. 2.8 The equipment of RTA system, MILA-3000

2.1.6 Heterostructure Fabrication System



Heterostructure fabrication system, which consists of three axis micrometer stage (Fig. 2.9) and optical microscopy, is shown in Fig. 2.10. By using this micromanipulator, BP can be transferred to the desired position of our substrate.

First, after the setup of our system, BP flakes are exfoliated onto the PDMS stamp. Next, the target sample is fixed on the stage (Fig. 2.10) by using double side tape and find the position that we want to fabricate heterostructure. Third, the PDMS stamp is inspected under the optical microscope to select the flake that we want to use. As the PDMS is transparent, we can see the target sample through it and thus it is possible to align the desired flake on the target sample where we want to transfer the flake with sub-micrometer resolution. Finally, as the desired position is reached, we can lower the glass slide with micromanipulator and let the PDMS stamp be adhered to the target sample to fabricate heterostructure.

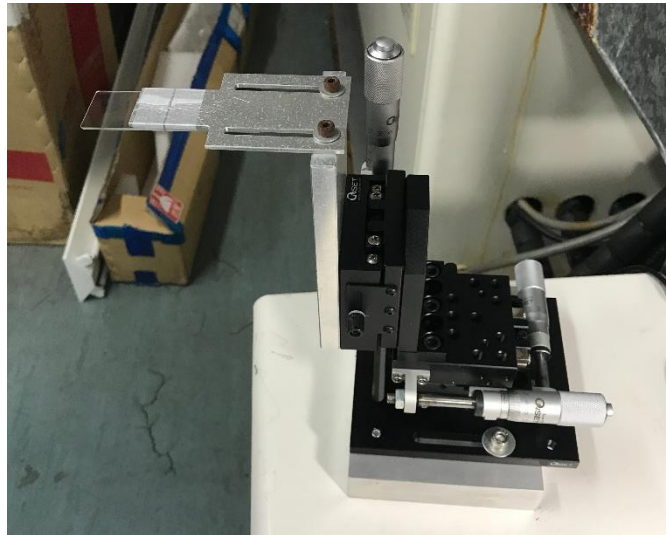


Fig. 2.9 Three axis micrometer stage.

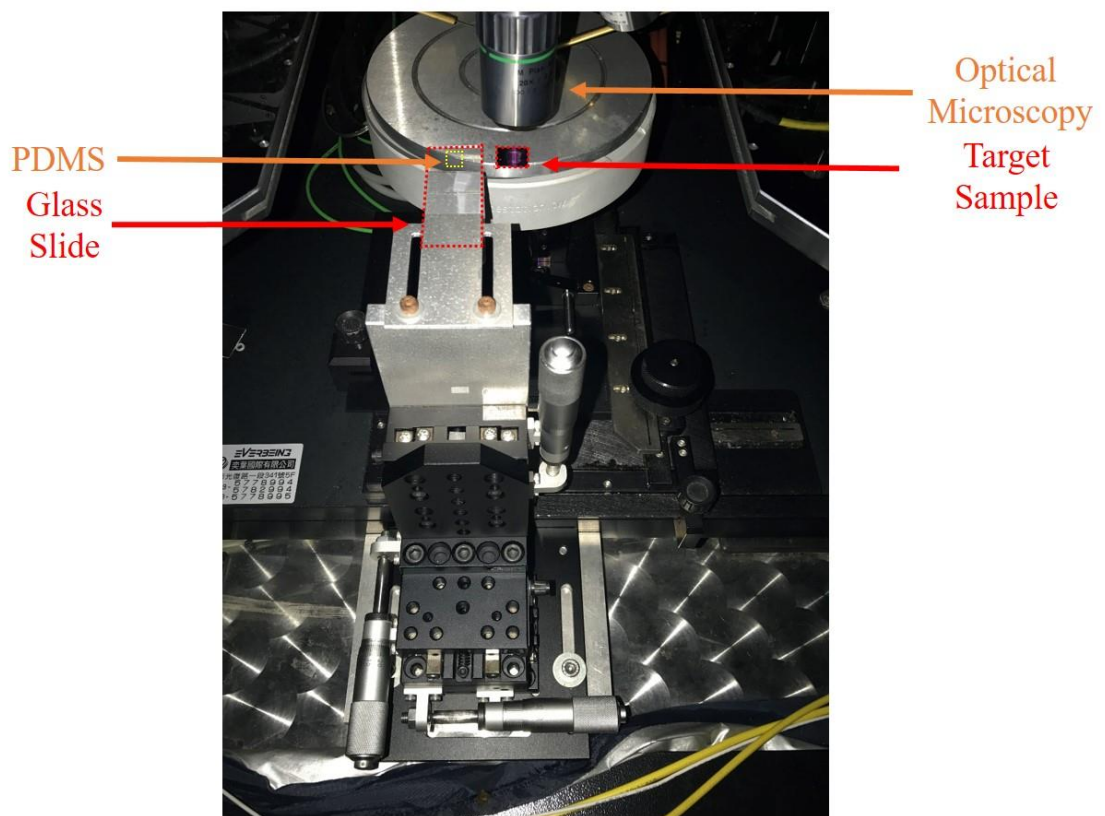


Fig. 2.10 Heterostructure fabrication system.

2.2 Measurement Techniques

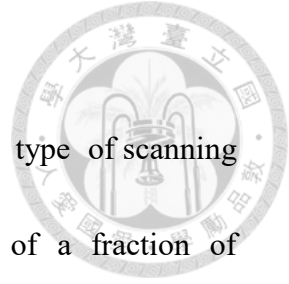
2.2.1 Optical Microscopy (OM)

For mechanically exfoliated BP, it's important to find BP flake with appropriate thickness and size. The film is inspected under the optical microscope and the level of contrast depends on the thickness of the film and the oxide layer. Just in analogy with graphene, the color contrast between BP nanosheets and the underlying SiO₂ is due to the interference of different wavelengths through the thin film and SiO₂. It means that optical imaging offers the possibility of simple, rapid and non-destructive characterization of large-area samples [69].



Fig. 2.11 The optical microscopy used in this research.

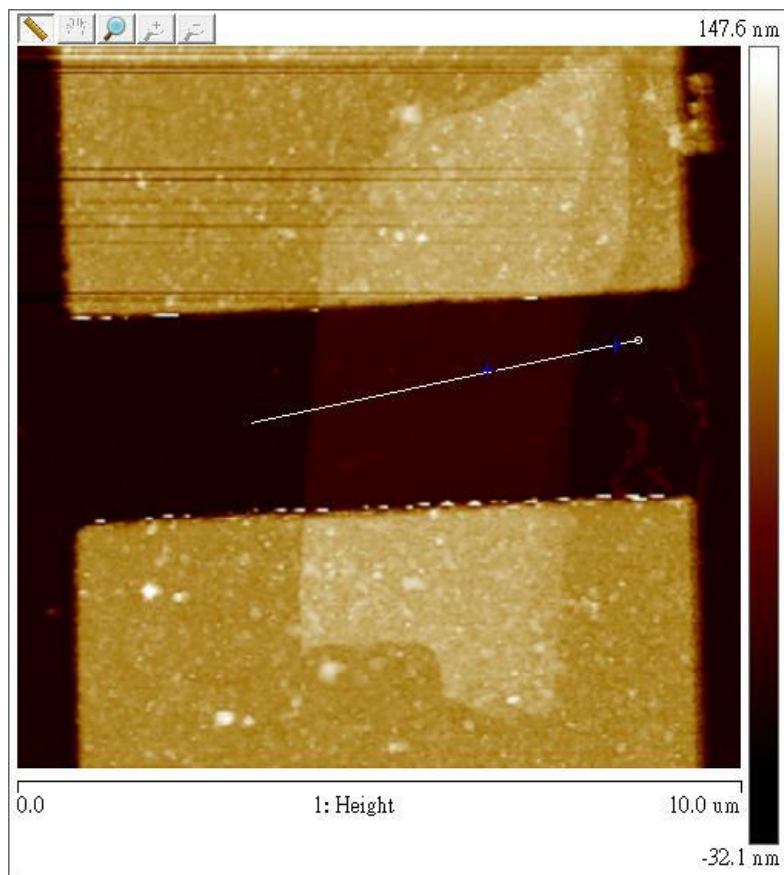
2.2.2 Atomic Force Microscopy (AFM)



Atomic force microscopy (AFM) is a very high-resolution type of scanning probe microscopy, with demonstrated resolution on the order of a fraction of a nanometer, more than 1000 times better than the optical diffraction limit.

In this research, AFM is used to check the thickness of BP nanosheets by standard tapping mode, which relies on the decreasing of the oscillation amplitude when the tip comes close to the surface.

(a)



(b)

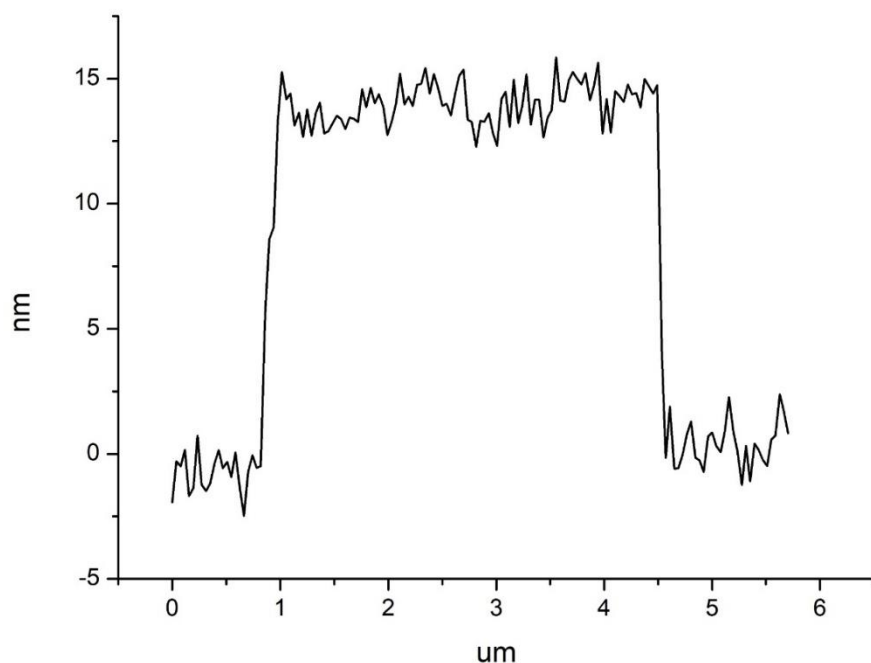


Fig. 2.12 (a) and (b) indicates that the thickness of this BP nanosheet is roughly 15nm.

2.2.3 Raman Spectroscopy

Raman spectroscopy is a spectroscopic technique used to observe vibrational, rotational, and other low-frequency modes in a system. The laser light interacts with molecular vibrations, phonons or other excitations, resulting in the energy of the laser photons being shifted up or down. Therefore, the shift in energy gives information about the vibrational modes in the system.

In this research, 532nm laser is used in Raman measurement. It gives the direction information of BP due to its anisotropic property.



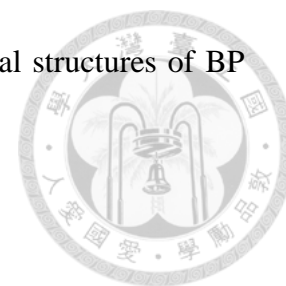
Fig. 2.13 The equipment of Raman measurement used in this research.

2.2.4 X-ray Diffraction (XRD)

X-ray crystallography is a technique used for determining the atomic and molecular structure of a crystal, in which the crystalline atoms cause a beam of incident X-rays to diffract into many specific directions. By measuring the angles and intensities of these diffracted beams, a crystallographer can produce a three-dimensional picture of the density of electrons within the crystal. From this electron density, the mean positions of the atoms in the crystal can be determined, as well as their chemical bonds, their disorder, and various other information.

In this research, the wavelength of the X-ray is 1.54\AA . The BP bulk is grounded

into powder in order to reduce the non-ideal scattering. The crystal structures of BP bulk can be determined from XRD measurement.



2.2.5 X-ray Photoelectron Spectroscopy (XPS)

X-ray Photoelectron Spectroscopy (XPS) is a quantitative spectroscopic technique that measures the elemental composition, empirical formula, chemical state and electronic state of the elements that exist in a material. XPS spectra are obtained by irradiating a material with a beam of X-rays while simultaneously measuring the kinetic energy and number of electrons that escape from the top 1 to 10 nm of the material being analyzed.

In XPS, photons with sufficient energy E_{photon} are absorbed by a system causing core electrons escaped from the sample. If the energy of the photons is larger than the binding energy of the electron E_{binding} , the excess energy will be converted to kinetic energy of the emitted photoelectron, as shown in Fig. 2.14. The binding energy of the core level electron can be calculated according to

$$E_{\text{binding}} = E_{\text{photon}} - (E_{\text{kinetic}} + \phi_{\text{spec}}) \quad (2.1)$$

where E_{binding} is the binding energy of the core electron from the Fermi level, E_{photon} is the energy of the X-ray photons being used, E_{kinetic} is the kinetic energy of the electron measured by the instrument and ϕ_{spec} the work function of the spectrometer.

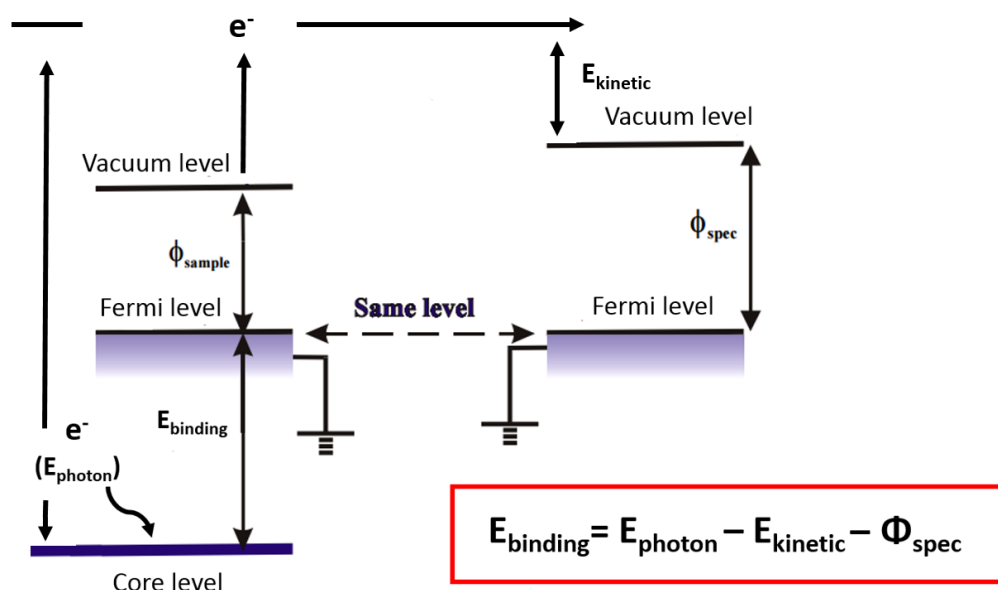


Fig. 2.14 Energy level diagram of the emitted photoelectron.

In this research, Al-K α (1486.6eV) is used as a X-ray source. The spot size is 400 μm and the analysis binding energy values is from 123eV to 143eV. The XPS measurement is used to understand the oxidation rate of BP bulk by measuring the ratio between the intensity of P₂O₅ and phosphorus.

2.2.6 Ultraviolet Photoemission Spectroscopy (UPS)

There are two major technique to measure photoemission spectra of atoms, i.e., Ultraviolet photoemission spectroscopy (UPS) and X-ray Photoelectron Spectroscopy (XPS). The basic theory of the photoemission is illustrated in Fig. 2.15 (a) and (b).

The ultraviolet photons to have lower energies that can be used to study the molecular orbital energies in the valence band region. Through the analysis of escaped

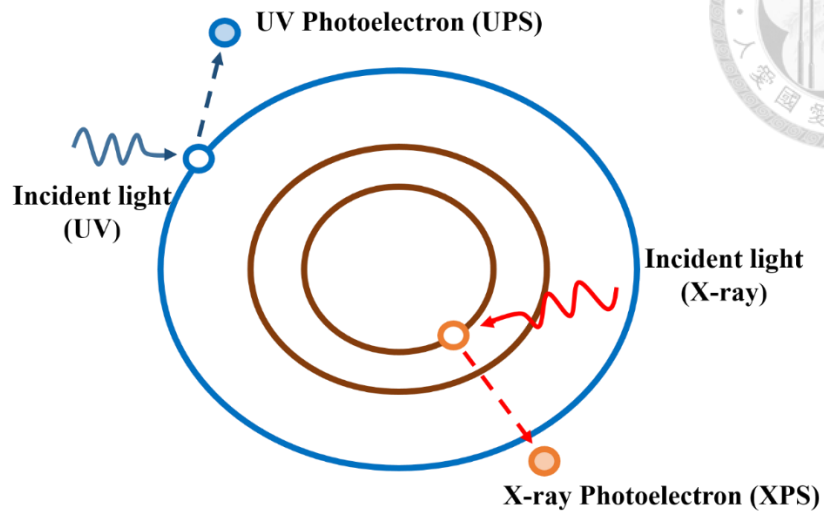
kinetic energy of photoelectrons, the binding energy of the specific molecular orbital energy can be calculated. Besides, the work function at the surface of black phosphorus can be obtained from Eq. (2.2).

$$E_{binding} = E_{photon} - (E_{kinetic} + \phi) \quad (2.2)$$

where $E_{binding}$ is the binding energy of the electron, E_{photon} is the energy of the UV, $E_{kinetic}$ is the kinetic energy of the electron and ϕ is the work function of the material.

In this research, the fermi level and work function differences before and after oxidation is presented.

(a)



(b)

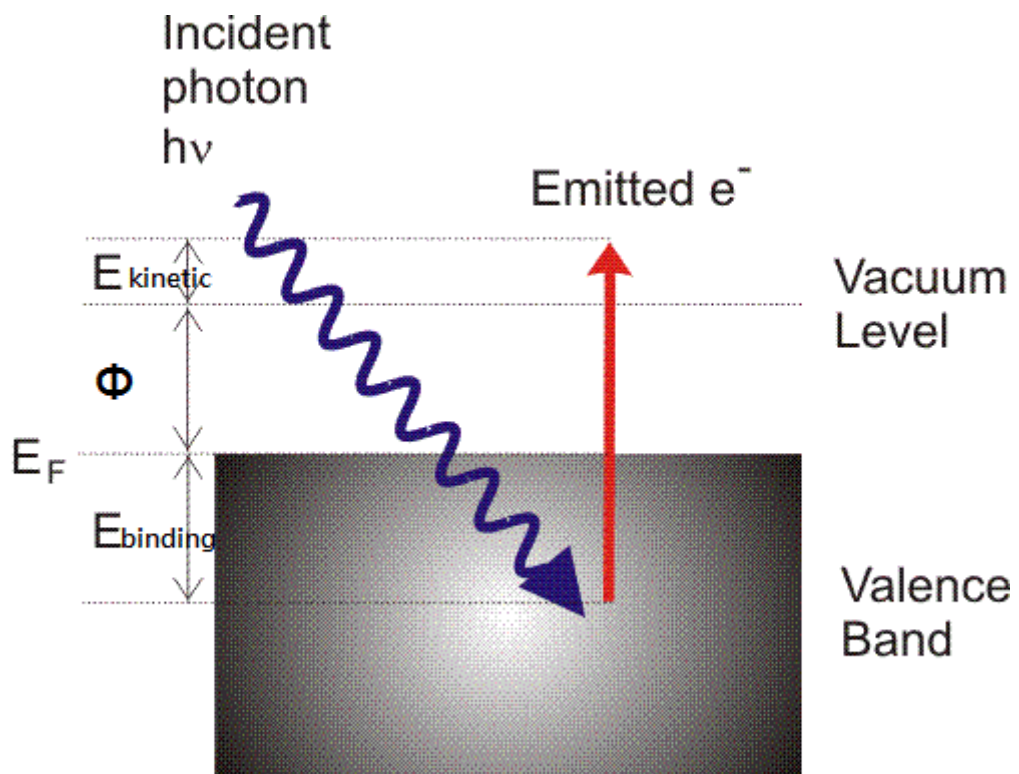
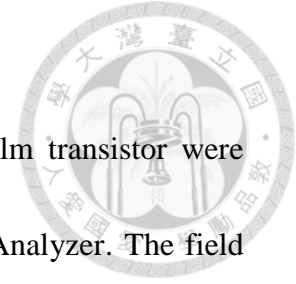


Fig. 2.15 (a) and (b) Schematic diagram showing how photoelectrons are generated.

2.2.7 Current – Voltage Characteristics

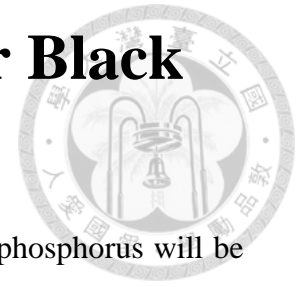


The current-voltage (I-V) characteristics of the BP thin film transistor were measured by Agilent B1500A Semiconductor Device Parameter Analyzer. The field effect mobility (μ_{EF}) of the TFT can be obtained by the transconductance (g_m) with low V_D .

$$\mu_{EF} = \frac{g_m}{C_i \frac{W}{L} V_D} \quad (2.2)$$

where $W(L)$ is the channel width (length), C_i is the capacitance per unit area. V_T can also be determined using linear extrapolation of the $I_D - V_G$ plot.

Chapter 3 Material Analysis for Black Phosphorus



In this chapter, the material analysis for the exfoliated black phosphorus will be investigated in details.

3.1 Crystal Structure of Black Phosphorus

It is important to confirm the crystalline structure of BP before fabricating a TFT device. By studying its X-ray diffraction pattern, as shown in Fig 3.1(a), the strong diffraction peaks at 16.9° , (002) plane, and 34.2° , (004) plane, were recognized, following the weaker peaks at 26.5° , 40.1° , 52.4° , 56° and 56.7° , corresponding to (012), (014), (006), (105) and (016) planes, respectively. The distance between the atomic planes in the BP bulk can also be calculated from the XRD pattern using the Bragg equation:

$$2d\sin\theta = n\lambda \quad (3.1)$$

where d is the distance between the atomic planes, θ is the Bragg scattering angle, n is the diffraction order and λ is the wavelength of incident X-ray. Since the crystalline form of black phosphorus is orthorhombic [70, 71], the reciprocal lattice vectors (hkl) can be obtained from the theoretical lattice constants (abc) and Eq. (3.2):

$$\frac{1}{d^2} = \frac{h^2}{a^2} + \frac{k^2}{b^2} + \frac{l^2}{c^2} \quad (3.2)$$

After the peaks and their corresponding reciprocal lattice vectors were

determined, the lattice constants can be calculated, as shown in Fig. 3.1 (b) and (c).

The lattice constants for bulk black phosphorus are $a = 3.31 \text{ \AA}$, $b = 4.37 \text{ \AA}$, and $c = 10.48 \text{ \AA}$, corresponding to zigzag, armchair and out of plane directions respectively

and are in good agreement with the previous experimental values [30, 72, 73]. The

atomic density is $5.26 \times 10^{22} \text{ \#/cm}^3$, and the density of bulk BP is 2.7 g/cm^3 . Because

the unit cell contains two layers, the lattice constant $c = 10.48 \text{ \AA}$ indicates that the

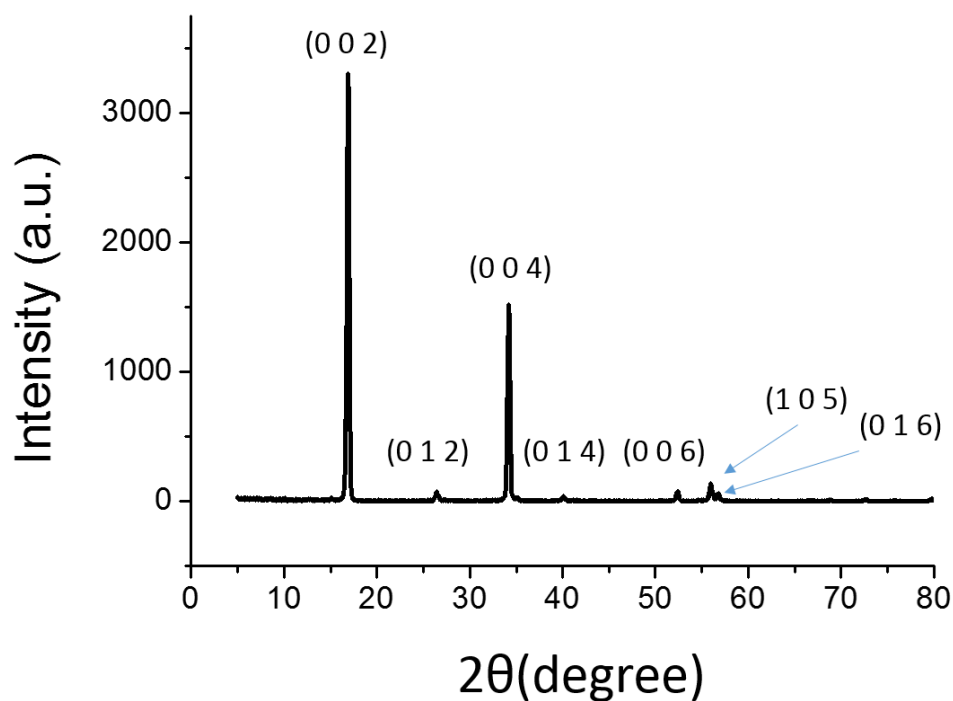
average interlayer spacing is close to 5.24 \AA . Therefore, the number of layers for

exfoliated BP thin films can be easily determined if the thickness of the BP

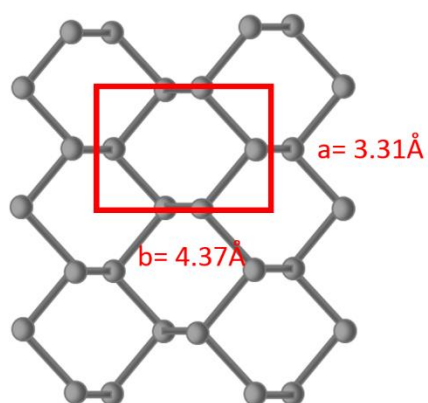
nanosheets is known.



(a)



(b)



(c)

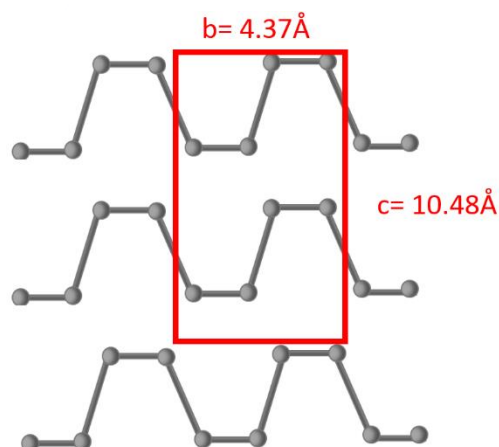


Fig. 3.1 (a) The X-ray diffraction pattern of bulk BP crystal.

Schematic of the unit cell of BP. (b) Top View. (c) Lateral view.



3.2 Characterization of Black Phosphorus Film

Thickness

In this section, the BP flakes with appropriate thickness are chosen under optical microscope. After fabrication process and measurement, atomic force microscope is used to precisely determine the exact layer number of BP nanosheets.

3.2.1 Optical Microscopy (OM)

For mechanically exfoliated BP, it's important to find BP flakes with proper thickness. The film is scrutinized under the optical microscope while the level of color contrast depends on both the thickness of the film and the underlying oxide layer. The color contrast between BP flakes and the bottom SiO₂ is due to the interference of different wavelengths through the thin film and SiO₂, just in analogy with graphene, which means that optical imaging is a simple, rapid and non-destructive method to characterize the thickness of exfoliated BP films [69].

After measuring several BP flakes by AFM, the relationship between the color of BP nanosheets under optical microscope and the thickness of BP thin films is found. Table 3.1 lists the color of BP flake as a function of its thickness on a 300 nm SiO₂/Si substrate. As the thickness decreases, the color changes from red to green as a result of optical interference effects with the oxide. Although the color seems similar when

the BP nanosheet is thinner than 20 nm, the transparency of the flake can be used to roughly identify the number of layers.

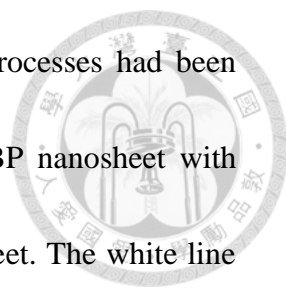


Table 3.1 Thickness dependence of color for BP film on 300 nm SiO₂/Si substrate under optical microscopy.

Thickness	Color
<20nm	green
20nm~30 nm	yellow-green
30nm~60 nm	yellow
60nm~80 nm	orange
>80nm	red

3.2.2 Atomic Force Microscope (AFM)

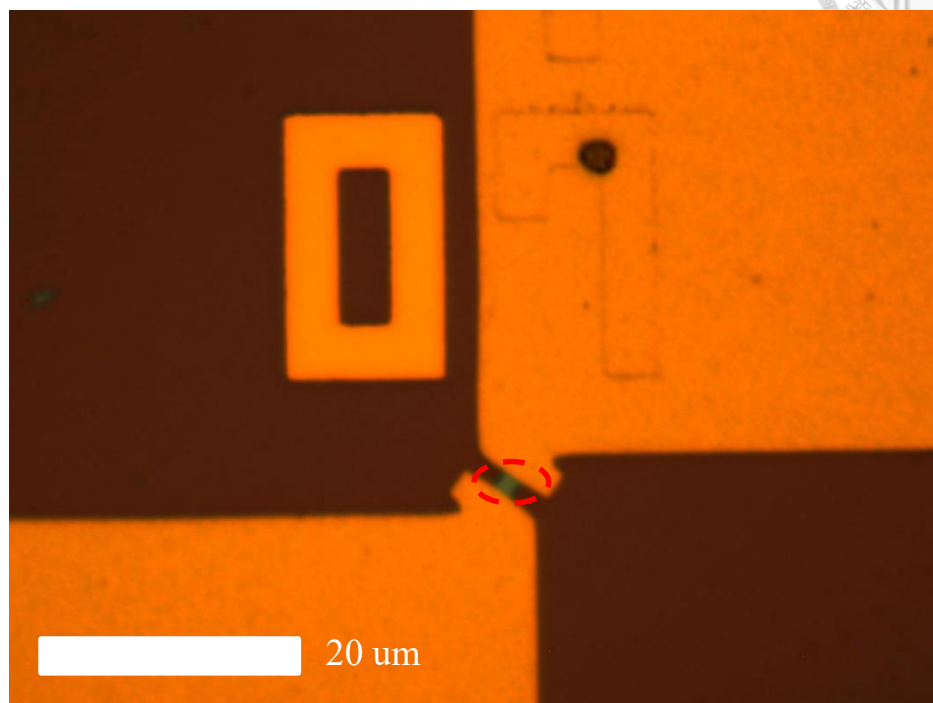
According to chapter 3.1, the thickness of a phosphorene layer is 0.52 nm. Therefore, it is easy to identify the layer number by measuring the thickness of the BP nanosheet. In this research, the standard tapping mode of AFM is used. It provides a more accurate measurement than that of the optical microscope. However, since the process of this measurement is pretty time-consuming, and black phosphorus will gradually degrade due to the long time exposure to ambient atmosphere, the thickness



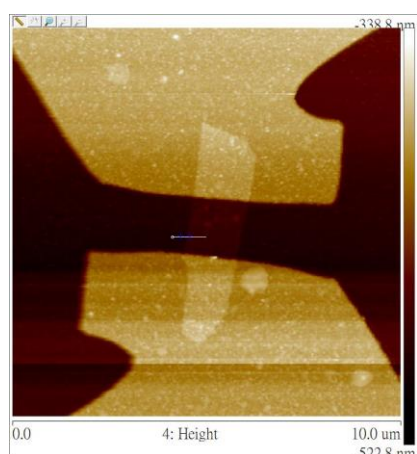
identification by AFM would not be conducted until the other processes had been completed. Fig. 3.2 (a) shows the OM image of an exfoliated BP nanosheet with green color. Fig. 3.2 (b) shows the AFM image of this BP nanosheet. The white line in (b) marks the position of the line profiles shown in Fig. 3.2 (c). The thickness of this BP nanosheet is about 14 nm, which is consistent with Table. 3.1 and implies that the layer number is roughly about 28. Fig. 3.3 (a) shows another exfoliated BP nanosheet with yellow color, and the AFM result of this BP flake is also shown in Fig. 3.3 (b) and (c). Finally, a BP nanosheet with both green and yellow color is shown in Fig. 3.4 (a), and the AFM results of the green and yellow parts of this BP thin film are shown in Fig. 3.4 (b) 、(c) and (d) 、(e), respectively. These AFM results indicate that the thickness of an mechanically exfoliated BP nanosheet can be really non-uniform, and the large surface roughness in few-layered phosphorene samples can lead to the measurement error in AFM. Besides, the scanning rate of AFM is slow as compared to the fast degradation rate of few-layered phosphorene in ambient conditions. As a result, the rapid, non-intrusive and accurate method for identifying the thickness of a BP nanosheet is required.



(a)



(b)



(c)

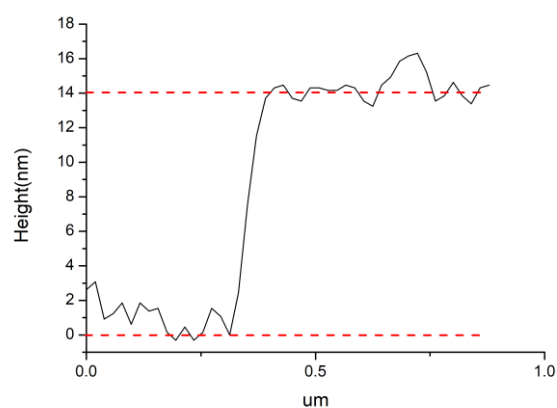
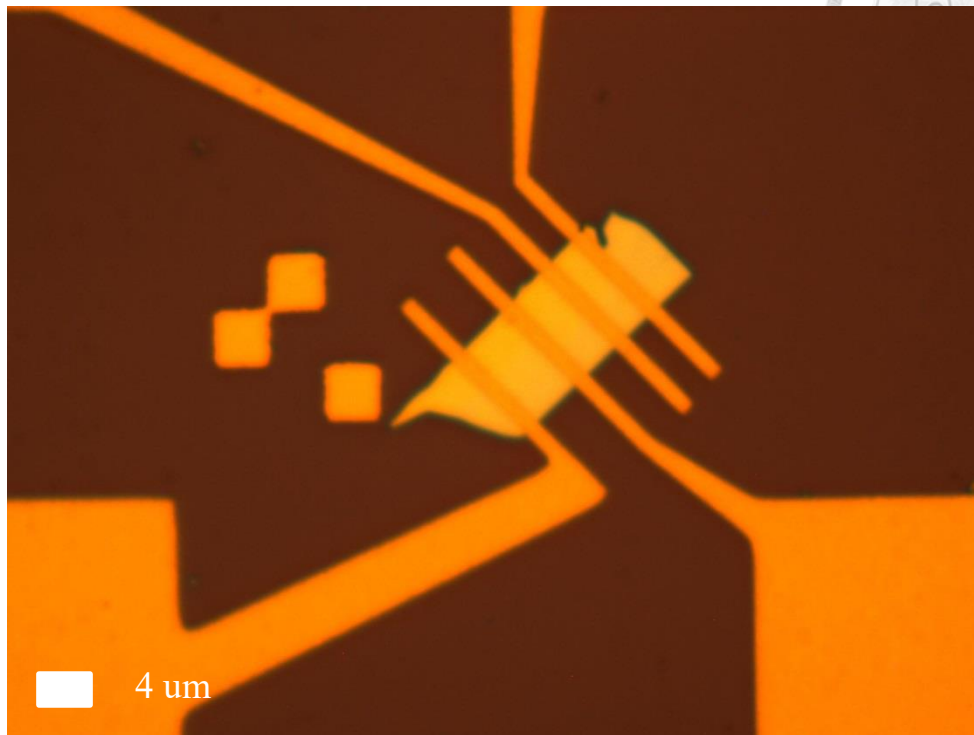
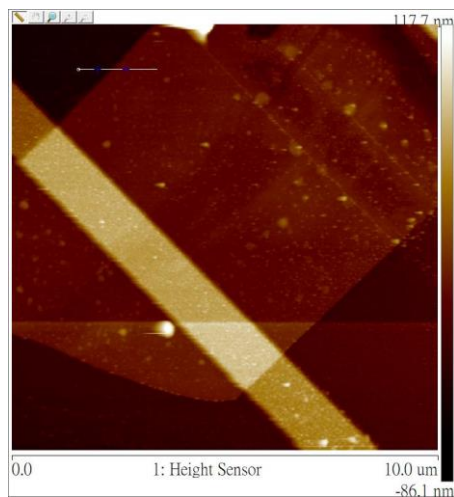


Fig. 3.2 (a) The OM image of an exfoliated BP nanosheet with green color. (b) The AFM image of this BP nanosheet. The white line marks the position of the line profiles shown in (c). (c) AFM line profile for the thickness of BP. The thickness of this BP nanosheet is about 14 nm.

(a)



(b)



(c)

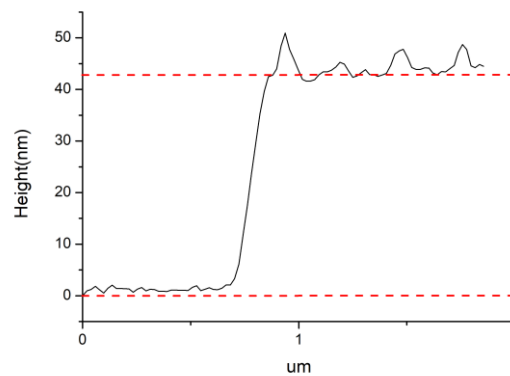
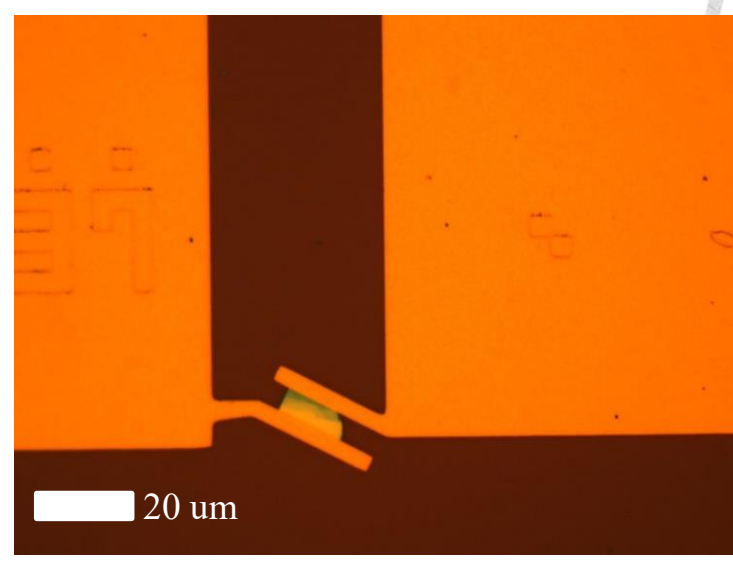


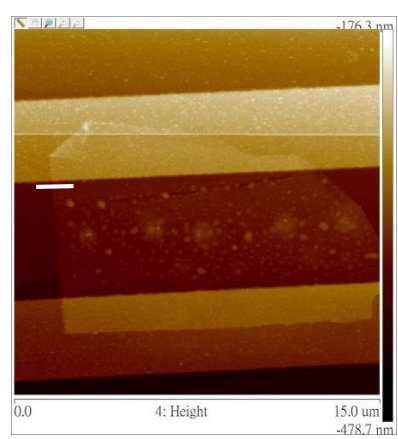
Fig. 3.3 (a) The OM image of an exfoliated BP nanosheet with yellow color. (b) The AFM image of this BP nanosheet. The white line marks the position of the line profiles shown in (c). (c) AFM line profile for the thickness of BP. The thickness of this BP nanosheet is about 43 nm.



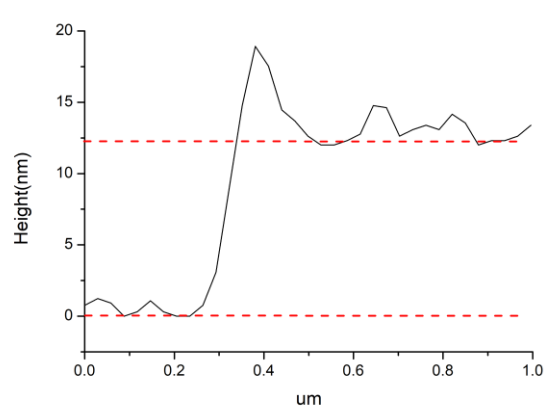
(a)



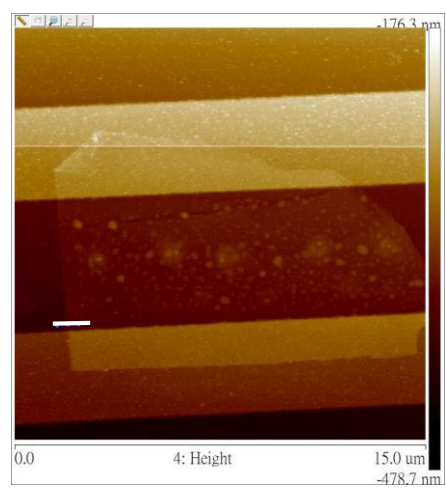
(b)



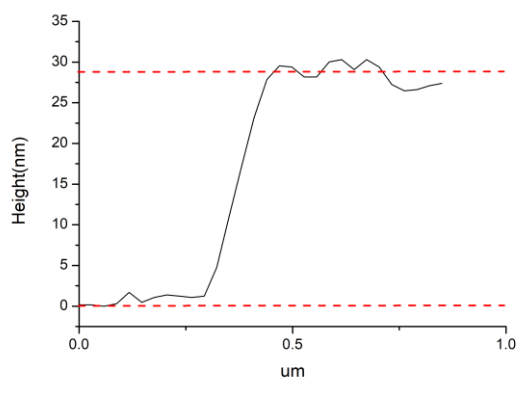
(c)



(d)



(e)



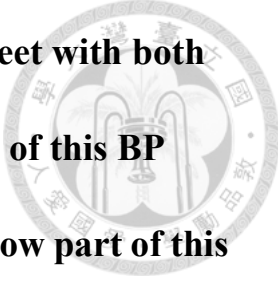
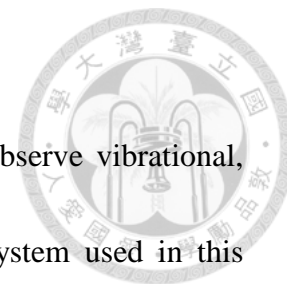


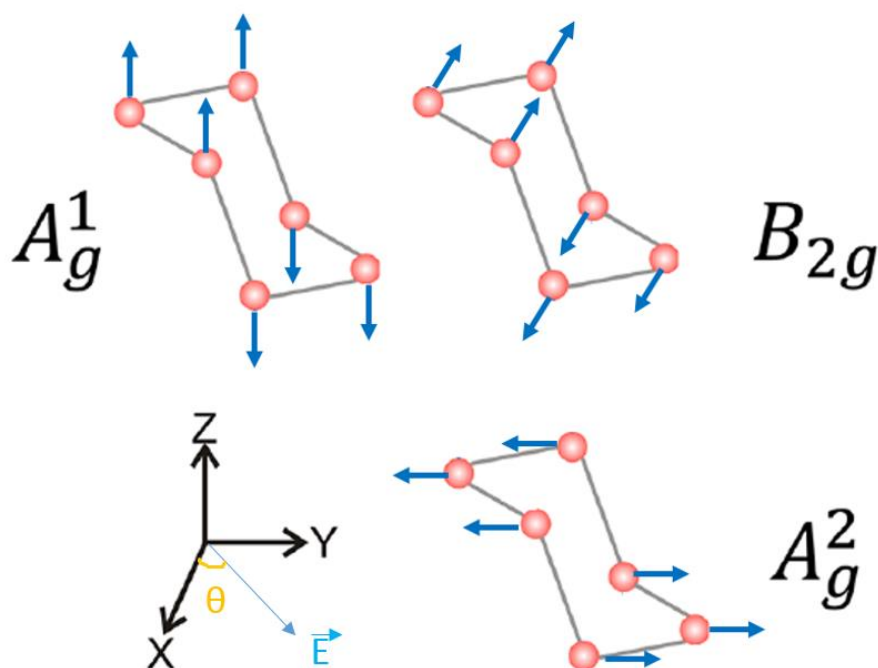
Fig. 3.4 (a) The OM image of an exfoliated BP nanosheet with both green and yellow color. (b) and (d) The AFM image of this BP nanosheet. The white line, which is at the green and yellow part of this BP nanosheet, respectively, marks the position of the line profiles shown in (c) and (e), respectively. (c) and (e) AFM line profile for the thickness of BP. The thickness of the green and yellow part of this BP nanosheet is about 12.4 nm and 29 nm, respectively.

3.3 Raman Spectroscopy



Raman spectroscopy is a spectroscopic technique used to observe vibrational, rotational, and other low-frequency modes in a material. The system used in this research is a 532nm laser. Since it has been reported that the high power laser-induced heat might damage the lattice structure of BP, a low laser power of 15mW was used to avoid the laser-induced degradation [74].

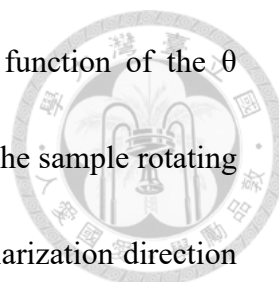
Unlike in TMDCs semiconductors, where Raman mode frequency has a monotonic dependence on the layer number, the black phosphorus has a non-monotonic dependence owing to the complicated Davydov-related effects [75, 76]. The three characteristic Raman modes, A_g^1 , B_{2g} and A_g^2 , can be observed under the typical backscattering configuration, as shown in Fig. 3.5, corresponding to the out-of-plane vibration A_g^1 (362cm^{-1}), in-plane vibration along the zigzag B_{2g} (439cm^{-1}) and armchair A_g^2 (467cm^{-1}), respectively [77].



ACS Nano, 2014, 8 (9), pp 9590–9596

Fig. 3.5 Schematic plot showing the vibration directions of A_g^1 , B_{2g} , and A_g^2 modes. The atoms oscillate along the z (out-of-plane), x (zigzag) and y (armchair) directions, respectively.

The anisotropic behavior of BP is probed by angular dependent Raman spectra [78-85]. The incident light was always polarized along the horizontal direction, as shown in Fig. 3.6 (a). θ is the angle between the zigzag direction of the BP with respect to the polarization direction of the incident beam as indicated in Fig. 3.6. The angle dependent intensities of A_g^1 , B_{2g} , and A_g^2 modes were measured from 0° to 180° , considering the two-fold rotational symmetry of BP along the incident direction of the laser. Although the peak positions are independent of the orientation of BP, it is



found that the Raman intensities show periodic oscillation as a function of the θ angle. The intensity of A_g^1 mode didn't appear much difference as the sample rotating because the vibration direction was always perpendicular to the polarization direction of the incident light. The A_g^2 mode reached its minimum intensity when the rotation angle was at 0° and the maximum intensity arose when the rotation angle was at 90° . The B_{2g} mode exhibited a 90° period and achieved its maximum intensity at both 40° and 130° , as shown in Fig. 3.6 (b) and Fig. 3.7 [78]. The intensities of the Raman modes are determined by the Raman tensors and the scattering geometry. The Raman tensors of A_g and B_{2g} modes can be expressed as:

$$R(A_g) = \begin{pmatrix} |a|e^{i\phi_a} & 0 & 0 \\ 0 & |b|e^{i\phi_b} & 0 \\ 0 & 0 & |c|e^{i\phi_c} \end{pmatrix}$$

$$R(B_{2g}) = \begin{pmatrix} 0 & 0 & |f|e^{i\phi_f} \\ 0 & 0 & 0 \\ |f|e^{i\phi_f} & 0 & 0 \end{pmatrix}$$

where a, b, c and f represent the amplitude of respective vibration modes. Notice that the null components in Raman tensors are due to the symmetry of the BP crystal structure. Considering parallel configuration, the polarization vectors of light can be expressed as:

$$\hat{e}_l = \hat{e}_s = (\cos\theta \quad 0 \quad \sin\theta)$$

where the angle θ is measured with respect to the zigzag direction.

Raman scattering intensity S for parallel polarization configuration is defined as

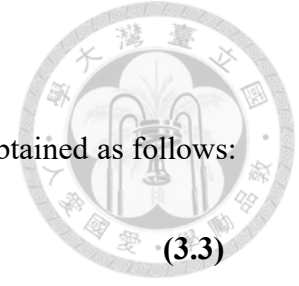
$$S \propto |\hat{e}_t * R * \hat{e}_s|^2$$

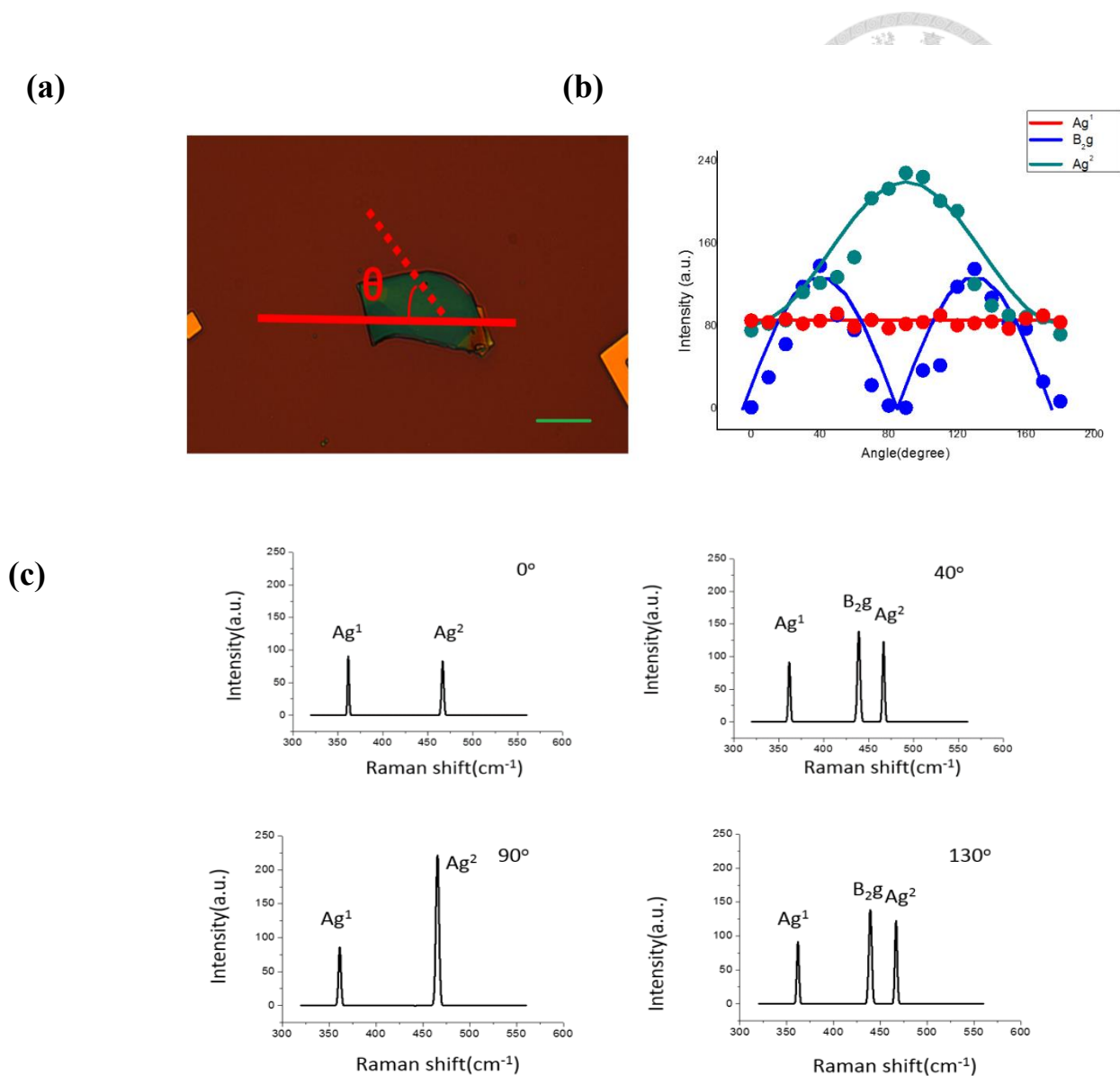
Then the relationship between intensity and rotation angle can be obtained as follows:

$$S(Ag) \propto (|a|e^{i\phi_a} \times \cos^2\theta + |c|e^{i\phi_c} \times \sin^2\theta)^2 \quad (3.3)$$

$$S(B_{2g}) \propto (|f|e^{i\phi_f} \times \sin 2\theta)^2 \quad (3.4)$$

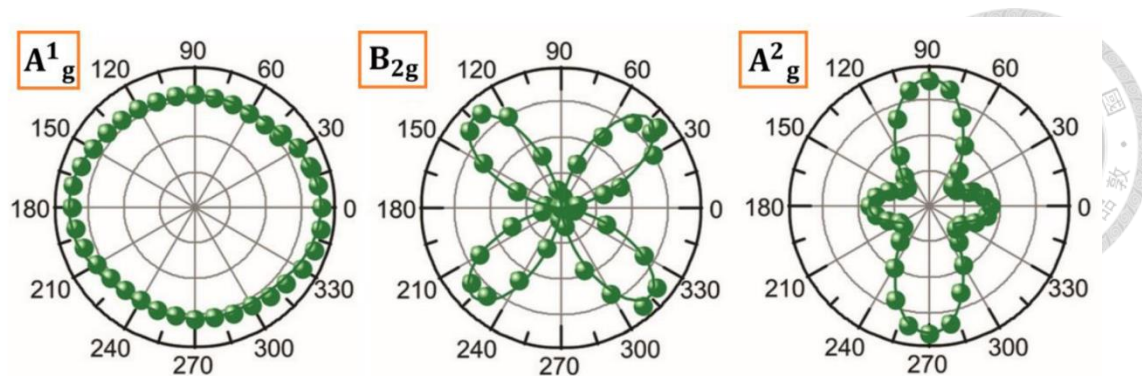
Since the Raman tensor parameter a is smaller than that of the parameter c under 532 nm laser excitation, Eq. (3.3) shows that S(Ag) reaches its minimum a^2 at $\theta=0^\circ$ and reaches its maximum c^2 at $\theta=90^\circ$. Eq. (3.4) indicates that S(B_{2g}) reaches its maximum when θ is 45° or 135° and exhibits a 90° period, which is consistent with the experimental result, as shown in Fig. 3.6 (b).





Po-Yen Chang, Master Thesis, Top-gated Black Phosphorus Thin Film Transistor with High-K Dielectric Layer (2017).

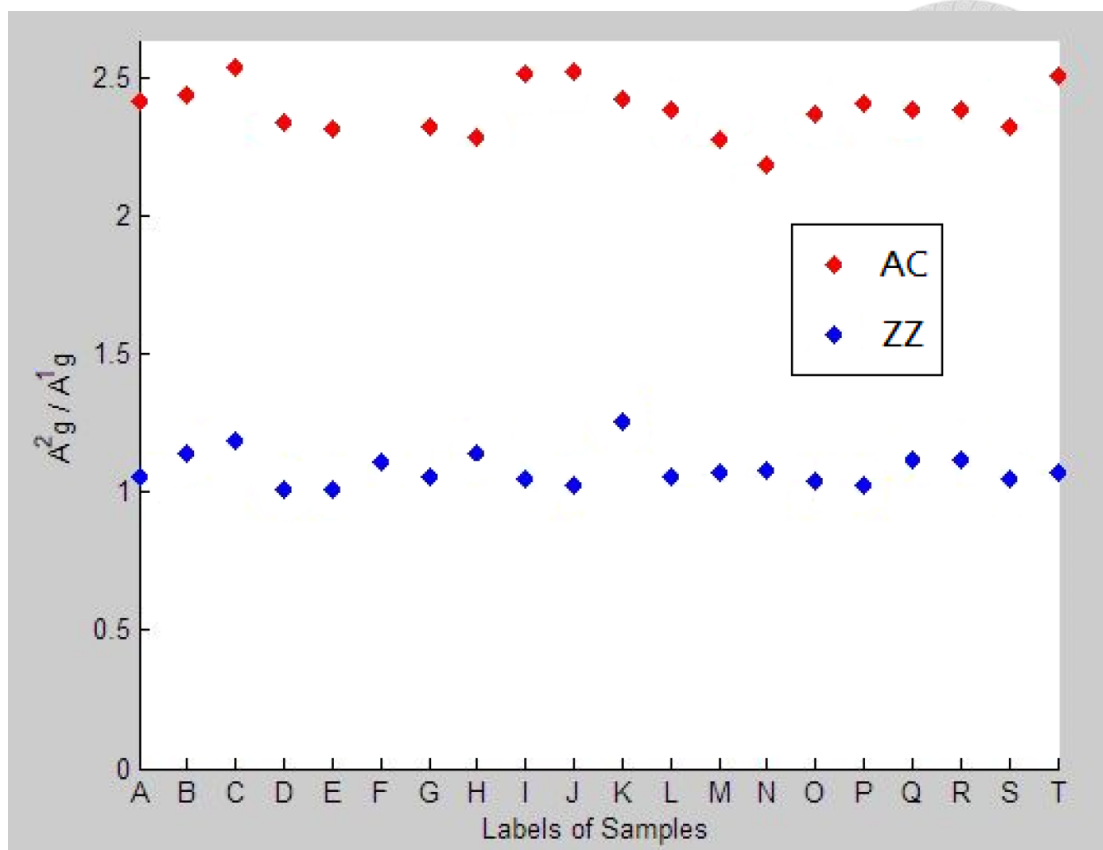
Fig. 3.6 (a) Optical image of a BP flake. θ is the angle between the zigzag crystallographic direction and polarization direction of incident laser. The scale bar is $10 \mu m$. (b) Polarization dependence of Ag^1 , B_{2g} , and Ag^2 modes. The solid curves are the theoretical value and the dots are the experimental results. (c) Angle dependent Raman spectra for BP. The three characteristic Raman modes, Ag^1 ($362cm^{-1}$), B_{2g} ($439 cm^{-1}$) and Ag^2 ($467 cm^{-1}$), can be observed.



Nanoscale, 2015, 7, 18708

Fig. 3.7 The polar plots of Raman intensity for each Raman vibration mode with 532 nm excitation.

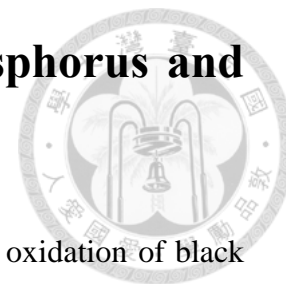
To determine the crystal orientation of rectangular BP, the intensity ratio of A_g^2 to A_g^1 can be used, as shown in Fig. 3.8, 20 rectangular BP samples (labeled as A~T) were selected for Raman measurements. It can be indicated that for any sample, the intensity ratio of the AC direction is always larger than 2, while the intensity ratio of the ZZ direction is approximately close to 1. In fact, the average intensity ratios of the AC and ZZ directions are 2.40 and 1.08, respectively, and their corresponding standard deviations are 0.103 and 0.061. This means that for BP thin films with 532 nm laser excitation, as long as the incident polarization angle at which the B_{2g} mode disappears is found, the intensity ratio of A_g^2 to A_g^1 can be used to distinguish the AC and ZZ directions of BP.



Yao Hsiao, Master Thesis, Black phosphorus with unique rectangular shape and its anisotropy for electronics and optoelectronics (2018).

Fig. 3.8 The Raman intensity ratios of A_g^2 to A_g^1 vibration modes for 20 rectangular BP samples (labeled as A~T). The polarizations of the 532 nm laser excitation are along AC and ZZ directions. The average intensity ratios of the AC and ZZ directions are 2.40 and 1.08, respectively.

3.4 XPS and UPS Analysis of Black Phosphorus and Gold-Germanium alloy



In this section, XPS is used to check the bond variation after oxidation of black phosphorus and Germanium. Eventually, UPS is used to determine the energy state and work function of phosphorene and Gold-Germanium alloy.

3.4.1 X-ray Photoelectron Spectroscopy (XPS)

In XPS, photons with sufficient energy E_{photon} are absorbed by a system causing core electrons escaped from the sample. If the energy of the photons is larger than the binding energy of the electron E_{binding} , the excess energy will be converted to kinetic energy of the emitted photoelectron, as shown in Fig. 3.9. The binding energy of the core level electron can be calculated according to

$$E_{\text{binding}} = E_{\text{photon}} - (E_{\text{kinetic}} + \phi_{\text{spec}})$$

(3.5)

where E_{binding} is the binding energy of the core electrons, E_{photon} is the energy of the incident X-ray photons, E_{kinetic} is the kinetic energy of the electrons measured by the instrument and ϕ_{spec} is the work function of the spectrometer.

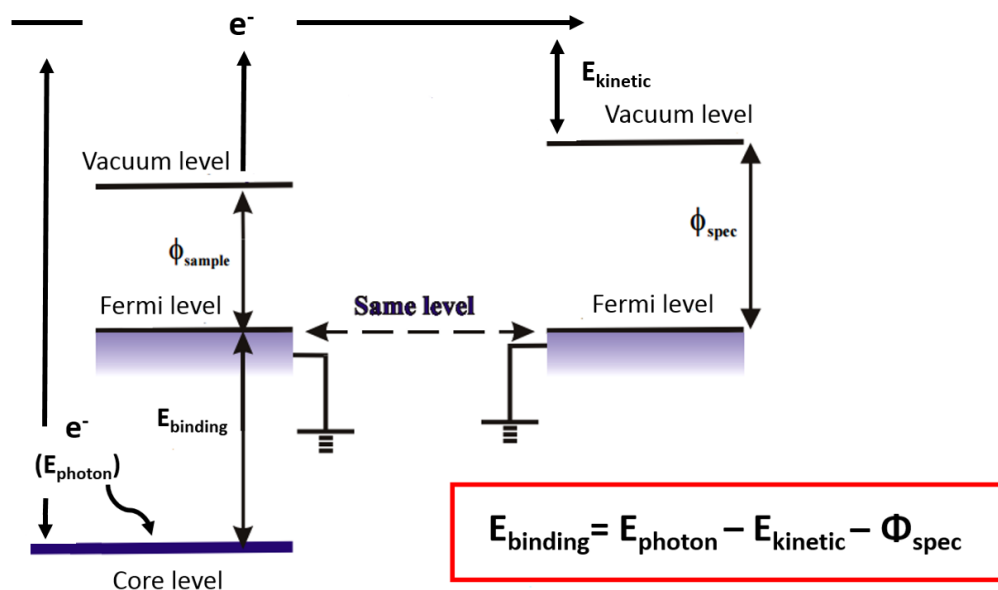
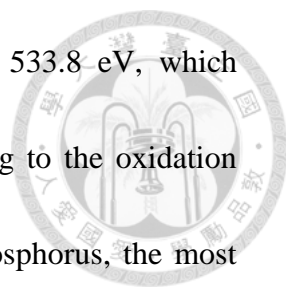


Fig. 3.9 Energy level diagram of the emitted photoelectron.

In order to study whether the ambient atmosphere oxidizes the whole BP crystal or merely the surface, the surface of the black phosphorus was sputtered off by Argon plasma. Figure 3.10 (a) displays three significant peaks P1, P2 and P3, corresponding to $2p_{3/2}$ (130.1eV), $2p_{1/2}$ (130.96eV) and $PxOy$ (134.5eV), respectively [31, 86-89]. After Argon sputtering for 5 min, the intensity of P3 peak decreases to almost zero, suggesting that the oxidation reaction only took place on the surface of the phosphorene and implying an uniform coverage of the oxide.

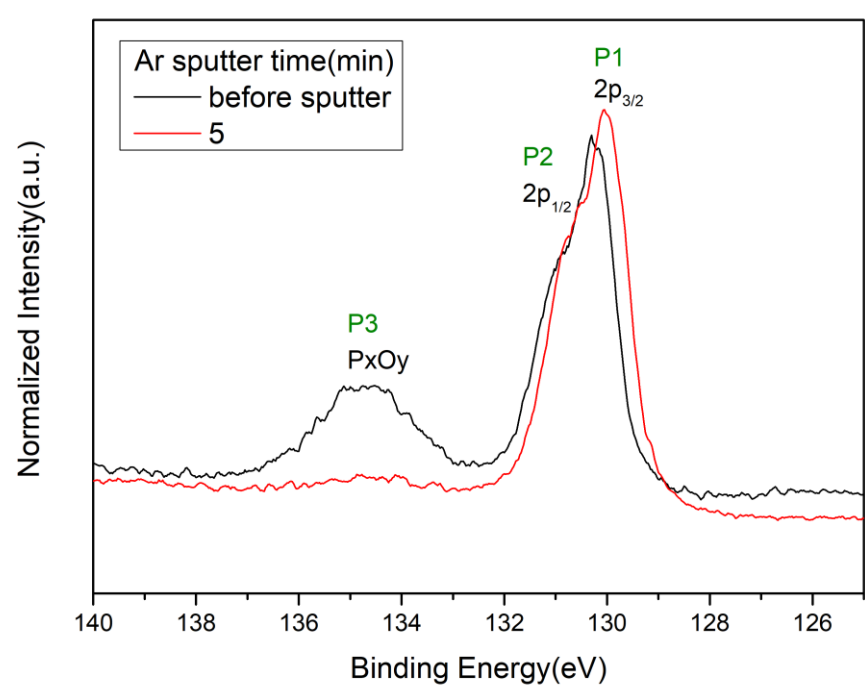
Typically, phosphorus can have the oxidation states of +3 or +5. Because the binding energy of phosphorus having the oxidation states of +3 are lower than 133eV, the higher binding energy at 134.5eV indicated that the phosphorus oxide has the oxidation state of +5. The O 1s core-level spectra before and after argon sputtering is



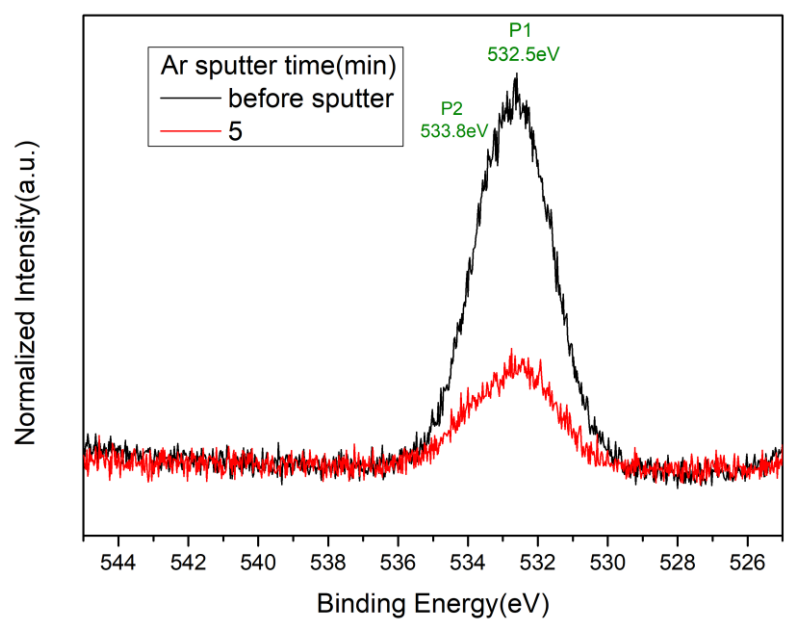
shown in Fig. 3.10 (b). There are two peaks at 532.5 eV and 533.8 eV, which correspond to P=O bond and P-O-P bond, respectively. According to the oxidation state of phosphorus atoms and the bond between oxygen and phosphorus, the most possible form of the phosphorus oxide is P₂O₅ [90, 91], as shown in Fig. 3.10 (c). In fact, P₂O₅ can easily react with water to form orthophosphoric acid (H₃PO₄) or metaphosphoric acid (HPO₃), both of which may pit the oxide and expose the inner part of the black phosphorus crystal to be oxidized, as shown in Fig. 3.10 (d), the “bubbles” on the BP surface is the water absorption by the hydrophilic BP surface. The pristine black phosphorus surface, like other 2D material, is hydrophobic. However, after black phosphorus reacts with oxygen, the surface become hydrophilic and the phosphorene oxide will react with water, forming phosphate which may produce corrosion of the inner part of the black phosphorus crystal [92].



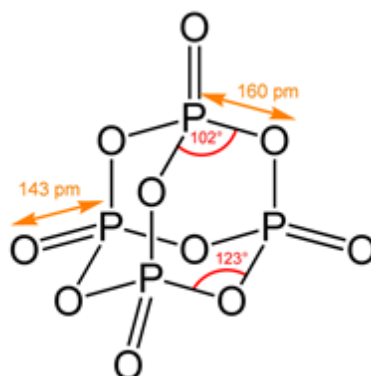
(a)



(b)



(c)



(d)

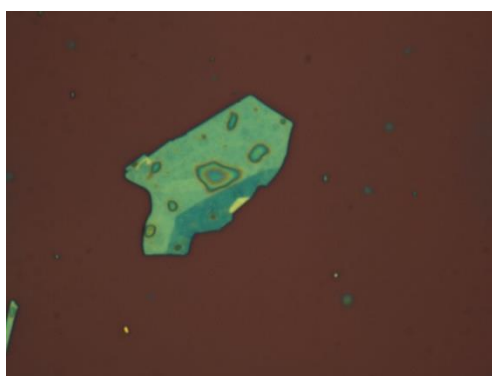
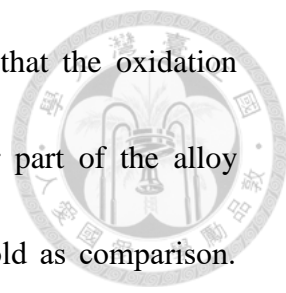


Fig. 3.10 (a) X-ray photoelectron spectrum for BP P2p core level. (b) O 1s core level spectrum. (c) Schematic diagram of P₂O₅ molecule. (d) Optical image of black phosphorus nanosheet after exposing to ambient atmosphere for 24 hours, the “bubbles” implied the water absorption on the hydrophilic surface.

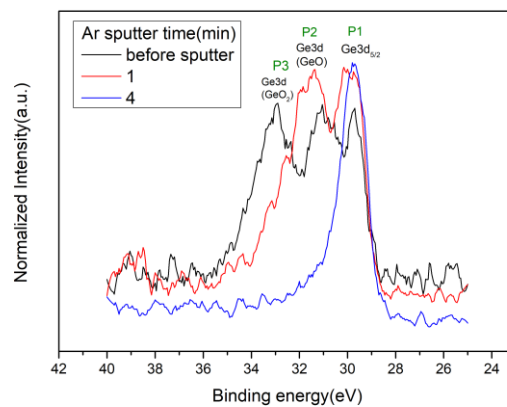
The XPS spectra of Gold-Germanium alloy, which the element ratio of gold to germanium is 88:12 and is the main metal contact used in this research, is also shown in Fig. 3.11 (a) and (b). Fig. 3.11 (a) shows the XPS spectrum of Germanium with three prominent peaks P1, P2 and P3, corresponding to 3d_{5/2} (29.3eV), GeO (30.9eV) and GeO₂ (32.5eV), respectively. Similarly, after Argon sputtering for 1 and 4 min,

the intensity of P2 and P3 peaks gradually decrease, indicating that the oxidation reaction can only affect the surface of the alloy while the inner part of the alloy remains unaffected. Fig. 3.11 (b) shows the XPS spectrum of Gold as comparison.



The two dominant peaks P1 and P2, corresponding to Au4f_{7/2} (84eV) and Au4f_{5/2} (88eV), respectively, are almost unchanged after the argon sputtering process.

(a)



(b)

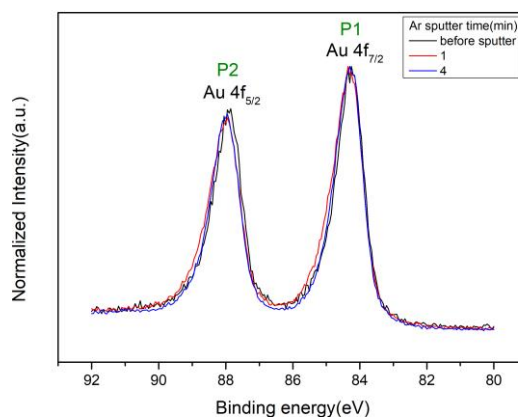
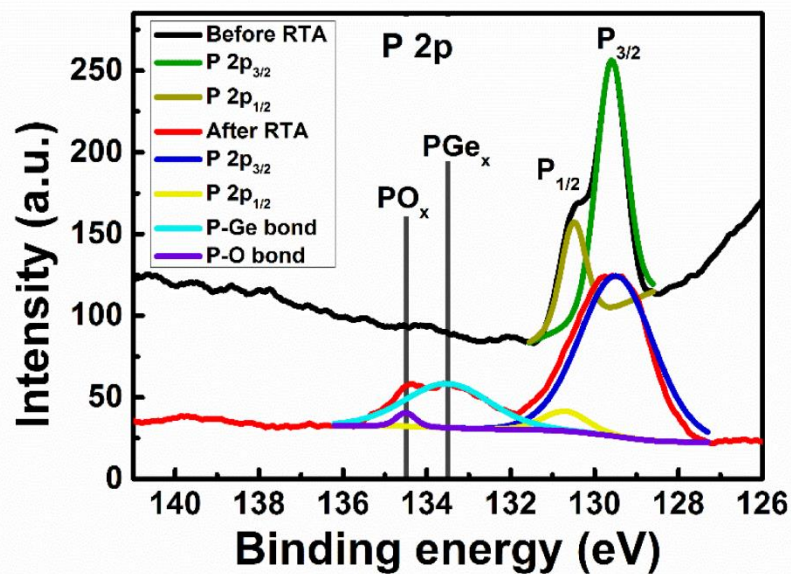


Fig. 3.11 (a) X-ray photoelectron spectrum for Ge3d core level. (b) Au4f core level spectrum.

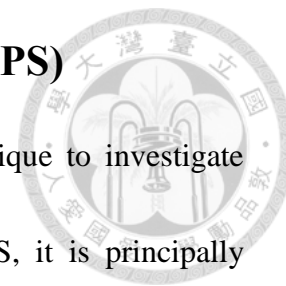
The reaction between BP and Ge after annealing can be examined by XPS. The XPS results of BP with 1.5 nm Ge on top of it before and after RTA are shown in Fig. 3.12. The condition of RTA is: 250 °C for 1 minute in nitrogen environment. In the sample without RTA, the spectrum shows two peaks: P 2p_{3/2} (130.1 eV) and P 2p_{1/2} (130.96 eV). After annealing, two additional peaks located at 133.5 and 134.5 eV emerge. The peak at 134.5 eV is related to phosphorus oxide, while the peak at 133.5 eV is assigned to P-Ge bond. The presence of the P-Ge bond after annealing indicates that germanium can successfully dope into BP and a metallic PGe_x compound can be formed after RTA [93].



Scientific Reports volume 7, Article number: 16857 (2017)

Fig. 3.12 XPS results of BP with 1.5 nm Ge on top of it before and after RTA. After RTA, the peak of P-Ge bond shows up.

3.4.2 Ultraviolet Photoelectron Spectroscopy (UPS)



Ultraviolet photoelectron spectroscopy is an effective technique to investigate the electronic state of a specific material. As compared to XPS, it is principally sensitive to the surface region (to 5 Å depth), which is because of the short free mean path of the emitted photoelectrons in ultraviolet energy range. In order to demonstrate how UPS works, the band diagram of an unknown material is illustrated in Fig. 3.13. When the photons of the ultraviolet light collide with the surface electrons of the material and transfer their energy to the surface electrons, the electrons at valence states which are called secondary electrons (SE) emit. Since the incident photon energy is smaller than 50 eV, it can only excite electrons at valence states while the XPS with its 200~2000 eV photon energy can excite the electrons at core levels. In UPS, an electron excited from valence states to vacuum level follows the equation below.

$$E_{binding} = E_{photon} - (E_{kinetic} + \phi) \quad (3.6)$$

Where $E_{binding}$ is the binding energy of the electron, E_{photon} is the energy of the UV, $E_{kinetic}$ is the kinetic energy of the electron and ϕ is the work function of the material.

The kinetic energy of electrons emitted from valence states can be detected by UPS detector. When electrons come from deeper valence states, the kinetic energy becomes smaller. Thus, the kinetic energy of electrons from deepest valence states can

be defined as zero and this position is called secondary electron edge (SEE). Because the kinetic energy of electrons emitted from the deepest valence states is zero, the work function of a material can be derived through SEE according to Eq. (3.6). On the other hand, electrons emitted from the valence band maximum have the largest kinetic energy. Through UPS analysis, the band diagram of the examined material can be obtained.

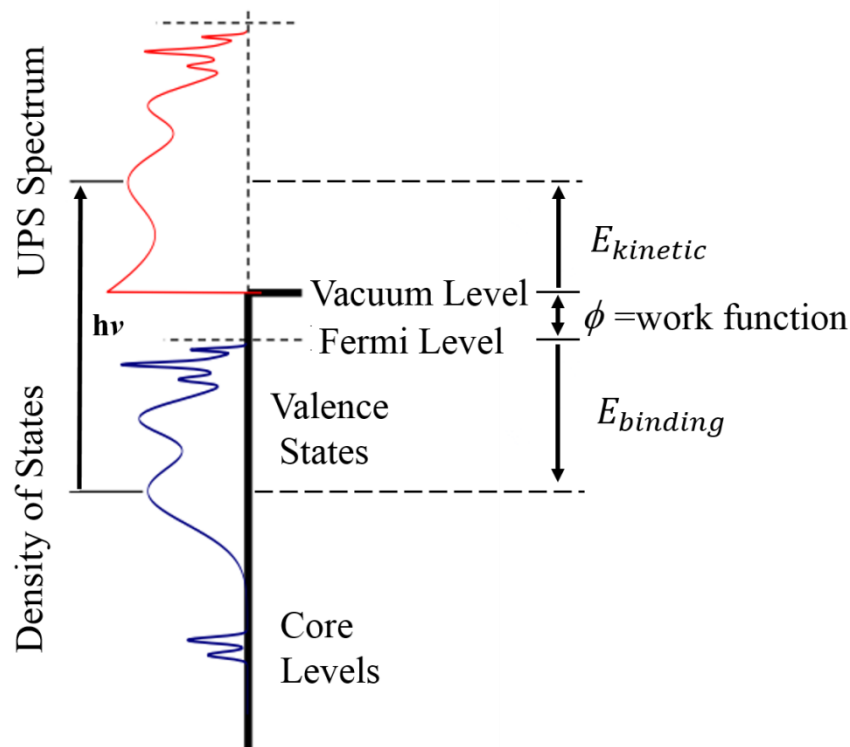
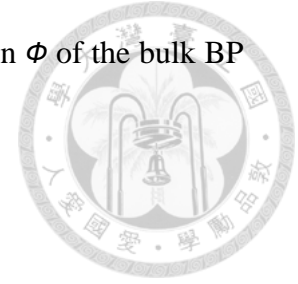


Fig. 3.13 Band diagram of an unknown material.

Fig. 3.14 (a) presents the UPS spectrum of bulk BP and Fig. 3.14 (b) and (c) is the enlarged diagram of (a). By extracting the line of the binding energy of bounded electrons in Fig 3.14 (b), the binding energy which corresponds to the secondary electron edge (SEE) is 16.68 eV. From the SEE at which the kinetic energy of emitted

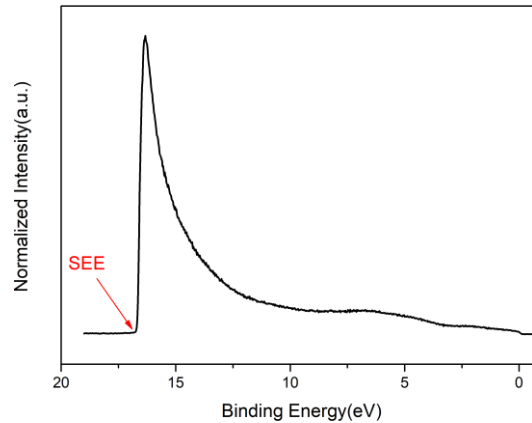
electron is zero and the source energy is 21.22eV, the work function ϕ of the bulk BP can be calculated as:

$$\phi = 21.22 \text{ eV} - 16.68 \text{ eV} = 4.54 \text{ eV}$$

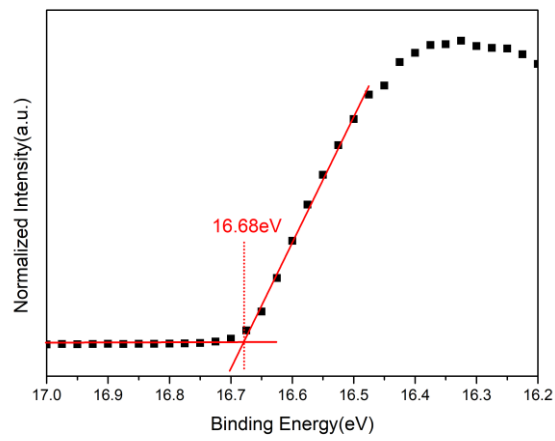


According to Fig 3.14 (c), the energy gap between valence band maximum and Fermi-level is 0.05 eV, which can be acquired from fitting the curves. Since the direct bandgap of bulk BP is 0.33 eV [94, 95] , the Fermi level closer to the valence band confirms that pristine BP is a p-type semiconductor. The band diagram of bulk BP is also shown in Fig. 3.14 (d).

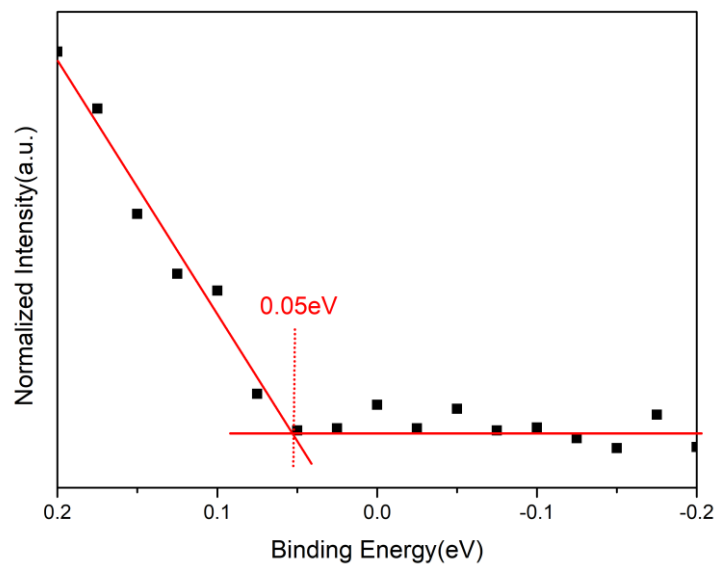
(a)



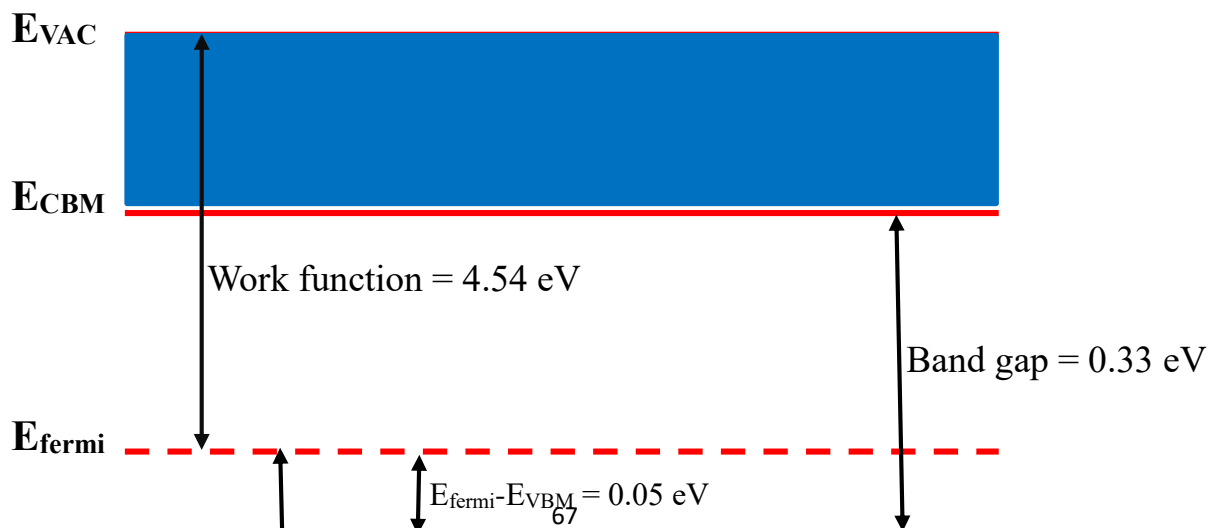
(b)



(c)



(d)



E_{VBM}

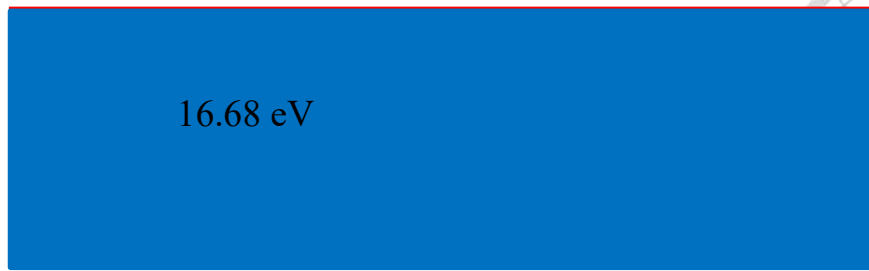


Fig. 3.14 (a), (b) and (c) UPS spectra of bulk BP. (d) Band diagram of bulk black phosphorus.

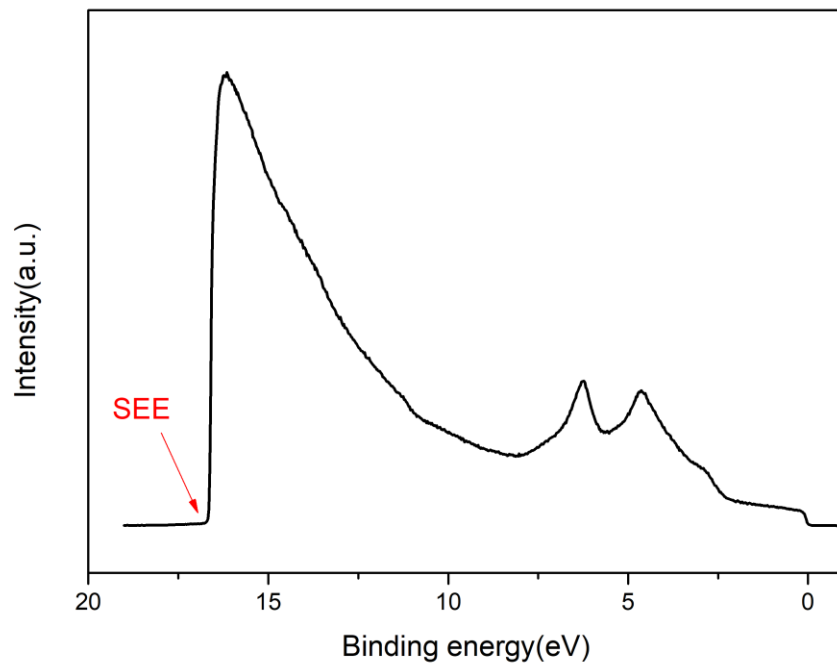
The work function of AuGe alloy can also be obtained by using UPS analysis, as shown in Fig. 3.15 (a) and (b). According to Fig. 3.15 (b), the work function of the alloy can be calculated as:

$$\phi = 21.22 \text{ eV} - 16.65 \text{ eV} = 4.57 \text{ eV}$$

This value is pretty close to the work function of bulk black phosphorus, which is a rather small value when compared to some other high work function metals like Nickel, Palladium...etc. Note that the work function difference is often not the primary issue to determine the quality of the metal/BP contact. Other factors such as fermi level pinning, van der Waals gap at the metal/BP interface and the tunneling current should also be taken into consideration.



(a)



(b)

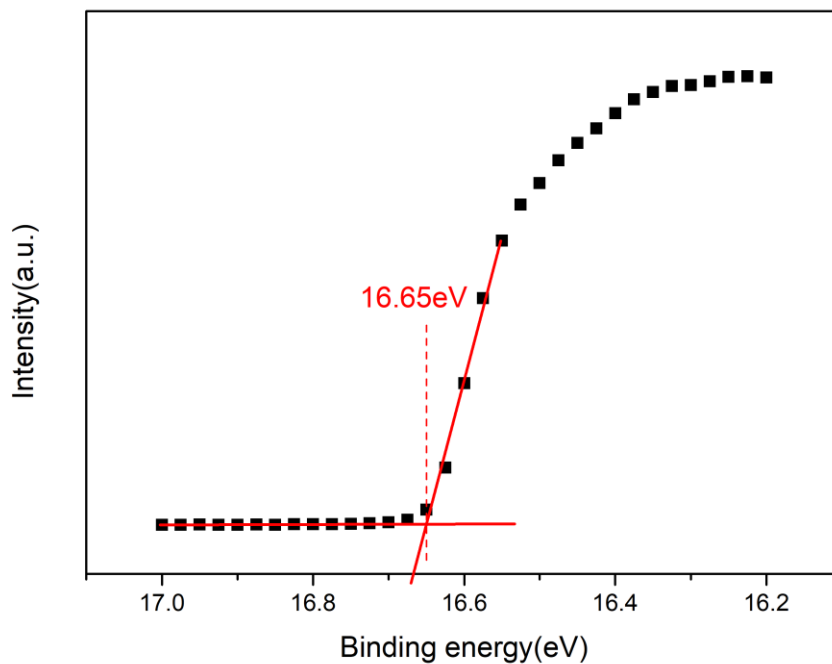


Fig. 3.15 (a) and (b) UPS spectra of AuGe alloy.

Chapter 4 BP Thin Film Transistors

In this chapter, the fabrication processes of the back-gated black phosphorus thin film transistors and their electronic properties will be first demonstrated in Sec. 4.1. The electronic properties of the back-gated BP TFTs can be considerably improved after thermal annealing at 200°C for 1 minute. Sec.4.2 describes the thickness dependent device performance. It can be found that the optimized thickness for the black phosphorus thin film transistor application is around 10 nm. Sec. 4.3 shows the electronic properties of back-gated BP TFTs with different metal contacts. The best metal contact in this research is gold- germanium alloy, due to the fact that germanium can be successfully doped into BP and a metallic PGex compound at the

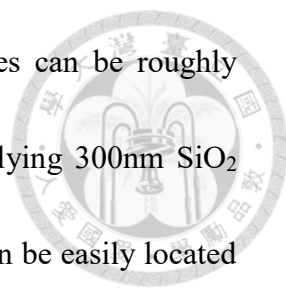
metal-phosphorene interface can be formed after RTA, as mentioned in chapter 3. Sec. 4.4 demonstrates the anisotropic properties of the BP TFTs along armchair and zigzag directions, and thereby the performance-optimized BP TFT can be obtained. Finally, in Sec. 4.5, pn diode is successfully fabricated through the heterojunction of BP-WS₂ and the homojunction of BP with different thickness. The electronic and optical properties of these two structures will also be measured and discussed.

4.1 Back-gated Black Phosphorus TFTs

4.1.1 Device Process Flow

First, the black phosphorus flakes were mechanically exfoliated onto the 300nm SiO₂/p⁺⁺ Si substrate in the glove box to prevent the oxidation of BP. The heavily doped silicon substrate serves as the bottom gate and the 300nm thick SiO₂ serves as the oxide insulator of the device. To remove the organic residues after exfoliation, the substrate was immersed in acetone for 1 hour, and then immersed in isopropyl alcohol (IPA) for 10 minutes. After removing the adhesive residue, the sample was immediately spin-coated with PMMA to avoid the surface of BP being degraded in the atmosphere and then the appropriate flakes were chosen under optical microscope,

as shown in Fig. 4.1(a). The thickness of black phosphorus flakes can be roughly determined through the optical contrast with respect to the underlying 300nm SiO₂ layer. The appropriate flakes with proper thickness and area size can be easily located by the metal mark on the substrate. Next, e-beam lithography was used to pattern the source and drain electrodes, followed by thermal evaporation of Cr (10nm)/Au (70nm) contact and lift off process. To achieve the better electronic properties, thermal annealing at 200°C in the nitrogen environment was used for 1 minute. The effect of thermal annealing will be discussed in Sec. 4.1.2. The cross section view of the device is shown in Fig. 4.1(c). The process flow of the fabrication processes for the black phosphorus TFTs are shown in Fig. 4.2.



(a)

(b)



(c)

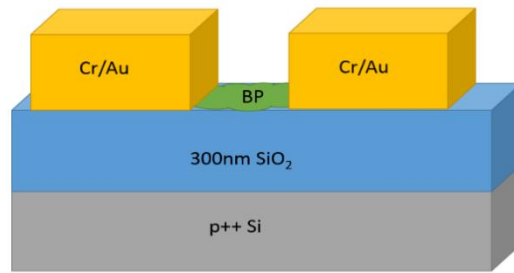


Fig. 4.1 Top view of BP TFT (a) before and (b) after device fabrication under optical microscope. The width and length of the device is 1.8um/2.9um, respectively. (c) Cross-sectional view of back-gated BP TFT structure.

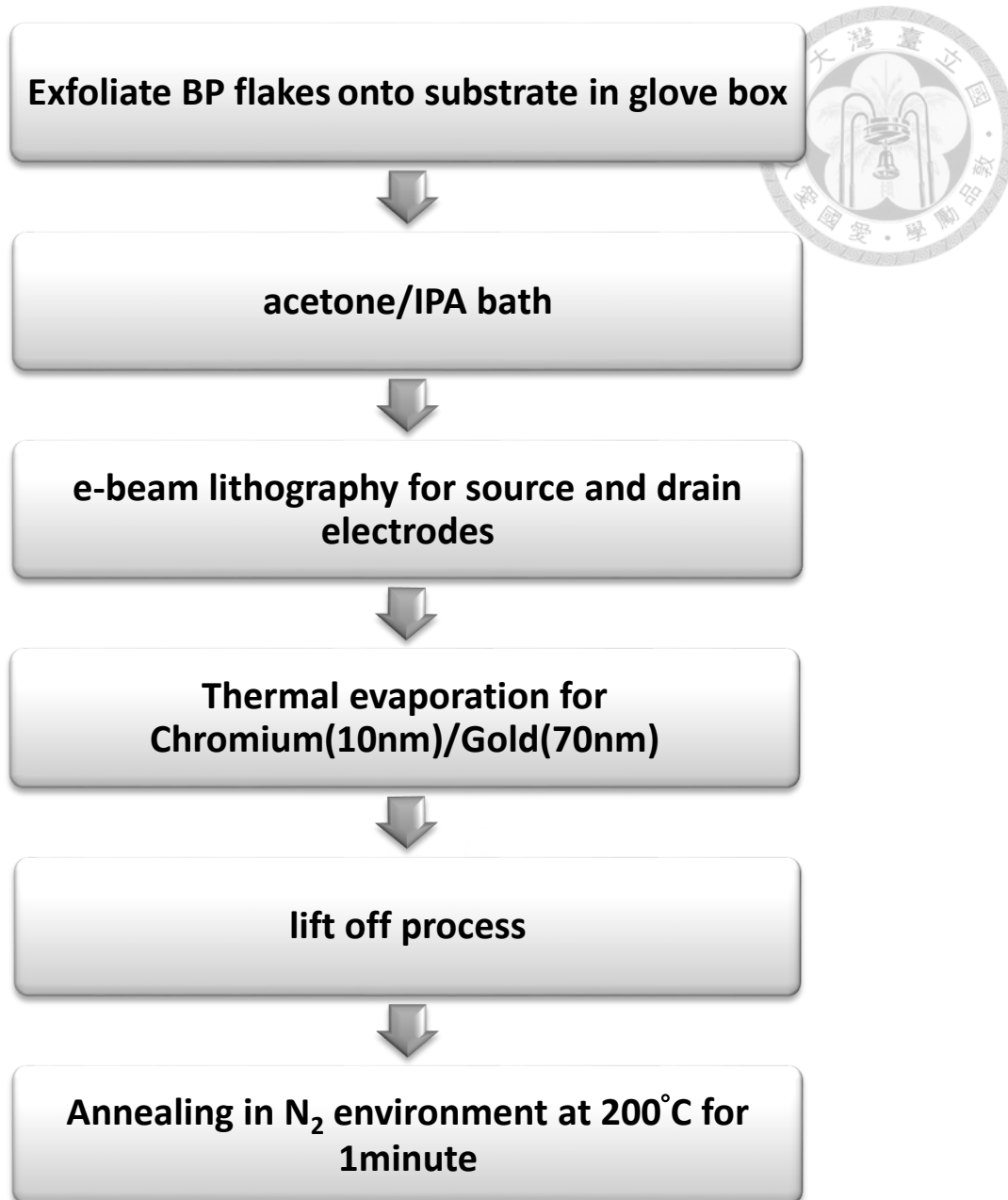


Fig. 4.2 The flow chart of back-gated BP TFT fabrication processes.

4.1.2 Device Performance

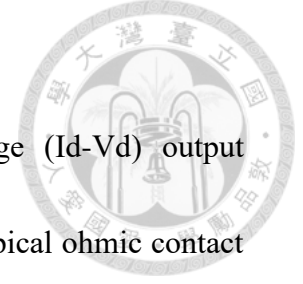
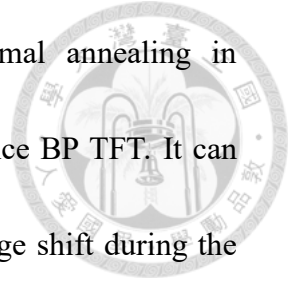


Fig. 4.3 (a) and (b) show the drain current-drain voltage (I_d - V_d) output characteristics before and after thermal annealing. In Fig. 4.3, a typical ohmic contact behavior of BP TFT is observed. As the gate voltage (V_g) becomes more negative, the drain current I_d becomes larger, which confirms that BP is a hole-dominant semiconductor. The transfer drain current versus gate voltage (I_d - V_g) characteristics of the BP TFT before and after thermal annealing is shown in Fig. 4.4 (a) and (b). The gate voltage sweep direction is shown in the arrows in Fig. 4.4. From Fig. 4.4, the on/off current ratio of this BP TFT before thermal annealing is 2×10^2 . After thermal annealing, the on/off current ratio is increased to 1.3×10^3 . This property is comparable to most graphene FETs due to its zero band gap. The subthreshold swing before and after thermal annealing are 17 V/dec and 5.2V/dec, respectively. The field effect mobility is also increased from 28 $\text{cm}^2/\text{V}\cdot\text{sec}$ to 86 $\text{cm}^2/\text{V}\cdot\text{sec}$, which can be extracted from the transconductance of linear region in the transfer characteristics curve by using Eq. (4.1).

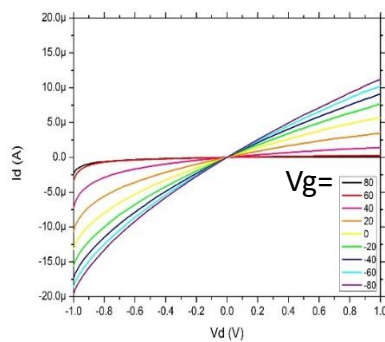
$$\mu_{EF} = \frac{g_m}{C_i \frac{W}{L} V_d} \quad (4.1)$$

Where μ_{EF} is the field effect mobility of the TFT, g_m is the transconductance, $W(L)$ is the channel width (length), and C_i is the gate oxide capacitance per unit area.

These electronic performance enhancement indicates that thermal annealing in nitrogen condition is a necessary process to obtain high performance BP TFT. It can also be observed that the hysteresis, defined as the threshold voltage shift during the forward sweep and reverse sweep, of this device is pretty large, which is due to the positive interface charges between BP/SiO₂ interface and is not desirable for logic switching applications because it will increase the on/off switching voltage, thereby increasing the power consumption of the circuit. Since the measurement of this device was conducted in atmosphere, if the measurement is conducted in vacuum, the hysteresis can be significantly reduced due to the reduction of interface charges. Table 4.1 summarizes the performance of BP TFT using SiO₂ substrate and Chromium contact.



(a)



(b)

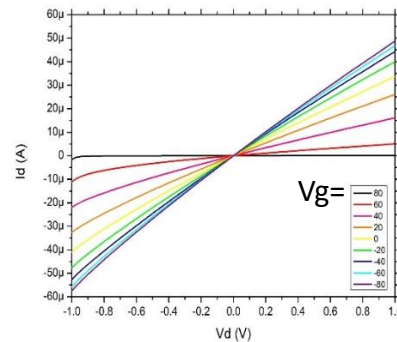


Fig. 4.3 Output characteristics of Cr contact BP TFT (a) before and (b) after thermal annealing.

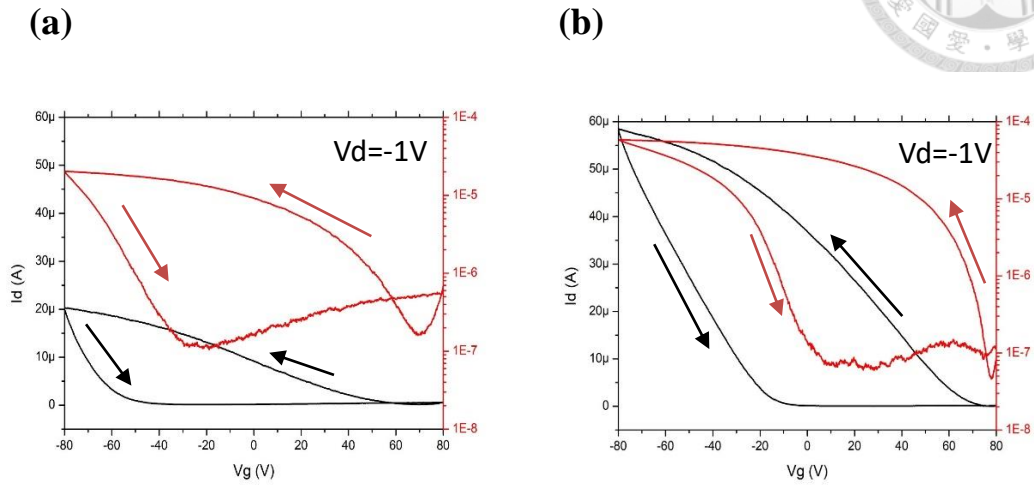


Fig. 4.4 Transfer characteristics of Cr contact BP TFT (a) before and (b) after thermal annealing.

Table 4.1 Electronic properties of BP TFTs before and after thermal annealing.

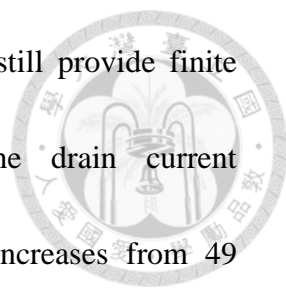
Annealing	Hole Mobility($\text{cm}^2/\text{V}\cdot\text{s}$)	On/Off	Subthreshold Swing(V/dec)
Before	28	2×10^2	17
After	86	1.3×10^3	5.2



4.2 Thickness Dependence of Electronic Properties

Because of the thickness-dependent band structure, the thickness of BP plays an important role on its electronic properties. The flakes with different thickness of 57nm, 43nm, 16.3nm, 11nm and 5nm on a same substrate were chosen. Thickness of the flakes were determined by AFM. It's worthy mentioning that the thickness is not constant across the surface, so an average estimated thickness was used. The metal contact used in this section is AuGe alloy (Au:Ge = 88:12), and the measurement is conducted in vacuum (pressure < 200mTorr).

The transfer drain current versus gate voltage characteristics of the BP TFTs in log scale is shown in Fig. 4.5. All the flakes demonstrate an ambipolar transport behavior. Since the electron mobility which are less than $10 \text{ cm}^2/\text{V}\cdot\text{s}$ are too low for the device application, Table. 4.3 only lists the dominant electronic properties of holes for easy comparison. The current on/off ratio (subthreshold swing) will monotonously increase (decrease) from 6.4×10^1 to 1.4×10^5 (10.65 V/dec to 4.63 V/dec) as the thickness decreases from 57 nm to 4 nm. This phenomenon has been reported in other two-dimensional FETs such as few-layer graphene and MoS₂ [96, 97] and can be attributed to the screening of the gate electric field. Simply speaking, the gate electric field only induces free carriers in the bottom layers as a result of charge screening.



Therefore, as the thickness of BP increases, the top layers can still provide finite conduction in the off state, thereby reducing/enlarging the drain current modulation/subthreshold swing. The field effect mobility also increases from 49 $\text{cm}^2/\text{V}\cdot\text{sec}$ to 173 $\text{cm}^2/\text{V}\cdot\text{sec}$ as the thickness decreases from 57 nm to 11 nm, which is because of the fact that the current is injected from electrical contacts on the top surface, and the finite interlayer resistance forces the current to flow through the top layers, which are not gated by the back gate, as shown in Fig. 4.6, thereby depresses the mobility for samples thicker than ~ 10 nm. However, the mobility drastically decreases to only 5 in the 4 nm thick sample, which is due to the fact that thinner samples are more vulnerable to charge impurities at the interface that are otherwise screened by the induced charge in thicker samples. To conclude, since the mobility is affected by the interlayer resistance and the impurity charge scattering at the interface, optimized thickness of BP thin film around 10 nm should be chosen to acquire better device performance.

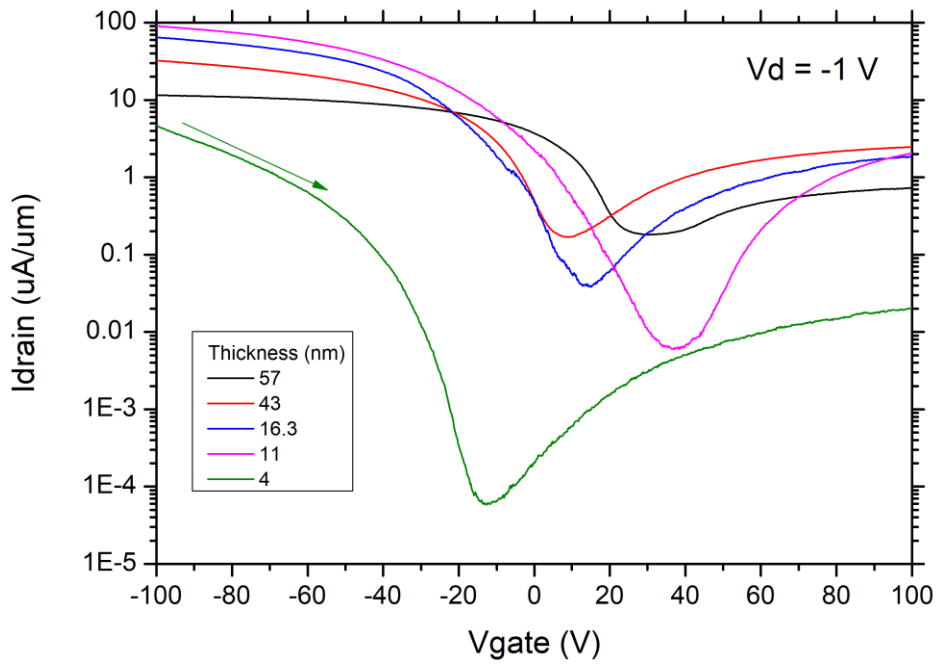
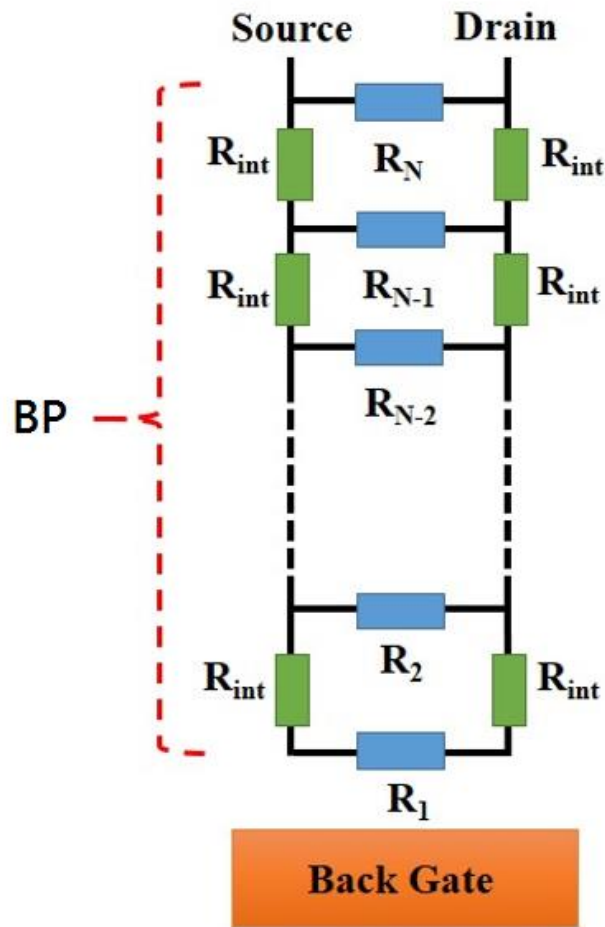


Fig. 4.5 Transfer characteristics of BP TFT in log scale with different thicknesses, the green arrow indicates the sweep direction of the gate bias.

Table 4.2 Electronic properties of BP TFTs for different thicknesses.

Thickness (nm)	Hole Mobility($\text{cm}^2/\text{V}\cdot\text{s}$)	On/Off	Subthreshold Swing(V/dec)
57	49	6.4×10^1	10.65
43	116	1.9×10^2	9.32
16.3	165	2×10^3	8.64
11	173	3.3×10^4	8
4	5	1.4×10^5	4.63

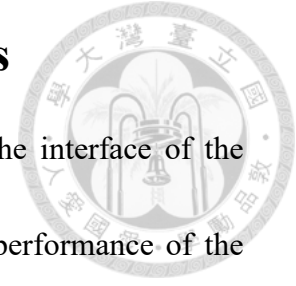


Nano letter, 2013, 13, 104

Purdue University

Fig. 4.6 The model of back-gated BP TFT

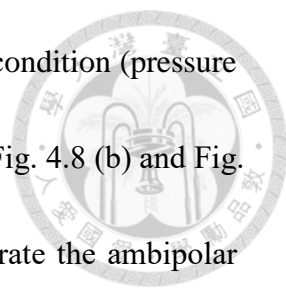
4.3 Contact Metal Comparison of BP TFTs



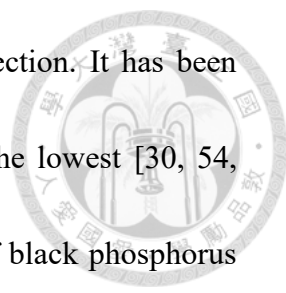
As mentioned in chapter 1, the large contact resistance at the interface of the source/drain metal and BP channel will undesirably restrain the performance of the BP TFT. In order to extract the contact resistance, transmission line method (TLM) was used to obtain the contact resistance for different contact metals [98]. The measured total resistance consists of several components, as shown in Eq (4.2).

$$R_T = 2R_m + 2R_C + R_{channel} \quad (4.2)$$

where R_m is the resistance of the contact metal, R_C is associated with the metal/semiconductor interface, and $R_{channel}$ is the semiconductor resistance. The resistance of a single contact would be $R_m + R_C$. However, in most situations, the resistivity of the metal in the contact is low enough to be ignored. These results suggest a method for measuring the contact resistance. If resistors of several different lengths are constructed, keeping all other conditions the same, the total resistances of each can be measured and plotted. In the limit of a zero-length resistor, the residual resistance would be just twice the contact resistance, which can be found from the graph by extrapolating back to $L = 0$. There are three different contact metals used in this research, which are Cr, Ni and AuGe alloy (Au:Ge = 88:12) . Fig. 4.7, Fig. 4.8 and Fig. 4.9 shows the device size and performance for the Cr, Ni and AuGe alloy contacted BP TFT, respectively. The electrical properties of these three devices are

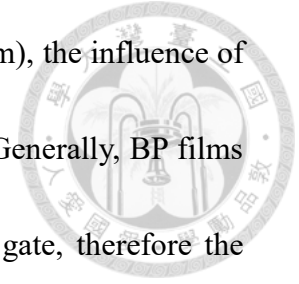


listed in Table 4.3. All of the three devices is measured in vacuum condition (pressure < 200mTorr). According to the transfer I_d - V_g plots in Fig. 4.7 (b), Fig. 4.8 (b) and Fig. 4.9 (b), it can be observed that all of these three devices demonstrate the ambipolar behavior, and the hysteresis are all much smaller than those of the Cr contact device mentioned in Sec. 4.1, implying that the electrical performance of BP TFT will be severely influenced by atmosphere. In fact, for hole current output characteristics in Fig. 4.7 (c), Fig. 4.8 (c) and Fig. 4.9 (c), all three devices show excellent ohmic contact behavior, which might due to the small bandgap ($=0.33$ eV) of black phosphorus and thus forming a low schottky barrier height at the metal/BP interface. The hole mobility for Cr, Ni and AuGe alloy contacted devices are 175 $\text{cm}^2/\text{V}\cdot\text{sec}$, 52 $\text{cm}^2/\text{V}\cdot\text{sec}$ and 116 $\text{cm}^2/\text{V}\cdot\text{sec}$, respectively. Since Nickel has the highest work function ($=5.15$ eV) out of these three, the lowest hole mobility for Ni contacted device might imply that the main mechanism of the current transport at the contact is through tunneling [99, 100] . The lower mobility of the AuGe alloy contacted device might due to two reasons. First, the thickness of the AuGe alloy contacted device ($=43$ nm) is quite large. As mentioned in Sec. 4.2, thicker samples tend to have lower mobility because of the existence of interlayer resistance in BP. The rather low on/off current ratio and the yellow color of this device under optical microscope also indicate that it is thicker than the other two devices. Second, the current transport



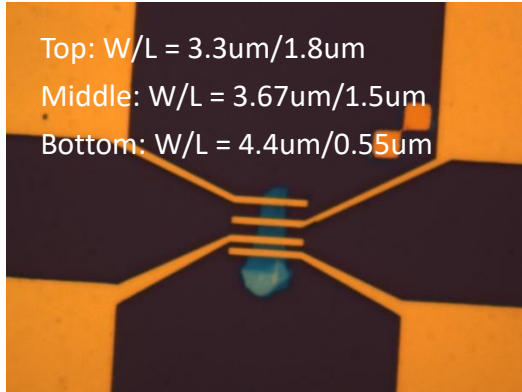
direction of the AuGe alloy contacted device is along zigzag direction. It has been reported that the hole mobility for BP along zigzag direction is the lowest [30, 54, 101] , comparing to other directions. The anisotropic properties of black phosphorus will be further investigated in Sec. 4.4. Finally, the contact resistance for these three metal contacts is obtained from the transmission line method (TLM). Fig. 4.10 demonstrates the relationship between the contact resistance versus back gate voltage. Table 4.4 lists the values of these contact resistances. As previously discussed, Ni undoubtedly has the highest contact resistance (from 5.61 Ω *mm to 8.03 Ω *mm as the back gate bias sweeps from -100 V to -50 V), while Cr contact resistance increases from 2.06 Ω *mm to 3.54 Ω *mm as the back gate bias sweeps from -100 V to -50 V. The dependencies of the contact resistance versus back gate bias for these two metals are quite consistent with the previous studies [35, 46, 59, 102, 103] . Although AuGe alloy has the lowest contact resistance out of these three, probably due to the fact that germanium can successfully dope into phosphorene and thus cause a p-type doping effect [93], its contact resistance actually decreases from 1.76 Ω *mm to 1.21 Ω *mm as the back gate bias sweeps from -100 V to -50 V. This phenomenon can possibly due to the large thickness of the AuGe alloy contacted device. According to the model shown in Fig. 4.6. As the back gate voltage sweeps to a large negative bias, the conduction channel will be closer to the BP/insulator interface, and the screening

effect becomes worse. Therefore, if the BP film is too thick ($> 40\text{nm}$), the influence of interlayer resistance might slightly enlarge the contact resistance. Generally, BP films with thickness less than 20 nm can be better gated by the back gate, therefore the impact of interlayer resistance can be negligible.

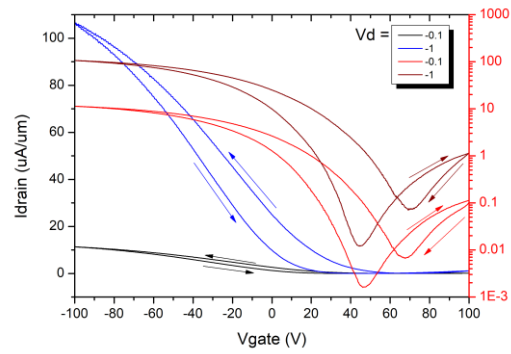




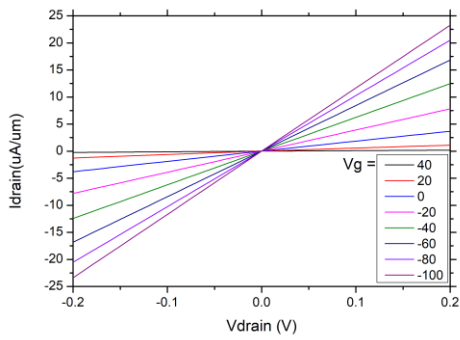
(a)



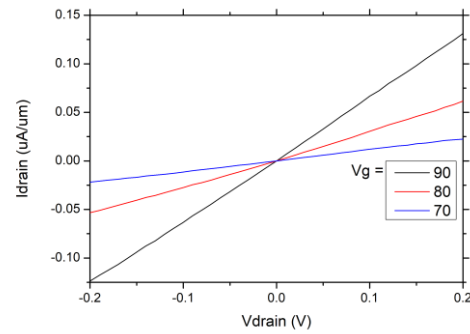
(b)



(c)



(d)



(e)

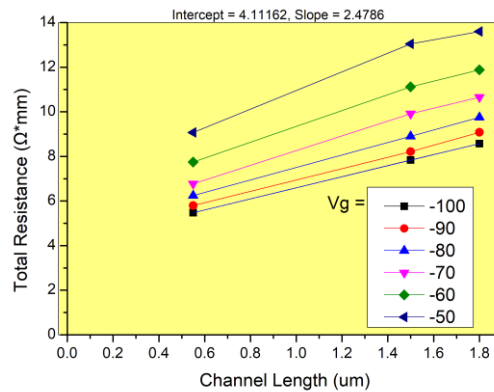


Fig. 4.7 (a) Optical image of the Cr contact TLM sample (b) Transfer characteristics of the Cr contact device, $L = 1.8 \mu\text{m}$. (c) Output characteristics of

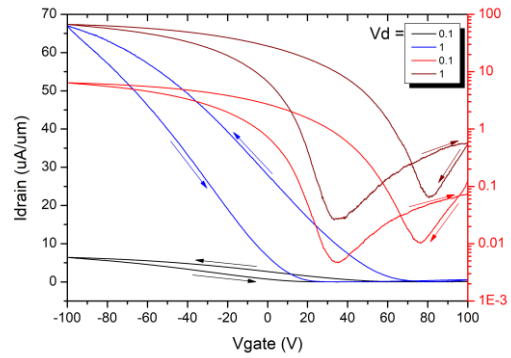
the Cr contact device for hole current transport and (d) electron current transport. (e) Result of TLM extraction method.



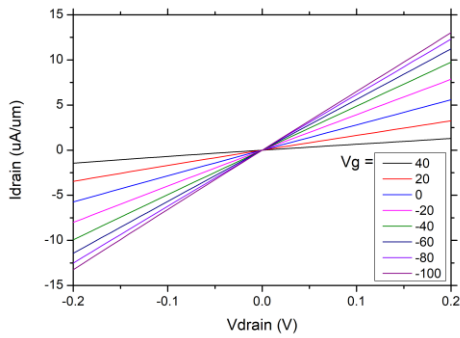
(a)



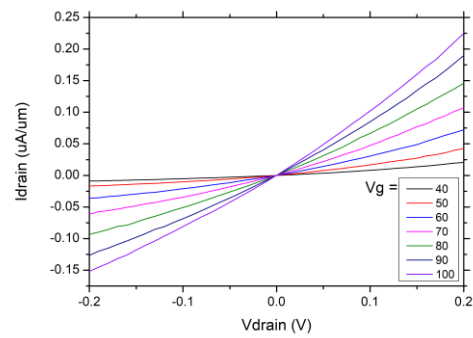
(b)



(c)



(d)



(e)

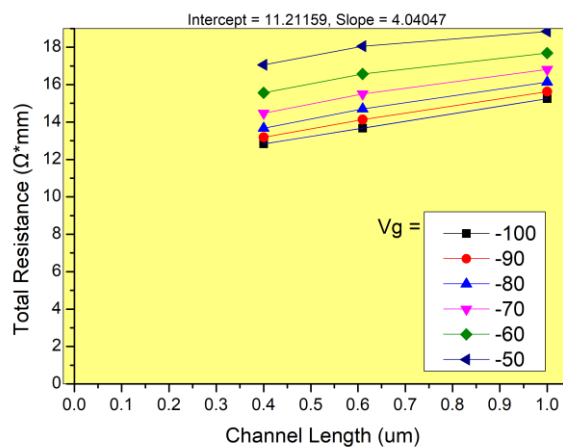


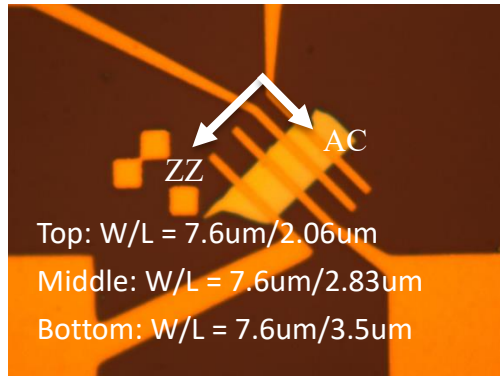
Fig. 4.8 (a) Optical image of the Ni contact TLM sample (b) Transfer characteristics of the Ni contact device, $L = 1 \mu\text{m}$. (c) Output characteristics of the

Ni contact device for hole current transport and (d) electron current transport. (e)

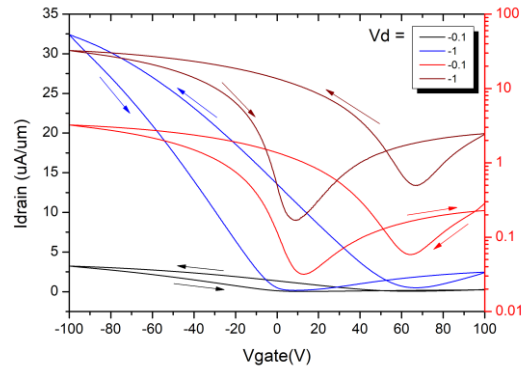
Result of TLM extraction method.



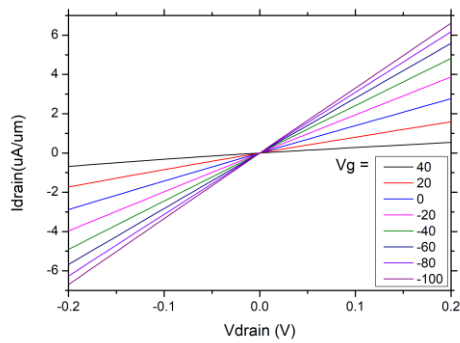
(a)



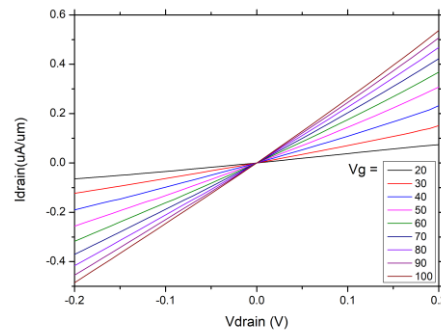
(b)



(c)



(d)



(e)

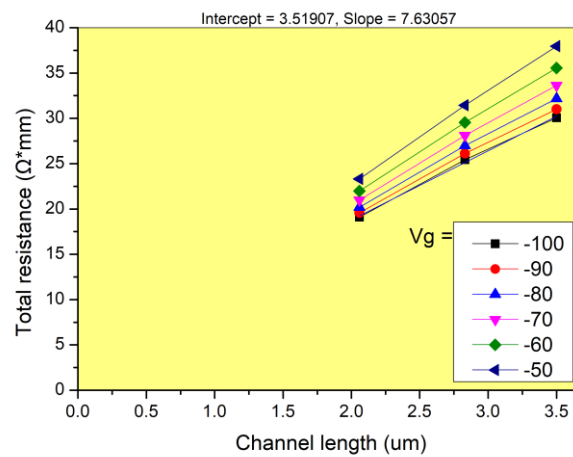


Fig. 4.9 (a) Optical image of the AuGe alloy contact TLM sample (b) Transfer characteristics of the AuGe alloy contact device, $L = 3.5 \mu\text{m}$. (c) Output

characteristics of the AuGe alloy contact device for hole current transport and (d)

electron current transport. (e) Result of TLM extraction method.

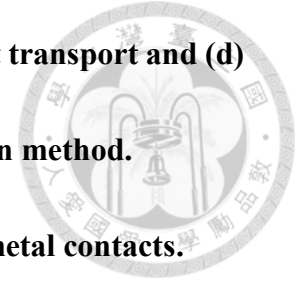


Table 4.3 Electronic properties of BP TFTs with different metal contacts.

Contact	Carrier	Mobility(cm ² /V*s)	On/Off	Subthreshold Swing(V/dec)
Cr	Hole	175	9×10^3	8
	Electron	5.5	9.5×10^1	13.92
Ni	Hole	52	2.6×10^3	8.33
	Electron	1.2	3×10^1	17.4
AuGe alloy	Hole	116	1.9×10^2	9.32
	Electron	12	1.5×10^1	30.98

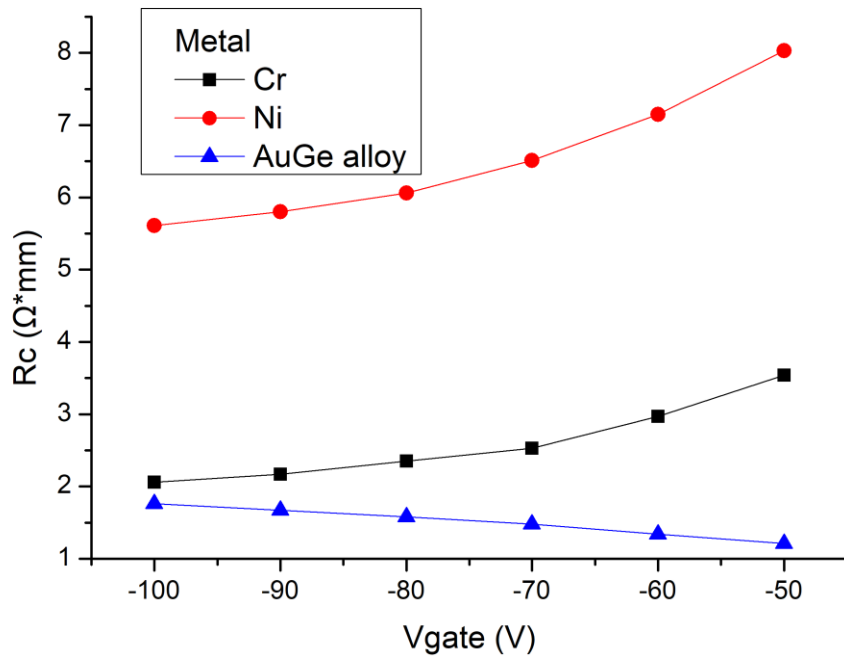


Fig. 4.10 Three different metal's contact resistance versus back gate bias. Note

that the dependency of the contact resistance versus back gate bias for AuGe alloy

contact is quite different than the other two metals.



Table 4.4 Three different metal's contact resistance versus back gate

bias.

Back gate bias(V)	-100	-90	-80	-70	-60	-50
R_C for Cr(Ω*mm)	2.06	2.17	2.35	2.53	2.97	3.54
R_C for Ni(Ω*mm)	5.61	5.8	6.06	6.51	7.15	8.03
R_C for AuGe alloy(Ω*mm)	1.76	1.67	1.58	1.48	1.34	1.21



4.4 Anisotropic Properties of Black Phosphorus

As mentioned before, BP thin films with rectangular shape can be fabricated by using the technique introduced in chapter 2. The crystal orientation of the rectangular BP film can be immediately verified by optical microscope, as the long and short sides of the rectangular BP corresponds to ZZ and AC directions, respectively. Thus, the current transport direction can be determined without complicate and tedious techniques to determine the lattice orientation of BP like Raman measurement, and the fabrication time can be reduced to prevent BP from severe oxidation. Besides, the calculation of the field-effect mobility will be more precise since it can be extracted by the transconductance and the geometric factor L/W of the thin film when the device operates in linear region. However, the L/W for an irregularly shaped BP film is so indefinite that it inevitably leads to a finite error in the calculation of mobility. Thanks to the geometric certainty of rectangular BP, a more accurate mobility can be acquired.

To investigate the anisotropic properties of the rectangular BP, two rectangular BP flakes were mechanically exfoliated onto the Si/SiO₂ substrate, and they were fabricated along ZZ and AC direction, respectively. The contact metal is AuGe alloy. Fig. 4.11 and Fig. 4.12 display the device performance along these two directions, and

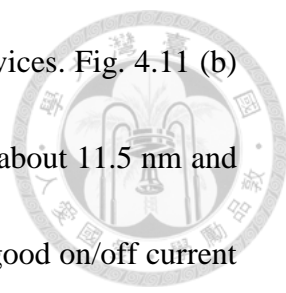
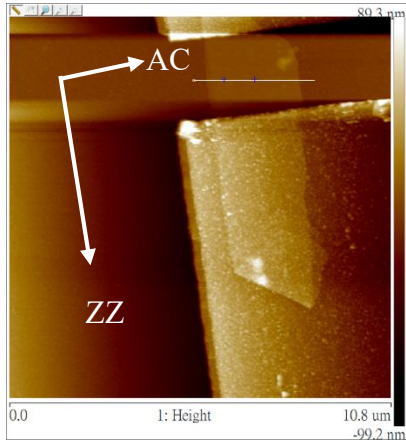


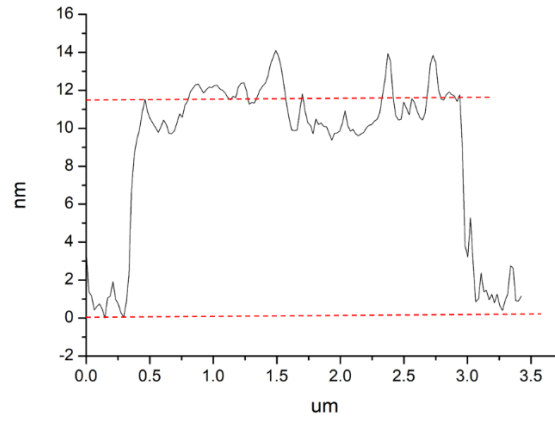
Table 4.5 lists some important electrical properties of these two devices. Fig. 4.11 (b) and Fig. 4.12 (b) show the thickness of these two devices which is about 11.5 nm and 20 nm, respectively, suggesting that both devices can demonstrate good on/off current ratio ($ZZ = 1 \times 10^4$ and $AC = 2.3 \times 10^3$), as shown in Fig. 4.11 (e) and Fig. 4.12 (e). Output characteristics show that AuGe alloy forms a good ohmic contact with BP. Notice that the peak hole mobility along AC direction can be up to $298 \text{ cm}^2/\text{V}\cdot\text{sec}$, which is comparable to other studies [93, 100, 104, 105]. In addition, the hole (electron) mobility ratio of AC/ZZ is about 1.88 (2.78), which is consistent with some previous researches [28, 30]. In conclusion, the using of contact and direction engineering can contribute to a high hole mobility for BP, revealing the potential of BP in the application of field-effect transistors.



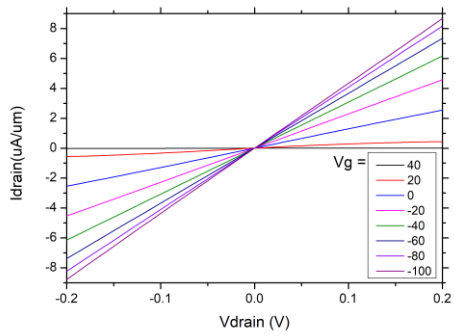
(a)



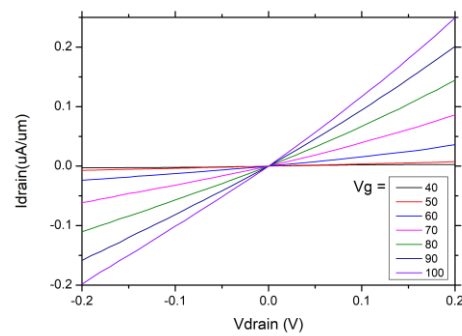
(b)



(c)



(d)



(e)

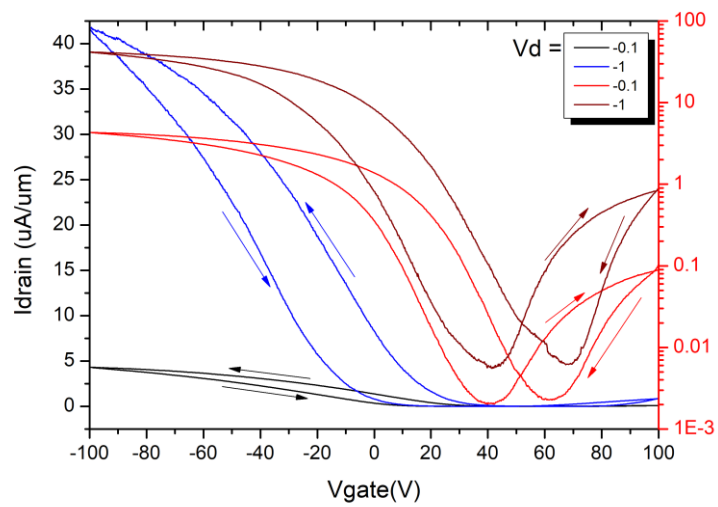


Fig. 4.11 (a) AFM image of the ZZ direction sample, $W/L = 2.55\mu\text{m}/2.8\mu\text{m}$. (b)

Thickness = 11.5 nm. Output characteristics for (c) hole and (d) electron transport.



(e) Transfer characteristics.

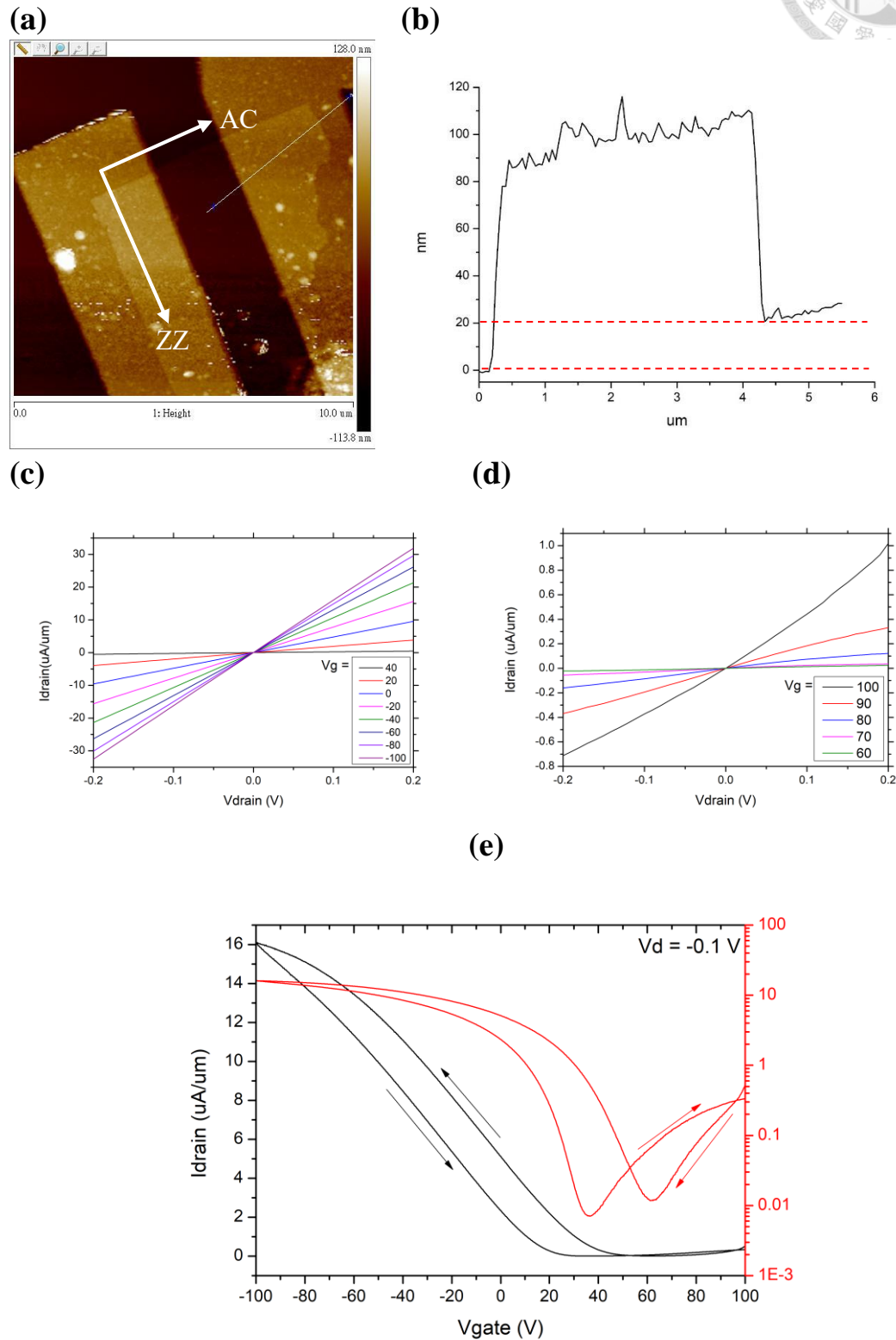


Fig. 4.12 (a) AFM image of the AC direction sample, $W/L = 6.4\mu\text{m}/2.2\mu\text{m}$. (b)

Thickness = 20 nm. Output characteristics for (c) hole and (d) electron transport

(e) Transfer characteristics.



Table 4.5 Electrical properties of BP TFTs along two transport directions.

Orientation	Carrier	Mobility($\text{cm}^2/\text{V}\cdot\text{s}$)	On/Off	Subthreshold Swing(V/dec)
ZigZag	Hole	159	1×10^4	13.13
	Electron	5.4	1.7×10^2	8.79
ArmChair	Hole	298	2.3×10^3	7.69
	Electron	15	7.6×10^1	17.16

To further explore the anisotropic properties of BP, two BP TFTs along two different directions were fabricated on the same BP flake, as shown in Fig 4.13. The thickness of this BP film is about 35 nm. The transfer characteristics of these two BP TFTs along AC and ZZ directions are shown in Fig. 4.13 (c) and (d), respectively. Table 4.6 shows the electrical properties of these two devices. Note that the hole mobility ratio between AC and ZZ is reduced to only about 1.52 in this case, which is lower than the theoretical results. The reason is that when there are two pairs of source/drain electrodes corresponding to AC and ZZ directions on the same BP flake, the drain current cannot be completely parallel to the AC (ZZ) orientation owing to the current spreading effect, which will result in underestimation (overestimation) the

mobility along AC (ZZ) direction. Fig. 4.14 illustrates the current spreading effect when measuring the mobility ratio μ_{AC}/μ_{ZZ} .

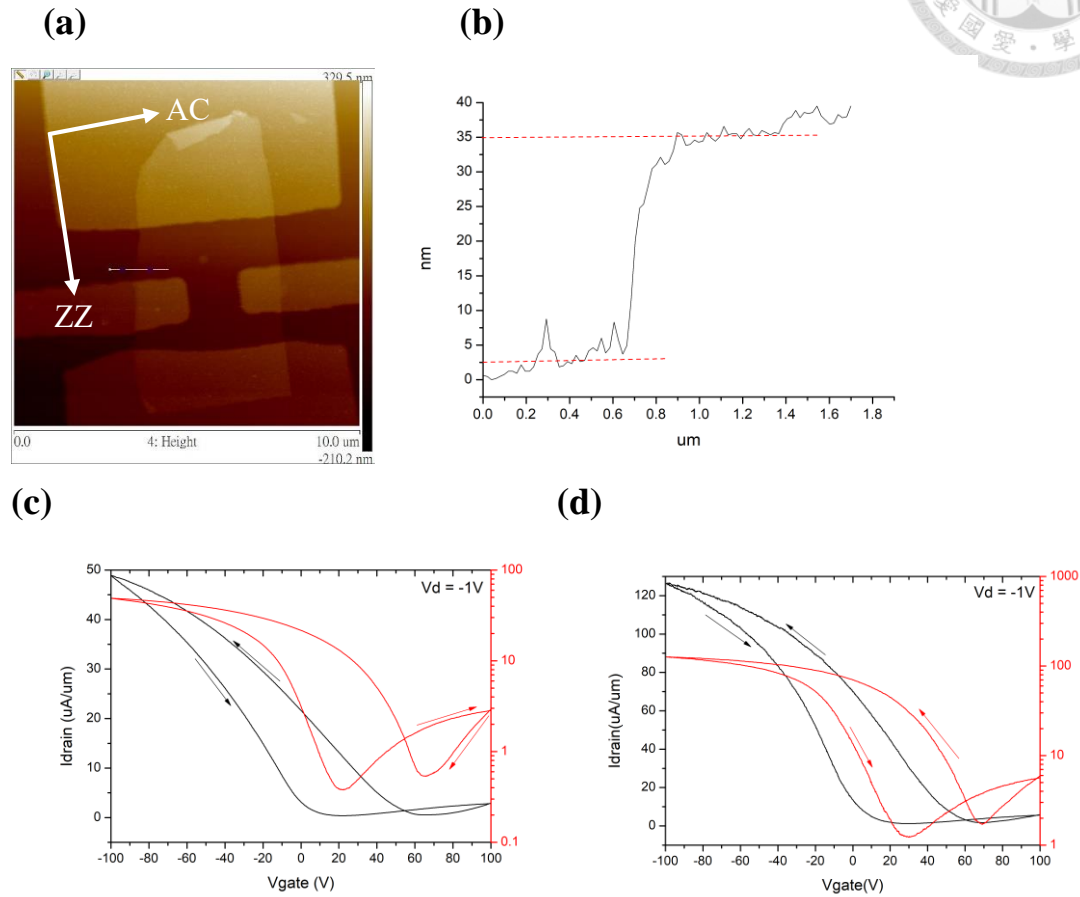
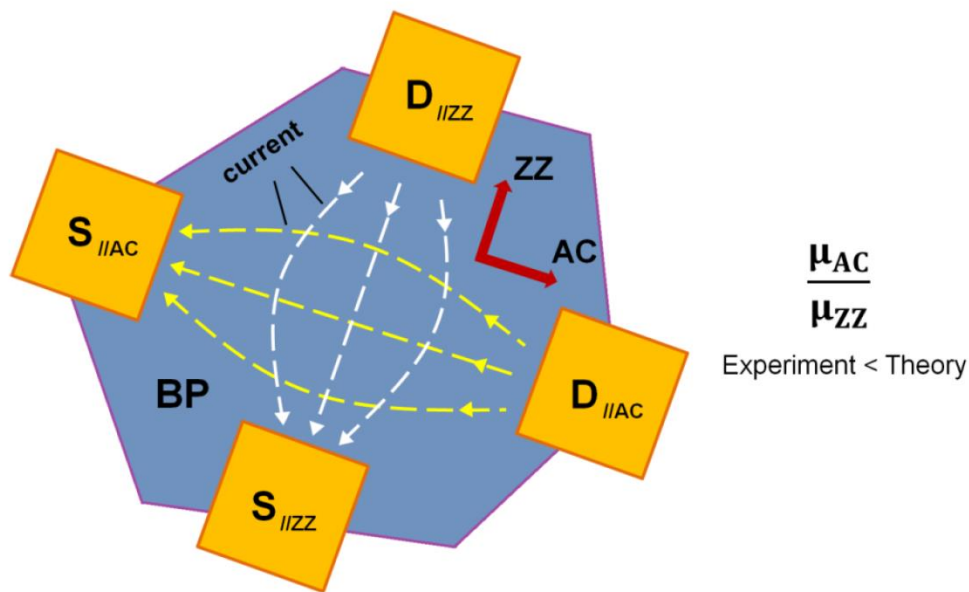


Fig. 4.13 (a) AFM image of the BP TFT sample, W/L = 4.35um/3.5um for ZZ, and 1um/1.7um for AC, respectively. (b) Thickness = 35 nm. Transfer characteristics for (c) ZZ direction and (d) AC direction.

Table 4.6 Electrical properties of BP TFTs along two transport directions on the same flake.

Orientation	Carrier	Mobility($cm^2/V*s$)	On/Off	Subthreshold Swing(V/dec)
ZigZag	Hole	140	2×10^2	13.31

	Electron	12	1×10^1	20.96
ArmChair	Hole	213	1.5×10^2	14.21
	Electron	15	8×10^0	34.35



Yao Hsiao, Master Thesis, Black phosphorus with unique rectangular shape and its anisotropy for electronics and optoelectronics (2018).

Fig. 4.14 Illustration of the current spreading effect in BP TFT.

In fact, the mobility is not a fixed value because of the various scattering mechanisms, such as surface roughness scattering, phonon scattering and Coulomb scattering. Among these scattering mechanisms, the surface roughness scattering is the dominant mechanism in nano-scaled 2D materials. Therefore, the mobility in 2D materials is not a constant but a function of back gate voltage. Fig 4.15 shows the hole mobility and the mobility ratio between AC/ZZ versus back gate bias according to the samples in Fig. 4.11 and Fig. 4.12. Note that both the mobilities along AC and ZZ

seems to gradually decline as the back gate bias sweeps from 0V to -100V. The μ_{AC}/μ_{ZZ} ratio is found to be in the interval of 1.8 to 2.8. The big ratio (>2.4) after V_g is less than -40V can be attributed to the fact that the thickness of the ZZ sample (thickness = 11.5 nm) is thinner than the AC sample (thickness = 20 nm), as mentioned in Fig. 4.11 (b) and Fig. 4.12 (b). As a result, when the back gate voltage sweeps to a large negative bias, a thinner film will suffer the surface roughness scattering at the BP/SiO₂ interface worse than a thicker film, resulting in a faster drop of the mobility and the increasing μ_{AC}/μ_{ZZ} ratio.

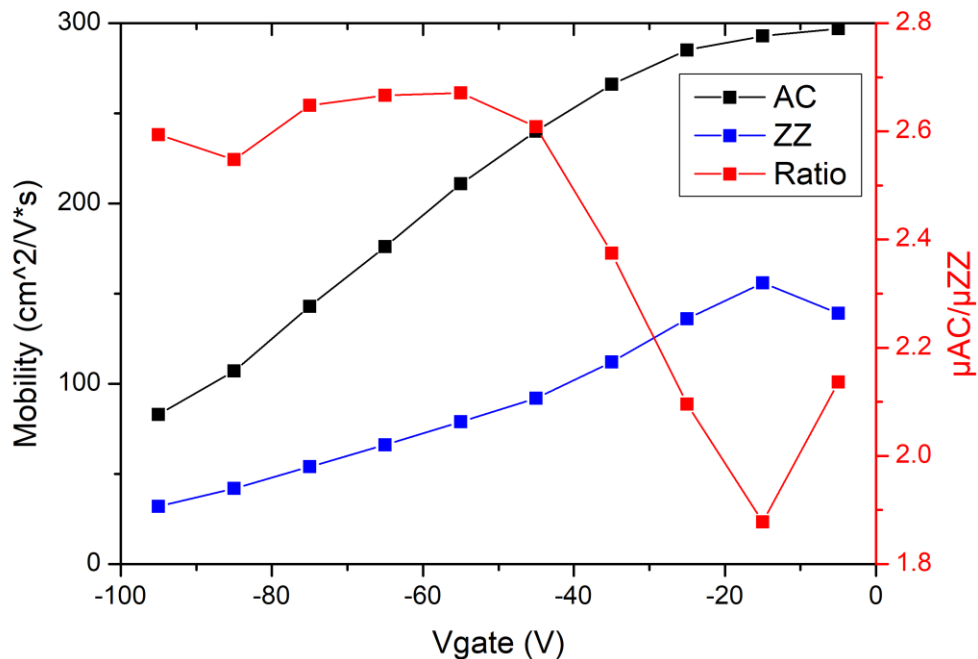


Fig. 4.15 The mobilities along AC (black line) and ZZ (blue line) directions and the μ_{AC}/μ_{ZZ} ratio versus back gate bias (red line), the ZZ and AC samples are mentioned in Fig 4.11 and Fig. 4.12, respectively.

On the other hand, Fig. 4.16 displays the hole mobility and the μ_{AC}/μ_{ZZ} ratio versus back gate bias based on the sample in Fig. 4.13. Notice that the peak mobility occurs at $V_g = 25V$ for both AC and ZZ directions. The drop of mobility is due to the surface roughness scattering. Since these two samples share the same BP film and thus the same thickness, the impact of surface scattering on these two devices can also be seemed as the same. Originally, the μ_{AC}/μ_{ZZ} ratio = 1.52 at $V_g = 25V$, and then gradually decreases as the back gate bias sweeps to $-100V$, implying that at large negative bias, the scattering mechanism will become the dominant factor to affect the mobility, while the influence of different transport directions will become less important.

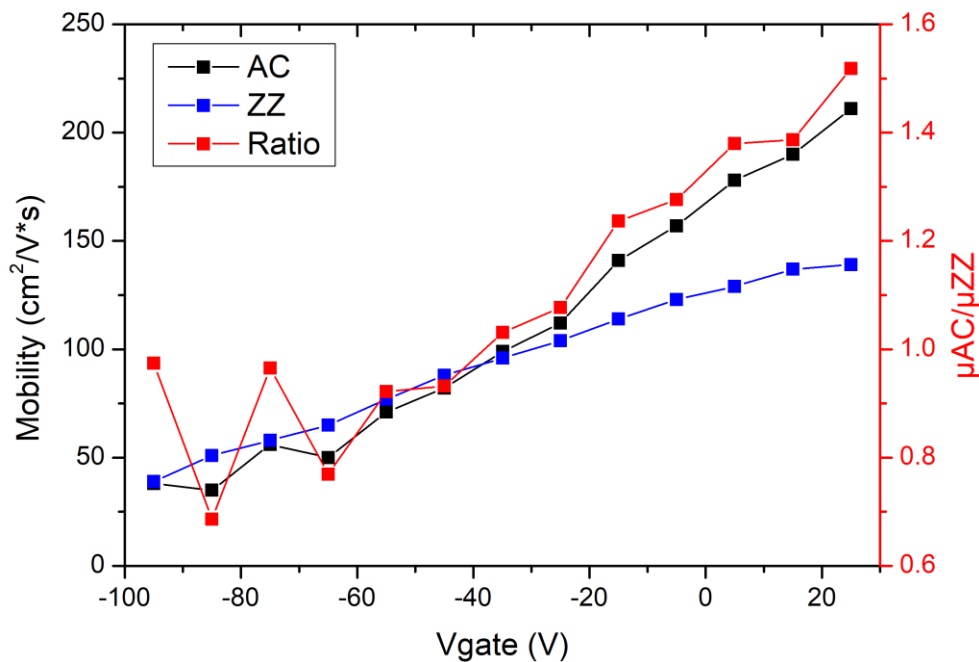


Fig. 4.16 The mobilities along AC (black line) and ZZ (blue line) directions and

the μ_{AC}/μ_{ZZ} ratio versus back gate bias (red line), the AC and ZZ samples are

mentioned in Fig. 4.13.



4.5 Characteristics of P-N BP/WS₂ Heterostructure and BP Homostructure

In this section, the fabrication of P-N junction is realized through the BP-WS₂ heterostructure and the homojunction of BP with different thicknesses. Their electrical and optical properties will also be measured and discussed.

4.5.1 Device Process Flow for BP-WS₂ Heterostructure

The process flow of the fabrication process for the BP-WS₂ heterostructure p-n junction is shown in Fig. 4.17. First, the BP flakes were mechanically exfoliated and transferred onto a patterned 300 nm SiO₂/p⁺⁺ Si substrate as shown in Fig. 4.18 (a). After choosing the proper BP films and acetone bath, WS₂ flake was transferred onto the top of BP as shown in Fig. 4.18 (b) by using dry transfer. After second acetone bath for 1 hour, the S/D electrodes would be defined by E-beam lithography, followed by thermal evaporation of Cr (10 nm)/Au (70 nm) contact metal for WS₂, and AuGe alloy (80 nm) for BP, respectively. Finally, after lift-off process, the device was thermal annealed at 200°C for 1 minute in N₂ to have better contact between WS₂ and black phosphorus. Fig. 4.18 (c) shows the completed devices under optical

microscopy. Fig. 4.18 (d) shows the cross-sectional diagram of the completed devices.

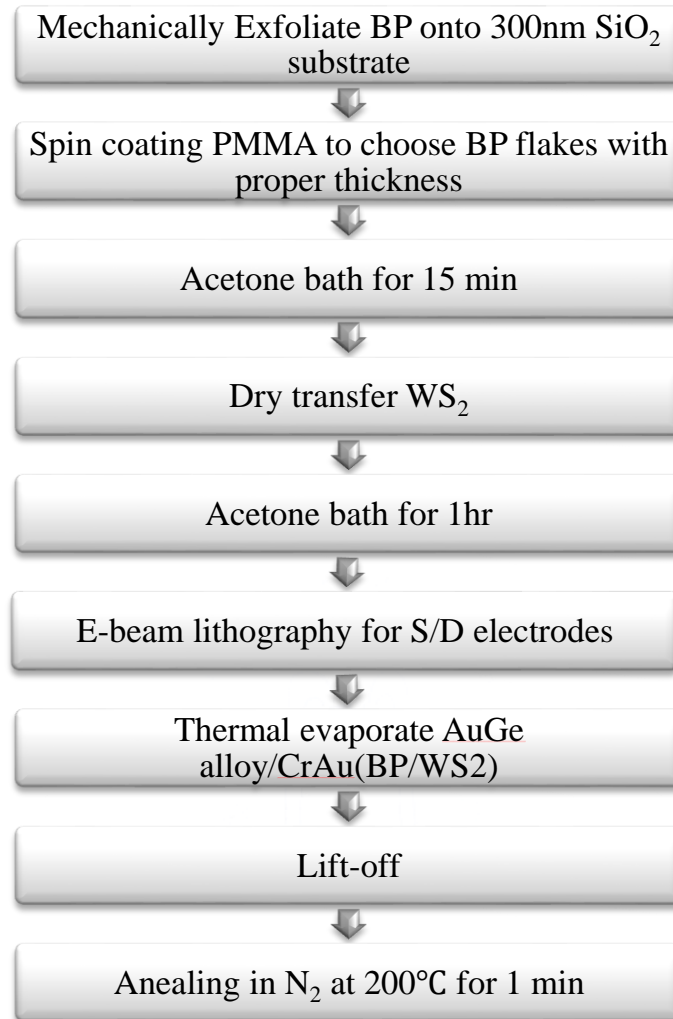


Fig. 4.17 The flow chart for BP-WS₂ heterostructure fabrication process

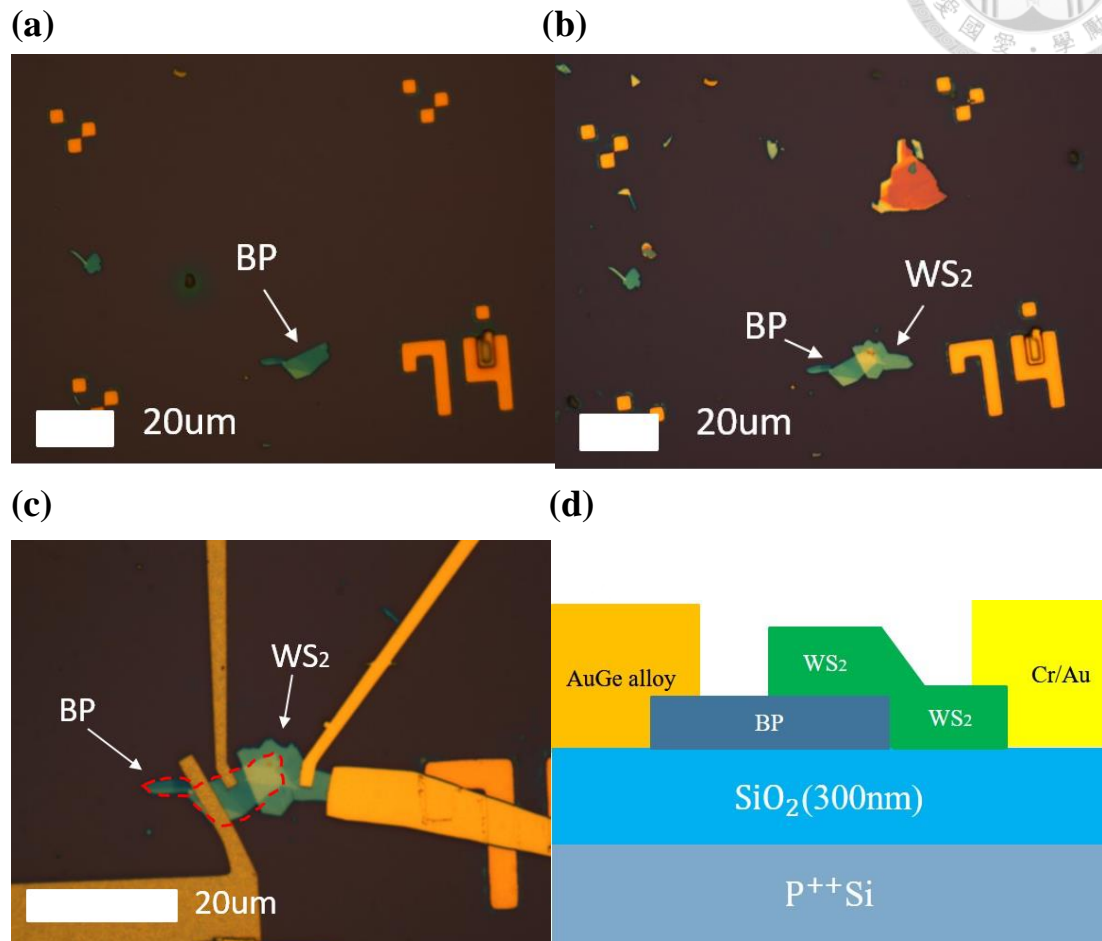


Fig. 4.18 (a) BP flakes on 300nm SiO₂ substrate (b) Dry transfer WS₂ onto BP (c) Completed device under optical microscope (d) Schematic diagram of the completed device.

4.5.2 Device Performance

Fig. 4.19 (a) and (b) shows the I_d - V_d curve of BP-WS₂ heterostructure P-N diode in log and linear scale, respectively. In order to further discuss its characteristics, we will consider the ideality factor (n), which is an important parameter to determine the

quality of a P-N diode. The ideality factor n can be extracted from the I_d - V_d plot in log scale and using the slope as shown in the red dashed line in Fig. 4.19 (a), following these equations.

$$I = I_0(e^{\frac{qV}{nkT}} - 1)$$

(4.2)

$$n = \frac{q}{kT \times \ln(10) \times \text{slope}}$$

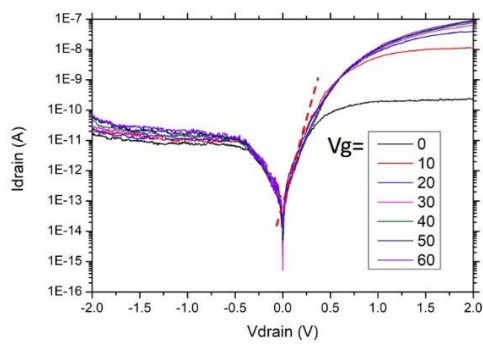
(4.3)

where n is the ideality factor, I is the current of diode, I_0 is the saturation current, $\frac{kT}{q} = 25.9$ mV at room temperature and V is the applied voltage. The ideality factor and the on/off ratio of the heterostructure P-N diode under different back gate bias is shown in Fig. 4.20. The current rectification ratio which is defined as forward current (I_F) divided by reverse current (I_R) at $|V_d| = 2V$ is about 3 order, and the ideality factor is in the range of 1.71 to 2.15, which indicates that the forward current is dominated by recombination current. These results show great electrical performance of the BP-WS₂ heterostructure P-N diode.

In order to further discuss the optical characteristics of BP-WS₂ heterostructure P-N diode, Xe lamp was used as a broadband light source to measure its optical properties. The emission spectra of Xe lamp is shown in Fig. 4.21.



(a)



(b)

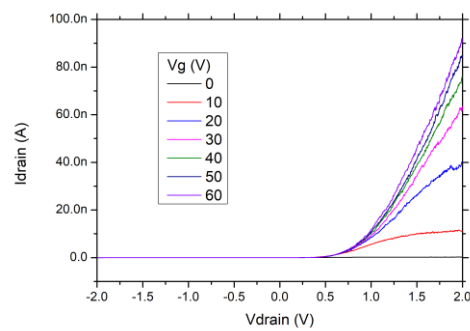


Fig. 4.19 I_d versus V_d of BP-WS₂ heterostructure P-N diode in (a) log scale (b)

linear scale. Note that the red dashed line can extract the ideality factor (n) of this device.

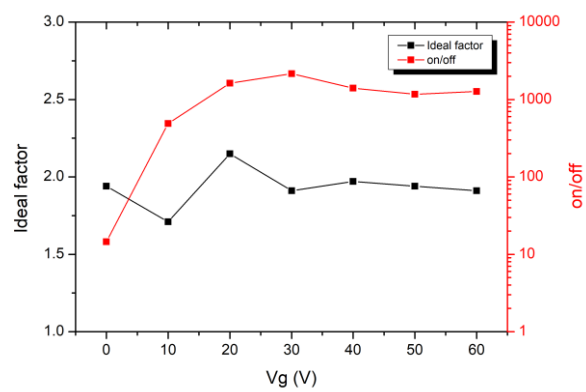


Fig. 4.20 The ideality factor and on/off ratio of BP-WS₂ heterostructure P-N diode under different back gate bias.

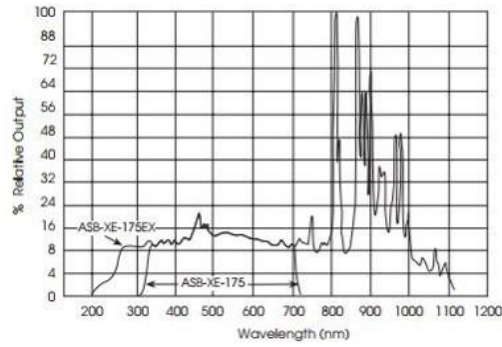


Fig. 4.21 The emission spectra of Xe lamp.

The incident light with intensities at 40.37, 222, and 4720 $\mu\text{W}/\text{cm}^2$ would be used to measure the photoresponse of BP- WS_2 heterostructure P-N diode. Fig. 4.22 (a) and (b) show the forward and reverse I_d - V_d curve under dark and various incident light intensities from 40.37 to 4720 $\mu\text{W}/\text{cm}^2$, respectively. The red dashed circle in Fig. 4.22 (a) is enlarged in Fig. 4.22 (b) and shows the details of the negative V_d bias region. Under forward and reverse bias, as the incident light intensity increases, the photocurrent becomes larger. At $V_{ds} = 0\text{V}$, the diode didn't show any photoresponse, indicating that the BP- WS_2 heterostructure P-N diode is not a photodiode but a photoconductor. At $V_{ds} = 2\text{V}$, the photocurrent I_{ph} , which is defined as $I_{illumination} - I_{dark}$, where $I_{illumination}$ and I_{dark} are the drain current I_d with and without light illumination, are 2.26, 3.49 and 22 nA for incident light intensity 40.37, 222 and 4720 $\mu\text{W}/\text{cm}^2$, respectively. At $V_{ds} = -2\text{V}$, the photocurrents are 66, 329 and 661 pA for incident light intensity 40.37, 222 and 4720 $\mu\text{W}/\text{cm}^2$, respectively. Fig. 4.23 shows the responsivity R of the diode versus light intensity at $V_{ds} = \pm 2\text{V}$. The responsivity R is defined as

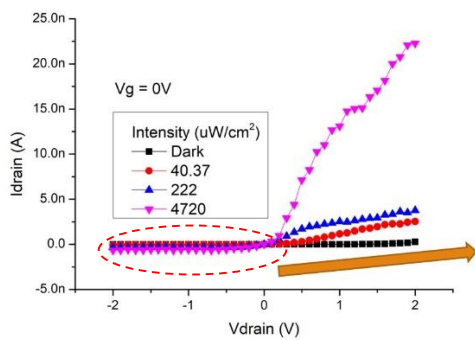
I_{ph}/P_{laser} , where P_{laser} is the incident light intensity multiply by the device area ($97 \mu\text{m}^2$).

At $V_{ds} = 2\text{V}$, the responsivities are 57.9, 16.2 and 10.9 A/W for incident light intensity 40.37, 222 and 4720 $\mu\text{W}/\text{cm}^2$, respectively. At $V_{ds} = -2\text{V}$, the responsivities are 1.69,

1.53 and 0.18 A/W for incident light intensity 40.37, 222 and 4720 $\mu\text{W}/\text{cm}^2$, respectively. The responsivity would decrease as the light intensity increases, which is

consistent with the theory and shows great optical response of the heterostructure.

(a)



(b)

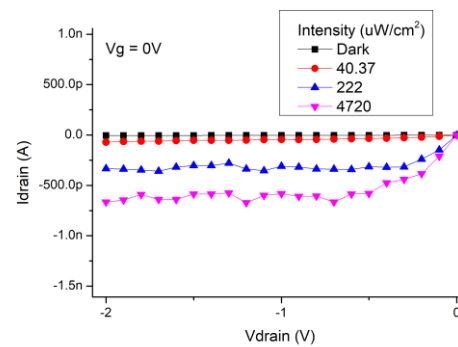


Fig. 4.22 (a) I_d versus V_d characteristics of BP- WS_2 heterostructure under various incident light intensity (b) Enlarged graph of (a) at $V_d < 0$.

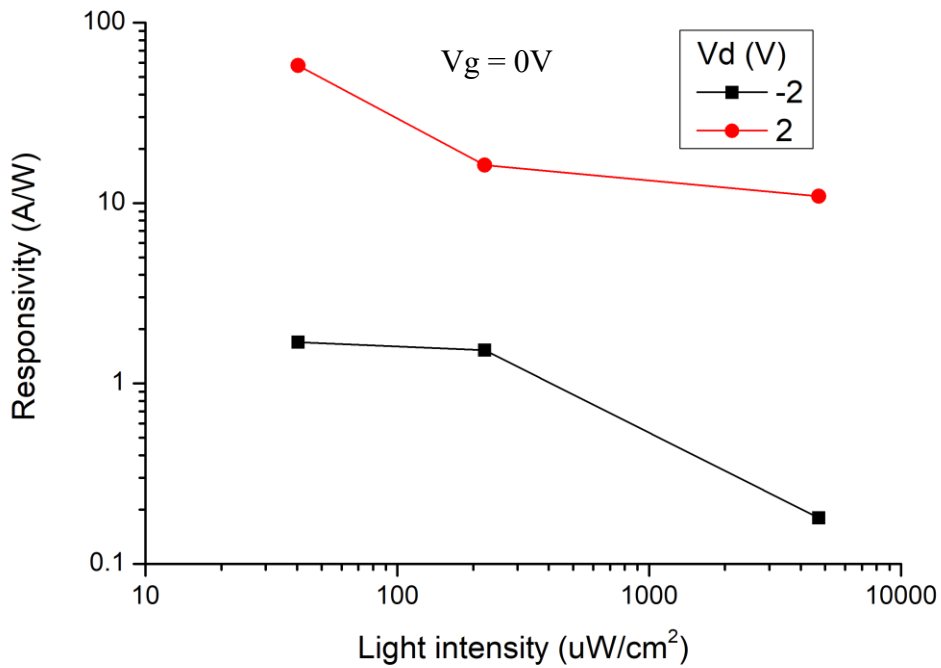


Fig. 4.23 Responsivity of BP-WS₂ Heterostructure versus incident light intensity.

To further investigate the BP-WS₂ heterostructure, the ideal energy band diagram of the heterostructure under thermal equilibrium before contact are shown in Fig. 4.24. The energy band diagram of BP has been shown in Chapter 3. The work function, electron affinity and bandgap of WS₂ is 4.3, 4.15 and 1.3 eV, respectively. To simplify the analysis, assume there are no interface states at the junction interface. According to the band diagram, the barrier height of holes is much larger than that of electrons, indicating that the forward current of the heterostructure is mainly contributed by electrons.

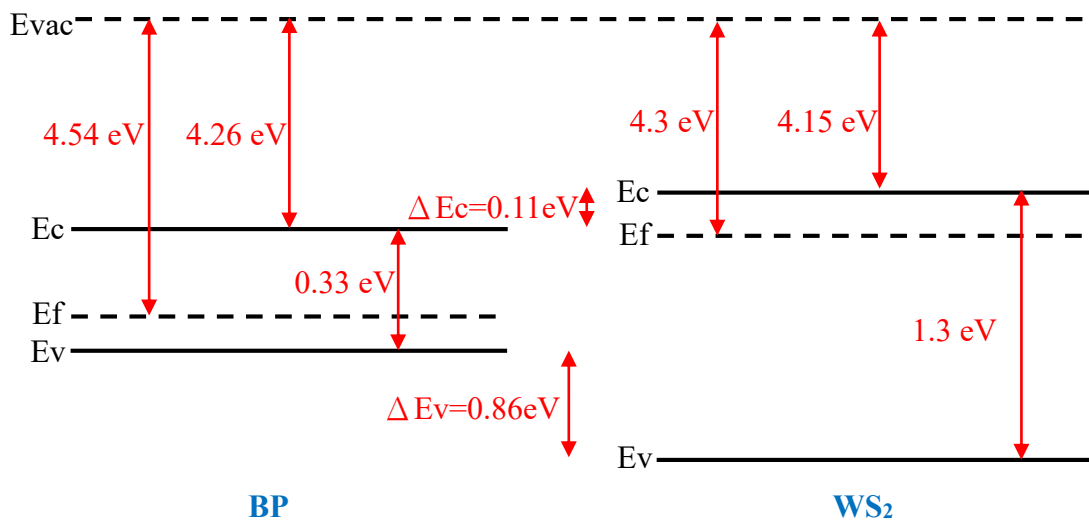
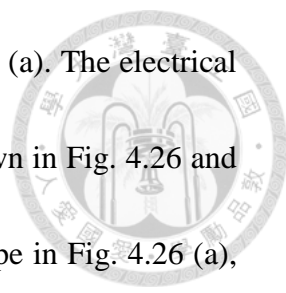


Fig. 4.24 Ideal Band diagram of BP-WS₂ Heterostructure before contact.



4.5.3 BP Homostructure P-N-Like Diode through Thickness Control

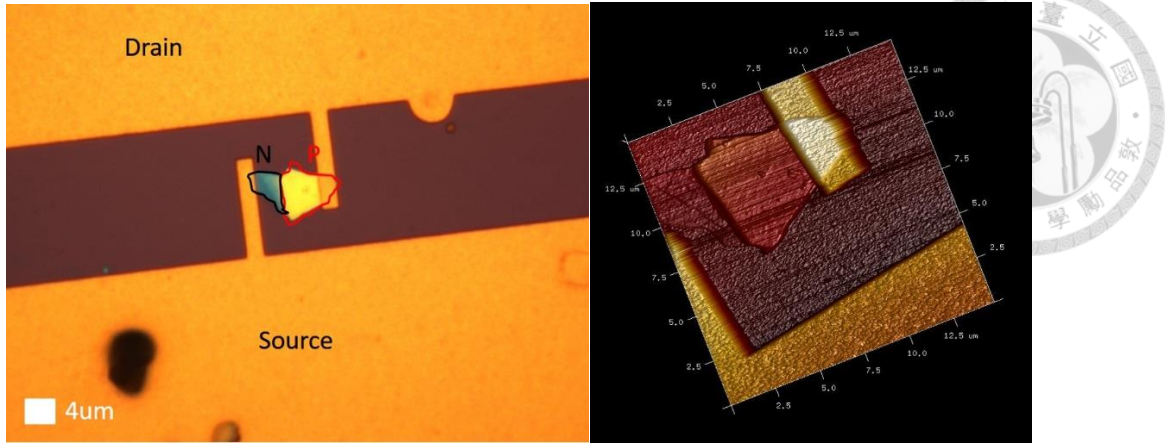
According to Fig. 4.5, the 4 nm BP film can be better gated by the back gate, which can be observed from the negative shift of the threshold voltage. As a result, if the threshold voltage of the BP TFT can be controlled through thickness, then the BP homostructure P-N-like diode can be realized. Fig. 4.25 shows the optical and AFM image of the BP homostructure P-N-like diode. Notice that in Fig. 4.25 (d), the thickness of the thick part can be up to 45~50 nm, while the thin part can be down to



only 10~15 nm, which agrees with the color difference in Fig. 4.25 (a). The electrical and optical properties of the homostructure P-N-like diode are shown in Fig. 4.26 and Table 4.7. The ideality factor, which can be extracted from the slope in Fig. 4.26 (a), is about 1.98, implying that the forward current is dominated by recombination current. The current rectification ratio, which is defined as forward current (I_F) divided by reverse current (I_R) at $|V_d| = 1V$ is about 2.3×10^1 . To further explore the optical responsivity of the device, 850 nm NIR Laser in optical fiber is used as the light source, and the intensity = 16.3 W/cm^2 . At $V_{ds} = 1V$ and $-1V$, the photocurrents are 270 and 7.26 nA, respectively. The device area = 34.5 um^2 . The responsivities at $V_d = \pm 1V$ are 47.76 and 1.29 mA/W, respectively. Notice that at $V_{ds} = 0V$, the diode also didn't show any photoresponse, indicating that the BP homostructure P-N-like diode is not a photodiode but a photoconductor. The device performance of the homostructure P-N-like diode is comparable to the BP- WS_2 heterostructure and shows great potential of BP in the applications of infrared photodetector due to the small direct bandgap ($=0.33 \text{ eV}$) of bulk BP [106-108].

(a)

(b)



(c)

(d)

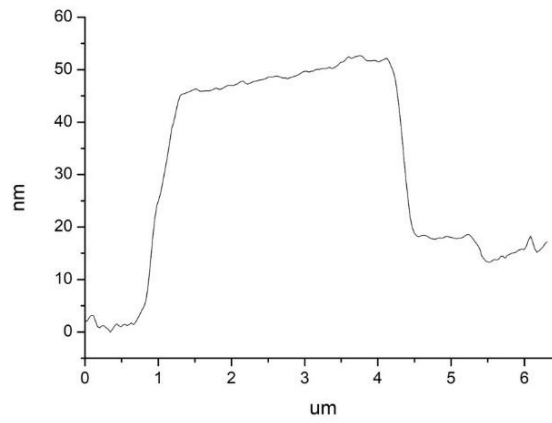
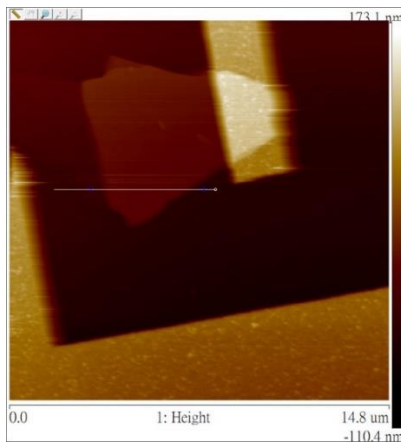
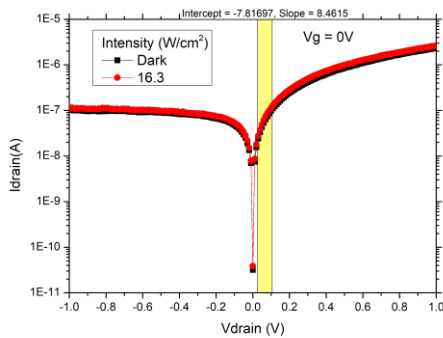


Fig. 4.25 BP homostructure P-N-like diode under (a) Optical microscope (b) 3D AFM image (c) 2D AFM image, the white line indicates the position of the line profiles shown in (d). (d) The result of the AFM measurement.

(a)



(b)

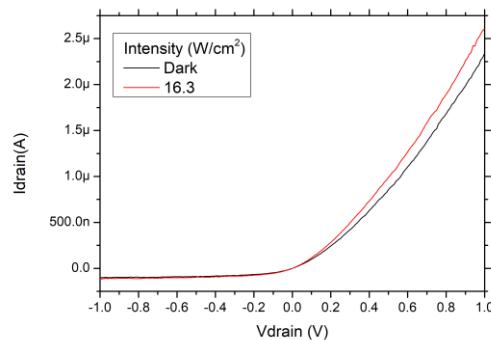


Fig. 4.26 Id-Vd plot of the homojunction P-N-like diode in (a) log scale (b) linear scale. Notice that at Vds = 0V, the diode also didn't show any photoresponse, indicating that the homojunction P-N-like diode is not a photodiode but a photoconductor.

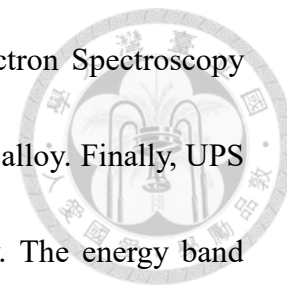
Table 4.7 Device performance of the homojunction P-N-like diode

Ideality Factor	On/Off	Responsivity @ Vd = 1V (mA/W)	Responsivity @ Vd = -1V (mA/W)
1.98	2.3×10^1	47.76	1.29

Chapter 5 Conclusion

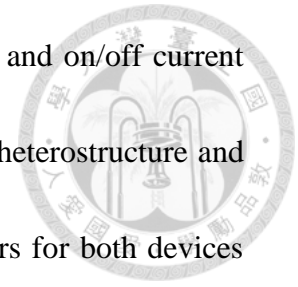
In Chapter 3, the lattice constant of bulk BP are determined by X-ray Diffraction (XRD). The thickness of the BP nanosheets can be roughly determined by optical microscopy (OM) and atomic force microscopy (AFM). The orientation of BP thin films can be recognized by Raman spectra. According to the intensity ratio of A²g to A¹g, the long and short sides of the rectangular BP thin films are found to be zigzag

(ZZ) and armchair (AC) directions, respectively. X-ray Photoelectron Spectroscopy (XPS) is used to study the elemental composition of BP and AuGe alloy. Finally, UPS is utilized to study the energy states of bulk BP and AuGe alloy. The energy band diagram of bulk BP is also obtained.



In Chapter 4, back-gated BP TFTs on 300nm SiO₂ substrate were successfully fabricated. It is found that after thermal annealing at 200°C in the nitrogen environment for 1 minute, both the hole mobility and the on/off current ratio of the BP TFT can be significantly improved. Section 4.2 discusses the thickness dependent properties of the BP TFT. The optimized thickness for BP TFT is found to be around 10nm, while for thickness larger than 10nm, the interlayer resistance and screening effect will weaken the mobility and drain current modulation. As for thickness less than 10nm, interface scattering will severely degrade the mobility. In Section 4.3, several metal contacts for BP TFTs are studied through Transmission Line Method (TLM). Terrific Ohmic contact between BP and metal is obtained due to the small bandgap of BP ($= 0.33\text{eV}$). Based on the result of TLM, AuGe alloy is found to have the lowest contact resistance. In Section 4.4, the anisotropic properties of BP are investigated through rectangular BP TFTs. The mobility ratio between AC/ZZ directions of BP is found to be dependent with thickness and back gate bias. Using AuGe alloy as the metal contact and AC direction as the carrier transport orientation,

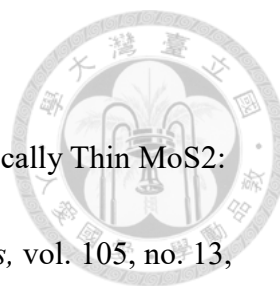
high performance BP TFT with hole mobility up to $298 \text{ cm}^2/\text{V}\cdot\text{s}$ and on/off current ratio up to 3 orders is obtained. Finally, P-N diode with BP-WS₂ heterostructure and BP homostructure were successfully fabricated. The ideality factors for both devices were found to be about 2, suggesting that the forward current is dominated by recombination current. The ideal energy band diagram under thermal equilibrium for BP-WS₂ heterostructure is used to indicate that the forward current of the heterostructure is mainly contributed by electrons. The optical responsivities show great potential of BP in the applications of optoelectronics due to the direct bandgap of BP.



References



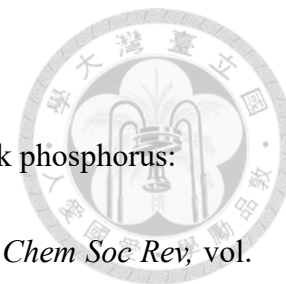
- [1] P. R. Wallace, "THE BAND THEORY OF GRAPHITE," *Physical Review*, vol. 71, no. 7, pp. 476-476, 1947.
- [2] K. S. Novoselov, A. K. Geim, S. V. Morozov, D. Jiang, Y. Zhang, S. V. Dubonos, I. V. Grigorieva, and A. A. Firsov, "Electric field effect in atomically thin carbon films," *Science*, vol. 306, no. 5696, pp. 666-9, Oct 22, 2004.
- [3] A. H. C. Neto, and K. Novoselov, "Two-Dimensional Crystals: Beyond Graphene," *Materials Express*, vol. 1, no. 1, pp. 10-17, 2011.
- [4] A. Loiseau, F. Willaime, N. Demoncy, G. Hug, and H. Pascard, "Boron nitride nanotubes with reduced numbers of layers synthesized by arc discharge," *Phys Rev Lett*, vol. 76, no. 25, pp. 4737-4740, Jun 17, 1996.
- [5] K. S. Novoselov, A. K. Geim, S. V. Morozov, D. Jiang, M. I. Katsnelson, I. V. Grigorieva, S. V. Dubonos, and A. A. Firsov, "Two-dimensional gas of massless Dirac fermions in graphene," *Nature*, vol. 438, no. 7065, pp. 197-200, Nov 10, 2005.
- [6] J. C. Slater, G. F. Koster, and J. H. Wood, "Symmetry and Free Electron Properties of the Gallium Energy Bands," *Physical Review*, vol. 126, no. 4, pp. 1307-1317, 1962.
- [7] F. Schwierz, "Graphene transistors," *Nat Nanotechnol*, vol. 5, no. 7, pp.



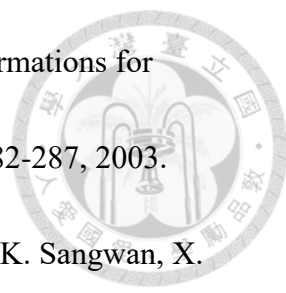
487-96, Jul, 2010.

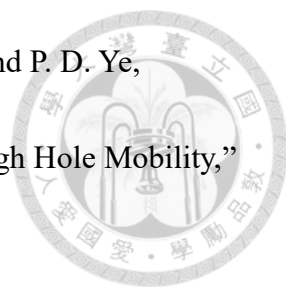
- [8] K. F. Mak, C. Lee, J. Hone, J. Shan, and T. F. Heinz, "Atomically Thin MoS₂: A New Direct-Gap Semiconductor," *Physical Review Letters*, vol. 105, no. 13, pp. 4, Sep, 2010.
- [9] B. Radisavljevic, A. Radenovic, J. Brivio, V. Giacometti, and A. Kis, "Single-layer MoS₂ transistors," *Nat Nanotechnol*, vol. 6, no. 3, pp. 147-50, Mar, 2011.
- [10] Q. H. Wang, K. Kalantar-Zadeh, A. Kis, J. N. Coleman, and M. S. Strano, "Electronics and optoelectronics of two-dimensional transition metal dichalcogenides," *Nature Nanotechnology*, vol. 7, no. 11, pp. 699-712, Nov, 2012.
- [11] H. Schmidt, F. Giustiniano, and G. Eda, "Electronic transport properties of transition metal dichalcogenide field-effect devices: surface and interface effects," *Chemical Society Reviews*, vol. 44, no. 21, pp. 7715-7736, 2015.
- [12] C. Gong, L. Colombo, R. M. Wallace, and K. Cho, "The unusual mechanism of partial Fermi level pinning at metal-MoS₂ interfaces," *Nano Lett*, vol. 14, no. 4, pp. 1714-20, 2014.
- [13] L. K. Li, Y. J. Yu, G. J. Ye, Q. Q. Ge, X. D. Ou, H. Wu, D. L. Feng, X. H. Chen, and Y. B. Zhang, "Black phosphorus field-effect transistors," *Nature*

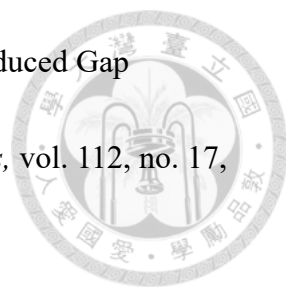
Nanotechnology, vol. 9, no. 5, pp. 372-377, May, 2014.

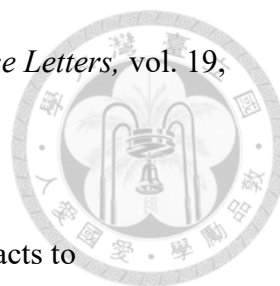


- [14] H. Liu, Y. Du, Y. Deng, and P. D. Ye, "Semiconducting black phosphorus: synthesis, transport properties and electronic applications," *Chem Soc Rev*, vol. 44, no. 9, pp. 2732-43, May 07, 2015.
- [15] S. Lange, P. Schmidt, and T. Nilges, "Au₃SnP₇@black phosphorus: an easy access to black phosphorus," *Inorg Chem*, vol. 46, no. 10, pp. 4028-35, May 14, 2007.
- [16] P. W. Bridgman, "Two new modifications of phosphorus," *Journal of the American Chemical Society*, vol. 36, pp. 1344-1363, Jul-Dec, 1914.
- [17] T. Nishii, Y. Maruyama, T. Inabe, and I. Shirotnani, "SYNTHESIS AND CHARACTERIZATION OF BLACK PHOSPHORUS INTERCALATION COMPOUNDS," *Synthetic Metals*, vol. 18, no. 1-3, pp. 559-564, Feb, 1987.
- [18] D. Warschauer, "Electrical and Optical Properties of Crystalline Black Phosphorus," *Journal of Applied Physics*, vol. 34, no. 7, pp. 1853-1860, 1963.
- [19] A. Brown, and S. Rundqvist, "Refinement of the crystal structure of black phosphorus," *Acta Crystallographica*, vol. 19, no. 4, pp. 684-685, 1965.
- [20] Y. Maruyama, S. Suzuki, K. Kobayashi, and S. Tanuma, "Synthesis and some properties of black phosphorus single crystals," *Physica B+C*, vol. 105, no. 1-3, pp. 99-102, 1981.

- 
- [21] R. Ahuja, “Calculated high pressure crystal structure transformations for phosphorus,” *physica status solidi (b)*, vol. 235, no. 2, pp. 282-287, 2003.
- [22] J. D. Wood, S. A. Wells, D. Jariwala, K. S. Chen, E. Cho, V. K. Sangwan, X. Liu, L. J. Lauhon, T. J. Marks, and M. C. Hersam, “Effective passivation of exfoliated black phosphorus transistors against ambient degradation,” *Nano Lett*, vol. 14, no. 12, pp. 6964-70, Dec 10, 2014.
- [23] R. W. Keyes, “The Electrical Properties of Black Phosphorus,” *Physical Review*, vol. 92, no. 3, pp. 580-584, 1953.
- [24] A. Castellanos-Gomez, L. Vicarelli, E. Prada, J. O. Island, K. L. Narasimha-Acharya, S. I. Blanter, D. J. Groenendijk, M. Buscema, G. A. Steele, J. V. Alvarez, H. W. Zandbergen, J. J. Palacios, and H. S. J. van der Zant, “Isolation and characterization of few-layer black phosphorus,” *2D Materials*, vol. 1, no. 2, pp. 025001, 2014.
- [25] L. Cartz, S. R. Srinivasa, R. J. Riedner, J. D. Jorgensen, and T. G. Worlton, “EFFECT OF PRESSURE ON BONDING IN BLACK PHOSPHORUS,” *Journal of Chemical Physics*, vol. 71, no. 4, pp. 1718-1721, 1979.
- [26] Y. Akahama, S. Endo, and S.-i. Narita, “Electrical Properties of Black Phosphorus Single Crystals,” *Journal of the Physical Society of Japan*, vol. 52, no. 6, pp. 2148-2155, 1983.

- 
- [27] H. Liu, A. T. Neal, Z. Zhu, Z. Luo, X. F. Xu, D. Tomanek, and P. D. Ye, “Phosphorene: An Unexplored 2D Semiconductor with a High Hole Mobility,” *Acs Nano*, vol. 8, no. 4, pp. 4033-4041, Apr, 2014.
- [28] F. N. Xia, H. Wang, and Y. C. Jia, “Rediscovering black phosphorus as an anisotropic layered material for optoelectronics and electronics,” *Nature Communications*, vol. 5, pp. 6, Jul, 2014.
- [29] V. Tran, R. Soklaski, Y. Liang, and L. Yang, “Layer-controlled band gap and anisotropic excitons in few-layer black phosphorus,” *Physical Review B*, vol. 89, no. 23, 2014.
- [30] J. Qiao, X. Kong, Z. X. Hu, F. Yang, and W. Ji, “High-mobility transport anisotropy and linear dichroism in few-layer black phosphorus,” *Nat Commun*, vol. 5, pp. 4475, Jul 21, 2014.
- [31] A. Favron, E. Gaufres, F. Fossard, A. L. Phaneuf-L'Heureux, N. Y. Tang, P. L. Levesque, A. Loiseau, R. Leonelli, S. Francoeur, and R. Martel, “Photooxidation and quantum confinement effects in exfoliated black phosphorus,” *Nat Mater*, vol. 14, no. 8, pp. 826-32, Aug, 2015.
- [32] K. T. Lam, Z. P. Dong, and J. Guo, “Performance Limits Projection of Black Phosphorous Field-Effect Transistors,” *Ieee Electron Device Letters*, vol. 35, no. 9, pp. 963-965, Sep, 2014.

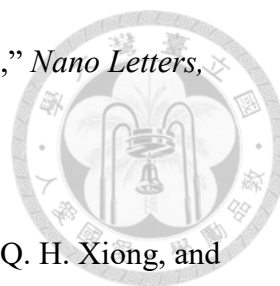
- 
- [33] A. S. Rodin, A. Carvalho, and A. H. Castro Neto, "Strain-Induced Gap Modification in Black Phosphorus," *Physical Review Letters*, vol. 112, no. 17, pp. 5, May, 2014.
- [34] R. X. Fei, and L. Yang, "Strain-Engineering the Anisotropic Electrical Conductance of Few-Layer Black Phosphorus," *Nano Letters*, vol. 14, no. 5, pp. 2884-2889, May, 2014.
- [35] Y. C. Du, H. Liu, Y. X. Deng, and P. D. Ye, "Device Perspective for Black Phosphorus Field-Effect Transistors: Contact Resistance, Ambipolar Behavior, and Scaling," *Acs Nano*, vol. 8, no. 10, pp. 10035-10042, Oct, 2014.
- [36] F. Schwierz, J. Pezoldt, and R. Granzner, "Two-dimensional materials and their prospects in transistor electronics," *Nanoscale*, vol. 7, no. 18, pp. 8261-8283, 2015.
- [37] R. H. Yan, A. Ourmazd, and K. F. Lee, "Scaling the Si MOSFET: from bulk to SOI to bulk," *IEEE Transactions on Electron Devices*, vol. 39, no. 7, pp. 1704-1710, 1992.
- [38] D. J. Frank, R. H. Dennard, E. Nowak, P. M. Solomon, Y. Taur, and W. Hon-Sum Philip, "Device scaling limits of Si MOSFETs and their application dependencies," *Proceedings of the IEEE*, vol. 89, no. 3, pp. 259-288, 2001.
- [39] D. J. Frank, Y. Taur, and H. S. P. Wong, "Generalized scale length for



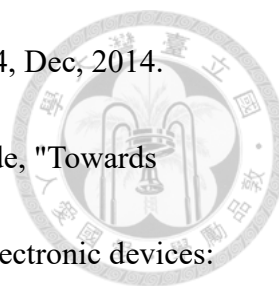
- two-dimensional effects in MOSFET's," *Ieee Electron Device Letters*, vol. 19, no. 10, pp. 385-387, Oct, 1998.
- [40] A. Allain, J. Kang, K. Banerjee, and A. Kis, "Electrical contacts to two-dimensional semiconductors," *Nat Mater*, vol. 14, no. 12, pp. 1195-205, Dec, 2015.
- [41] S. P. Koenig, R. A. Doganov, H. Schmidt, A. H. Castro Neto, and B. Özyilmaz, "Electric field effect in ultrathin black phosphorus," *Applied Physics Letters*, vol. 104, no. 10, pp. 103106, 2014.
- [42] M. Buscema, D. J. Groenendijk, S. I. Blanter, G. A. Steele, H. S. J. van der Zant, and A. Castellanos-Gomez, "Fast and Broadband Photoresponse of Few-Layer Black Phosphorus Field-Effect Transistors," *Nano Letters*, vol. 14, no. 6, pp. 3347-3352, Jun, 2014.
- [43] J. Quereda, P. San-Jose, V. Parente, L. Vaquero-Garzon, A. J. Molina-Mendoza, N. Agrait, G. Rubio-Bollinger, F. Guinea, R. Roldan, and A. Castellanos-Gomez, "Strong Modulation of Optical Properties in Black Phosphorus through Strain-Engineered Rippling," *Nano Lett*, vol. 16, no. 5, pp. 2931-7, May 11, 2016.
- [44] T. Low, A. S. Rodin, A. Carvalho, Y. Jiang, H. Wang, F. Xia, and A. H. Castro Neto, "Tunable optical properties of multilayer black phosphorus thin films,"



- Physical Review B*, vol. 90, no. 7, 2014.
- [45] Q. Guo, A. Pospischil, M. Bhuiyan, H. Jiang, H. Tian, D. Farmer, B. Deng, C. Li, S. J. Han, H. Wang, Q. Xia, T. P. Ma, T. Mueller, and F. Xia, "Black Phosphorus Mid-Infrared Photodetectors with High Gain," *Nano Lett*, vol. 16, no. 7, pp. 4648-55, Jul 13, 2016.
- [46] S. Das, M. Demarteau, and A. Roelofs, "Ambipolar Phosphorene Field Effect Transistor (vol 8, pg 11730, 2014)," *Acs Nano*, vol. 10, no. 2, pp. 2984-2984, Feb, 2016.
- [47] T. Hong, B. Chamlagain, W. Z. Lin, H. J. Chuang, M. H. Pan, Z. X. Zhou, and Y. Q. Xu, "Polarized photocurrent response in black phosphorus field-effect transistors," *Nanoscale*, vol. 6, no. 15, pp. 8978-8983, Aug, 2014.
- [48] T. Low, M. Engel, M. Steiner, and P. Avouris, "Origin of photoresponse in black phosphorus phototransistors," *Physical Review B*, vol. 90, no. 8, pp. 5, Aug, 2014.
- [49] J. W. Jiang, B. S. Wang, and H. S. Park, "Interlayer breathing and shear modes in few-layer black phosphorus," *Journal of Physics-Condensed Matter*, vol. 28, no. 16, pp. 10, Apr, 2016.
- [50] X. Ling, L. B. Liang, S. X. Huang, A. A. Puretzky, D. B. Geohegan, B. G. Sumpter, J. Kong, V. Meunier, and M. S. Dresselhaus, "Low-Frequency



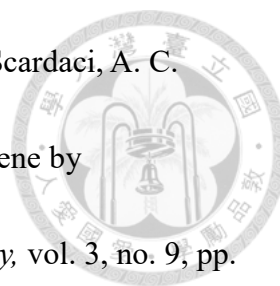
- Interlayer Breathing Modes in Few-Layer Black Phosphorus,” *Nano Letters*, vol. 15, no. 6, pp. 4080-4088, Jun, 2015.
- [51] X. Luo, X. Lu, G. K. W. Koon, A. H. C. Neto, B. Ozyilmaz, Q. H. Xiong, and S. Y. Quek, “Large Frequency Change with Thickness in Interlayer Breathing Mode-Significant Interlayer Interactions in Few Layer Black Phosphorus,” *Nano Letters*, vol. 15, no. 6, pp. 3931-3938, Jun, 2015.
- [52] J. O. Island, G. A. Steele, H. S. J. van der Zant, and A. Castellanos-Gomez, “Environmental instability of few-layer black phosphorus,” *2d Materials*, vol. 2, no. 1, pp. 6, Mar, 2015.
- [53] J. B. Smith, D. Hagaman, and H.-F. J. N. Ji, “Growth of 2D black phosphorus film from chemical vapor deposition,” vol. 27, no. 21, pp. 215602, 2016.
- [54] Y. Hsiao, P. Y. Chang, K. L. Fan, N. C. Hsu, and S. C. Lee, “Black phosphorus with a unique rectangular shape and its anisotropic properties,” *Aip Advances*, vol. 8, no. 10, pp. 7, Oct, 2018.
- [55] J. H. Kang, D. Sarkar, Y. Khatami, and K. Banerjee, “Proposal for all-graphene monolithic logic circuits,” *Applied Physics Letters*, vol. 103, no. 8, pp. 5, Aug, 2013.
- [56] R. Kappera, D. Voiry, S. E. Yalcin, B. Branch, G. Gupta, A. D. Mohite, and M. Chhowalla, “Phase-engineered low-resistance contacts for ultrathin MoS₂



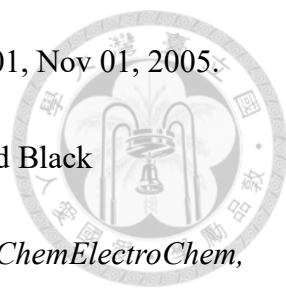
- transistors," *Nature Materials*, vol. 13, no. 12, pp. 1128-1134, Dec, 2014.
- [57] Y. Deng, N. J. Conrad, Z. Luo, H. Liu, X. Xu, and D. Y. Peide, "Towards high-performance two-dimensional black phosphorus optoelectronic devices: The role of metal contacts." pp. 5.2. 1-5.2. 4.
- [58] D. J. Perello, S. H. Chae, S. Song, and Y. H. Lee, "High-performance n-type black phosphorus transistors with type control via thickness and contact-metal engineering," *Nat Commun*, vol. 6, pp. 7809, Jul 30, 2015.
- [59] Y. Q. Ma, C. F. Shen, A. Y. Zhang, L. Chen, Y. H. Liu, J. H. Chen, Q. Z. Liu, Z. Li, M. R. Amer, T. Nilges, A. N. Abbas, and C. W. Zhou, "Black Phosphorus Field-Effect Transistors with Work Function Tunable Contacts," *Acs Nano*, vol. 11, no. 7, pp. 7126-7133, Jul, 2017.
- [60] N. Haratipour, and S. J. Koester, "Ambipolar Black Phosphorus MOSFETs With Record n-Channel Transconductance," *Ieee Electron Device Letters*, vol. 37, no. 1, pp. 103-106, Jan, 2016.
- [61] C. H. Wang, J. A. C. Incorvia, C. J. McClellan, A. C. Yu, M. J. Mleczko, E. Pop, and H. S. P. Wong, "Unipolar n-Type Black Phosphorus Transistors with Low Work Function Contacts," *Nano Letters*, vol. 18, no. 5, pp. 2822-2827, May, 2018.
- [62] D. Xiang, C. Han, J. Wu, S. Zhong, Y. Y. Liu, J. D. Lin, X. A. Zhang, W. P. Hu,

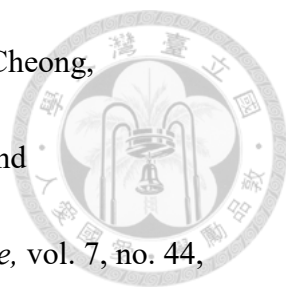


- B. Ozyilmaz, A. H. C. Neto, A. T. S. Wee, and W. Chen, "Surface transfer doping induced effective modulation on ambipolar characteristics of few-layer black phosphorus," *Nature Communications*, vol. 6, pp. 8, Mar, 2015.
- [63] P. D. Zhao, D. Kiriya, A. Azcatl, C. X. Zhang, M. Tosun, Y. S. Liu, M. Hettick, J. S. Kang, S. McDonnell, K. C. Santosh, J. H. Guo, K. Cho, R. M. Wallace, and A. Javey, "Air Stable p-Doping of WSe₂ by Covalent Functionalization," *Acs Nano*, vol. 8, no. 10, pp. 10808-10814, Oct, 2014.
- [64] Y. Du, L. Yang, H. Zhou, and P. D. Ye, "Performance Enhancement of Black Phosphorus Field-Effect Transistors by Chemical Doping," *IEEE Electron Device Letters*, vol. 37, no. 4, pp. 429-432, 2016.
- [65] Y. M. Shi, W. Zhou, A. Y. Lu, W. J. Fang, Y. H. Lee, A. L. Hsu, S. M. Kim, K. Kim, H. Y. Yang, L. J. Li, J. C. Idrobo, and J. Kong, "van der Waals Epitaxy of MoS₂ Layers Using Graphene As Growth Templates," *Nano Letters*, vol. 12, no. 6, pp. 2784-2791, Jun, 2012.
- [66] W. Choi, N. Choudhary, G. H. Han, J. Park, D. Akinwande, and Y. H. Lee, "Recent development of two-dimensional transition metal dichalcogenides and their applications," *Materials Today*, vol. 20, no. 3, pp. 116-130, Apr, 2017.
- [67] Y. Hernandez, V. Nicolosi, M. Lotya, F. M. Blighe, Z. Y. Sun, S. De, I. T. McGovern, B. Holland, M. Byrne, Y. K. Gun'ko, J. J. Boland, P. Niraj, G.

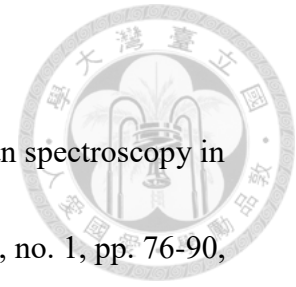


- Duesberg, S. Krishnamurthy, R. Goodhue, J. Hutchison, V. Scardaci, A. C. Ferrari, and J. N. Coleman, "High-yield production of graphene by liquid-phase exfoliation of graphite," *Nature Nanotechnology*, vol. 3, no. 9, pp. 563-568, Sep, 2008.
- [68] J. J. Pei, X. Gai, J. Yang, X. B. Wang, Z. F. Yu, D. Y. Choi, B. Luther-Davies, and Y. R. Lu, "Producing air-stable monolayers of phosphorene and their defect engineering," *Nature Communications*, vol. 7, pp. 8, Jan, 2016.
- [69] H. Y. Chen, W. W. Fei, J. X. Zhou, C. Y. Miao, and W. L. Guo, "Layer Identification of Colorful Black Phosphorus," *Small*, vol. 13, no. 5, pp. 5, Feb, 2017.
- [70] S. H. Aldave, M. N. Yogeesh, W. Zhu, J. Kim, S. S. Sonde, A. P. Nayak, and D. Akinwande, "Characterization and sonochemical synthesis of black phosphorus from red phosphorus," *2D Materials*, vol. 3, no. 1, pp. 014007, 2016.
- [71] E. Flores, J. R. Ares, A. Castellanos-Gomez, M. Barawi, I. J. Ferrer, and C. Sánchez, "Thermoelectric power of bulk black-phosphorus," *Applied Physics Letters*, vol. 106, no. 2, pp. 022102, 2015.
- [72] J. Heyd, J. E. Peralta, G. E. Scuseria, and R. L. Martin, "Energy band gaps and lattice parameters evaluated with the Heyd-Scuseria-Ernzerhof screened

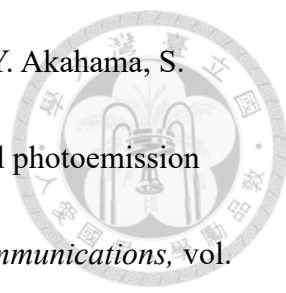
- 
- hybrid functional,” *J Chem Phys*, vol. 123, no. 17, pp. 174101, Nov 01, 2005.
- [73] L. Wang, Z. Sofer, and M. Pumera, “Voltammetry of Layered Black Phosphorus: Electrochemistry of Multilayer Phosphorene,” *ChemElectroChem*, vol. 2, no. 3, pp. 324-327, 2015.
- [74] S. Kuriakose, T. Ahmed, S. Balendhran, V. Bansal, S. Sriram, M. Bhaskaran, and S. Walia, “Black phosphorus: ambient degradation and strategies for protection,” *2d Materials*, vol. 5, no. 3, pp. 10, Jul, 2018.
- [75] E. G. A. Favron, F. Fossard, P.L. Lévesque, A-L. Phaneuf-L'Heureux, N. Y-W. Tang, A. Loiseau, R. Leonelli, S. Francoeur, R. Martel, “Exfoliating pristine black phosphorus down to the monolayer: photo-oxidation and electronic confinement effects,” *Mesoscale and Nanoscale Physics* 2014.
- [76] J. Yang, R. Xu, J. Pei, Y. W. Myint, F. Wang, Z. Wang, S. Zhang, Z. Yu, and Y. Lu, “Optical tuning of exciton and trion emissions in monolayer phosphorene,” *Light: Science & Applications*, vol. 4, no. 7, pp. e312, 2015.
- [77] S. Liu, N. Huo, S. Gan, Y. Li, Z. Wei, B. Huang, J. Liu, J. Li, and H. Chen, “Thickness-dependent Raman spectra, transport properties and infrared photoresponse of few-layer black phosphorus,” *J. Mater. Chem. C*, vol. 3, no. 42, pp. 10974-10980, 2015.

- 
- [78] J. Kim, J. U. Lee, J. Lee, H. J. Park, Z. Lee, C. Lee, and H. Cheong, “Anomalous polarization dependence of Raman scattering and crystallographic orientation of black phosphorus,” *Nanoscale*, vol. 7, no. 44, pp. 18708-18715, 2015.
- [79] C. Q. Han, M. Y. Yao, X. X. Bai, L. Miao, F. Zhu, D. D. Guan, S. Wang, C. L. Gao, C. Liu, D. Qian, Y. Liu, and J.-f. Jia, “Electronic structure of black phosphorus studied by angle-resolved photoemission spectroscopy,” *Physical Review B*, vol. 90, no. 8, 2014.
- [80] S. Zhang, J. Yang, R. Xu, F. Wang, W. Li, M. Ghufran, Y. W. Zhang, Z. Yu, G. Zhang, Q. Qin, and Y. Lu, “Extraordinary photoluminescence and strong temperature/angle-dependent Raman responses in few-layer phosphorene,” *ACS Nano*, vol. 8, no. 9, pp. 9590-6, Sep 23, 2014.
- [81] W. Lu, X. Ma, Z. Fei, J. Zhou, Z. Zhang, C. Jin, and Z. Zhang, “Probing the anisotropic behaviors of black phosphorus by transmission electron microscopy, angular-dependent Raman spectra, and electronic transport measurements,” *Applied Physics Letters*, vol. 107, no. 2, pp. 021906, 2015.
- [82] H. B. Ribeiro, M. A. Pimenta, C. J. de Matos, R. L. Moreira, A. S. Rodin, J. D. Zapata, E. A. de Souza, and A. H. Castro Neto, “Unusual angular dependence of the Raman response in black phosphorus,” *ACS Nano*, vol. 9, no. 4, pp.

4270-6, Apr 28, 2015.

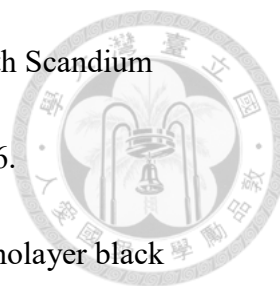


- [83] H. B. Ribeiro, M. A. Pimenta, and C. J. S. de Matos, “Raman spectroscopy in black phosphorus,” *Journal of Raman Spectroscopy*, vol. 49, no. 1, pp. 76-90, Jan, 2018.
- [84] X. Ling, S. X. Huang, E. H. Hasdeo, L. B. Liang, W. M. Parkin, Y. Tatsumi, A. R. T. Nugraha, A. A. Puretzky, P. M. Das, B. G. Sumpter, D. B. Geohegan, J. Kong, R. Saito, M. Drndic, V. Meunier, and M. S. Dresselhaus, “Anisotropic Electron-Photon and Electron-Phonon Interactions in Black Phosphorus (vol 16, pg 2260, 2016),” *Nano Letters*, vol. 16, no. 7, pp. 4731-4731, Jul, 2016.
- [85] J. X. Wu, N. N. Mao, L. M. Xie, H. Xu, and J. Zhang, “Identifying the Crystalline Orientation of Black Phosphorus Using Angle-Resolved Polarized Raman Spectroscopy,” *Angewandte Chemie-International Edition*, vol. 54, no. 8, pp. 2366-2369, Feb, 2015.
- [86] A. Ziletti, A. Carvalho, D. K. Campbell, D. F. Coker, and A. H. Castro Neto, “Oxygen defects in phosphorene,” *Phys Rev Lett*, vol. 114, no. 4, pp. 046801, Jan 30, 2015.
- [87] A. Ziletti, A. Carvalho, P. E. Trevisanutto, D. K. Campbell, D. F. Coker, and A. H. Castro Neto, “Phosphorene oxides: Bandgap engineering of phosphorene by oxidation,” *Physical Review B*, vol. 91, no. 8, 2015.

- 
- [88] M. Taniguchi, S. Suga, M. Seki, H. Sakamoto, H. Kanzaki, Y. Akahama, S. Terada, S. Endo, and S. Narita, “Valence band and core-level photoemission spectra of black phosphorus single crystals,” *Solid State Communications*, vol. 45, no. 2, pp. 59-61, 1983.
- [89] K. J. Gaskell, M. M. Smith, and P. M. A. Sherwood, “Valence band x-ray photoelectron spectroscopic studies of phosphorus oxides and phosphates,” *Journal of Vacuum Science & Technology A: Vacuum, Surfaces, and Films*, vol. 22, no. 4, pp. 1331-1336, 2004.
- [90] Y. Wang, and P. M. A. Sherwood, “Phosphorus Pentoxide (P₂O₅) by XPS,” *Surface Science Spectra*, vol. 9, no. 1, pp. 159-165, 2002.
- [91] P. Y. Shih, S. W. Yung, and T. S. Chin, “FTIR and XPS studies of P₂O₅–Na₂O–CuO glasses,” *Journal of Non-Crystalline Solids*, vol. 244, no. 2-3, pp. 211-222, 1999.
- [92] W. Luo, D. Y. Zemlyanov, C. A. Milligan, Y. Du, L. Yang, Y. Wu, and P. D. Ye, “Surface chemistry of black phosphorus under a controlled oxidative environment,” *Nanotechnology*, vol. 27, no. 43, pp. 434002, Sep 23, 2016.
- [93] H. M. Chang, A. Charnas, Y. M. Lin, P. D. Ye, C. I. Wu, and C. H. Wu, “Germanium-doped Metallic Ohmic Contacts in Black Phosphorus Field-Effect Transistors with Ultra-low Contact Resistance,” *Scientific Reports*,

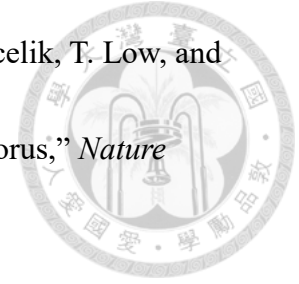


- vol. 7, pp. 9, Dec, 2017.
- [94] A. Castellanos-Gomez, "Black Phosphorus: Narrow Gap, Wide Applications," *J Phys Chem Lett*, vol. 6, no. 21, pp. 4280-91, Nov 05, 2015.
- [95] Y. Cai, G. Zhang, and Y. W. Zhang, "Layer-dependent band alignment and work function of few-layer phosphorene," *Sci Rep*, vol. 4, pp. 6677, Oct 20, 2014.
- [96] T. Hong, B. Chamlagain, W. Lin, H.-J. Chuang, M. Pan, Z. Zhou, and Y.-Q. J. N. Xu, "Polarized photocurrent response in black phosphorus field-effect transistors," vol. 6, no. 15, pp. 8978-8983, 2014.
- [97] K. Kaasbjerg, K. S. Thygesen, and K. W. Jacobsen, "Phonon-limited mobility in n-type single-layer MoS₂ from first principles," *Physical Review B*, vol. 85, no. 11, pp. 16, Mar, 2012.
- [98] Z. P. Ling, S. Sakar, S. Mathew, J. T. Zhu, K. Gopinadhan, T. Venkatesan, and K. W. Ang, "Black Phosphorus Transistors with Near Band Edge Contact Schottky Barrier," *Sci Rep*, vol. 5, pp. 18000, Dec 15, 2015.
- [99] A. V. Penumatcha, R. B. Salazar, and J. Appenzeller, "Analysing black phosphorus transistors using an analytic Schottky barrier MOSFET model (vol 6, 8948, 2015)," *Nature Communications*, vol. 7, pp. 1, Jun, 2016.
- [100] L. Li, M. Engel, D. B. Farmer, S. J. Han, and H. S. P. Wong,



- “High-Performance p-Type Black Phosphorus Transistor with Scandium Contact,” *Acs Nano*, vol. 10, no. 4, pp. 4672-4677, Apr, 2016.
- [101] Y. Liu, T. Low, and P. P. Ruden, “Mobility anisotropy in monolayer black phosphorus due to scattering by charged impurities,” *Physical Review B*, vol. 93, no. 16, pp. 5, Apr, 2016.
- [102] N. Haratipour, S. Namgung, R. Grassi, T. Low, S. H. Oh, and S. J. Koester, “High-Performance Black Phosphorus MOSFETs Using Crystal Orientation Control and Contact Engineering,” *Ieee Electron Device Letters*, vol. 38, no. 5, pp. 685-688, May, 2017.
- [103] N. Haratipour, M. C. Robbins, and S. J. Koester, “Black Phosphorus p-MOSFETs With 7-nm HfO₂ Gate Dielectric and Low Contact Resistance,” *Ieee Electron Device Letters*, vol. 36, no. 4, pp. 411-413, Apr, 2015.
- [104] A. Avsar, I. J. Vera-Marun, J. Y. Tan, K. Watanabe, T. Taniguchi, A. H. C. Neto, and B. Ozyilmaz, “Air-Stable Transport in Graphene-Contacted, Fully Encapsulated Ultrathin Black Phosphorus-Based Field-Effect Transistors,” *Acs Nano*, vol. 9, no. 4, pp. 4138-4145, Apr, 2015.
- [105] M. C. Robbins, and S. J. Koester, “Black Phosphorus p- and n-MOSFETs With Electrostatically Doped Contacts,” *Ieee Electron Device Letters*, vol. 38, no. 2, pp. 285-288, Feb, 2017.

[106] G. W. Zhang, S. Y. Huang, A. Chaves, C. Y. Song, V. O. Ozcelik, T. Low, and H. G. Yan, "Infrared fingerprints of few-layer black phosphorus," *Nature Communications*, vol. 8, pp. 9, Jan, 2017.



[107] L. Ye, H. Li, Z. F. Chen, and J. B. Xu, "Near-Infrared Photodetector Based on MoS₂/Black Phosphorus Heterojunction," *Acs Photonics*, vol. 3, no. 4, pp. 692-699, Apr, 2016.

[108] X. L. Chen, X. B. Lu, B. C. Deng, O. Sinai, Y. C. Shao, C. Li, S. F. Yuan, V. Tran, K. Watanabe, T. Taniguchi, D. Naveh, L. Yang, and F. N. Xia, "Widely tunable black phosphorus mid-infrared photodetector," *Nature Communications*, vol. 8, pp. 7, Nov, 2017.